RUTHENIUM OXIDE SOL-GELS AND CARBON-SUPPORTED RUTHENIUM OXIDE COMPOSITES FOR USE IN SUPERCAPACITORS

AARON ROWE

NOTE TO USERS

This reproduction is the best copy available.

Your file Votre référence
ISBN: 978-0-494-57486-7
Our file Notre référence
ISBN: 978-0-494-57486-7

Ruthenium Oxide Sol-Gels and Carbon-Supported Ruthenium Oxide Composites For Use in Supercapacitors

by

Aaron Rowe

A thesis submitted to the School of Graduate Studies in partial fulfillment of the requirements for the degree of Master of Science

Department of Chemistry
Memorial University of Newfoundland
St. John's, Newfoundland and Labrador, Canada
July 2007

Abstract

The major goal of this research was to prepare and characterize highly capacitive materials containing ruthenium oxide for use in supercapacitors. This was achieved by fabricating high surface area materials in efforts to produce minimized mass loadings of ruthenium oxide with maximized electrochemical contributions to capacitance.

Ruthenium oxide-titanium oxide hydrogels with a maximum specific capacitance of 10 F g^{-1} were prepared via a sol-gel method. During voltammetric cycling, these gels experienced leaching of ruthenium into the electrolyte which slowly diminished their capacitive capabilities. Subsequent annealing partially resolved the leaching issue, but the hydrogel stability remained questionable.

Carbon-supported ruthenium oxide composites were prepared using two types of high surface area carbon black as the supports onto which ruthenium nanoparticles were deposited via reduction of a ruthenium precursor. After deposition of the metal, ruthenium oxide was generated primarily by aging in air. Elemental analysis was used to elucidate the combined mass percent of ruthenium metal and/or oxide in the composites. X-ray photoelectron spectroscopy indicated that RuO_2 was the dominant oxide species and that unconverted ruthenium metal was present in the composites. X-ray diffraction confirmed this, with a mean ruthenium metal particle size of ca. 3.1 nm, while a mean ruthenium oxide particle size of 8.9 nm was found via transmission electron microscopy. The existence of ruthenium metal "cores" surrounded by ruthenium oxide "shells" was proposed to explain these results. Capacitance was measured via cyclic voltammetry. The

highest specific capacitance of all the composites was 574 F g^{-1}. A maximum specific capacitance of 758 F g^{-1} was found for ruthenium oxide itself amongst all composites.

Acknowledgements

I would like to express my deepest thanks to Dr. Peter Pickup for his supervision, guidance, encouragement and support throughout the duration of my program. I would also like to thank my supervisory committee, Dr. Raymond Poirier and Dr. David Thompson, for their helpful comments and advice.

I would also like to thank the members of the Pickup research group for their help and support during our time together. In particular, I want to thank Dr. Omar Yepez and Dr. Wanda Aylward for their helpful advice, cheerful dispositions and hilarious conversations during both good and difficult times.

I also want to thank Lisa Lee in the Biology Department at Memorial University for her assistance with sample imaging. Also, I wish to thank Dr. Zeynel Bayindir for his assistance and advice during my visit to the Institute for Research in Materials at Dalhousie University.

Financial support from the School of Graduate Studies, the Memorial University Chemistry Department, NSERC and Defence Research and Development Canada are gratefully acknowledged.

Finally, I wish to thank my family and friends, in particular my parents and my close friend Stacey Alexander, for their support, encouragement and understanding throughout my studies.

Table of Contents

List of Abbreviations

abs-EtOH – absolute ethanol

ACF – activated carbon fibre

CFP – carbon fibre paper

CNT – carbon nanotubes

CME – chemically modified electrode

CV – cyclic voltammetry or cyclic voltammogram

DDW – distilled deionized water

DMFC – direct methanol fuel cell

EDL – electrical double-layer

EDLC – electrochemical double-layer capacitor

ESR – equivalent series resistance

IHP – inner Helmholtz plane

MWNT – multi-walled nanotubes

OHP – outer Helmholtz plane

PEMFC – proton exchange membrane fuel cell

PVDC – polyvinylidene chloride

RuO_x – ruthenium oxide

SCE – saturated calomel electrode

SWNT – single-walled nanotube

$Ti(O^iPr)_4$ – titanium(IV) isopropoxide

TEM – transmission electron microscopy

XPS – X-ray photoelectron spectroscopy

XRD – X-ray diffraction

List of Tables

List of Figures

Chapter 1

Chapter 3

Chapter 4

Chapter 1

Introduction to Supercapacitors

1.1 Introduction to Electrical Energy Storage

Recently, there has been increasing research in electrochemical energy storage and conversion. As fossil fuel sources become increasingly scarce and global warming continues to be a distinct possibility, electrochemical energy has arisen as a sustainable and environmentally friendly alternative to traditional greenhouse gas emitting energy sources such as combustion engines, combustion-based steam-pistons and gas turbines. In addition, efficient new methods of storing vast amounts of energy are required by the demands of a growing technological society to power many modern day electronic devices such as portable electronics and electric / hybrid vehicles.

There are two fundamental ways in which electrical energy can be stored: as chemical energy and electrostatically.[1] When stored as chemical energy, the faradaic oxidation and reduction of electrochemically active masses in an electrolyte is required to release charge. The charge then flows between two electrodes with different potentials via an external load, during which time it can perform electrical work. Hence, chemical energy is converted directly into electrical energy. The extent of faradaic charge storage is referred to as capacity, measured in units of either coulombs (C) or watt hours (W h). A device which stores charge in this manner is called a battery.

When charge is stored electrostatically, an electric potential is applied to a pair of closely-spaced conductors, called plates, separated by an insulator material, called a dielectric.[1] Electric charges of equal magnitude and opposite polarity accumulate on the plates. This is also known as non-faradaic electrical energy storage, as no redox

chemistry is involved. A device which stores charge thusly is called a capacitor, or more specifically, an electrostatic capacitor.[1]

This gives rise to the term *capacitance*, which is the amount of electric charge stored for a given electrical potential. Capacitance is calculated as follows:

$$C = \frac{Q}{V} \qquad \text{(Equation 1.1)}$$

where C is capacitance in the SI unit farads (F), Q is the electric charge in coulombs (C), and V is the applied potential in volts (V). Thus, a capacitance of 1 farad is obtained when 1 coulomb of charge is stored due to the application of 1 volt of potential between the two plates.[1] Traditionally, capacitance has been expressed in terms of microfarads (μF), nanofarads (nF) and picofarads (pF), as units of farads are disproportionately large compared to the magnitude of capacitance values obtained for conventional capacitors. The charged stored, Q, is the product of the capacitance and voltage, CV. In so-called parallel-plate capacitors, the capacitance is directly proportional to the surface area of the plates and is inversely proportional to the distance between the plates as determined by the dielectric. The basic design of an electrostatic capacitor is illustrated in Figure 1.1.

As opposite charges develop on the plates of the capacitor, a potential difference arises between the two due to the electric field that is generated. The amount of energy stored in a capacitor between plates of charge $+q$ and $-q$ is given by:

$$G = \frac{1}{2}CV^2 \qquad \text{(Equation 1.2)}$$

where G is the Gibbs (free) energy in joules (J), C is the capacitance in farads, and V is the applied potential in volts. The maximum amount of energy that can be stored is

determined by the strength of the electric field which the dielectric can withstand without breaking down.[1]

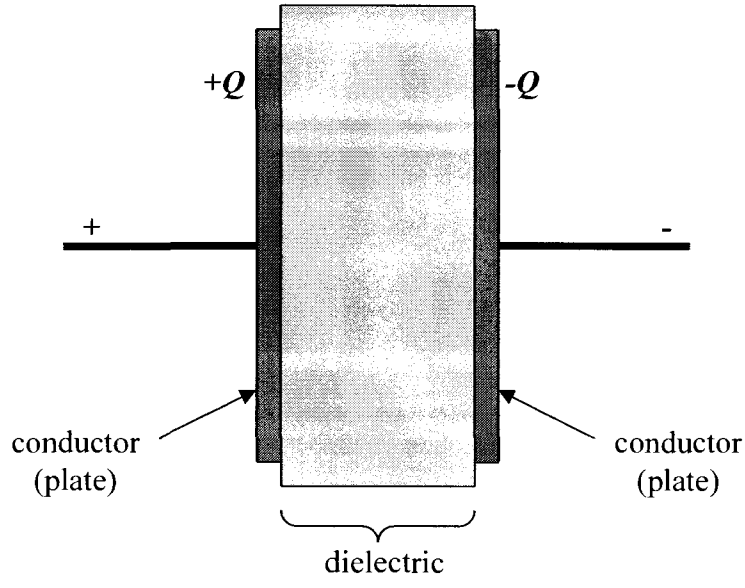

Figure 1.1. A conventional parallel-plate electrostatic capacitor.

There are three types of capacitors: conventional capacitors (also called traditional and/or common capacitors), electrolytic capacitors, and supercapacitors. Both conventional and electrolytic capacitors function as energy-storage devices in electric circuits, and are widely used in many applications. For example, they act as filters which divert electric signal spikes during power surges to prevent damage to sensitive circuitry.[1] They also absorb and conceal current fluctuations so as to provide "clean" power supplies

for signal or control circuits, such as those found in audio equipment. Radio receivers use capacitors as electronic filters which discern between signals of low and high frequency.[1] Their use in digital circuits prevents information loss in memory devices (such as computer hard drives) during electronic power failures. Supercapacitors, meanwhile, have emerged as a promising new electrochemical energy storage technology. The following section describes the characteristics of supercapacitors and how they are similar to and differ from conventional capacitors.

1.2 Supercapacitors

1.2.1 Introduction

A supercapacitor is a relatively new type of electrochemical energy storage device. Supercapacitors are characterized by their high power densities, relatively high energy densities and exceptionally large capacitances.[1,2] The name supercapacitor originates from the fact that these devices have capacitances and energy densities several orders of magnitude greater than conventional electrostatic capacitors.[2] Such characteristics have resulted in these devices also being referred to as "ultracapacitors" and "electrochemical capacitors"; while all three names are used interchangeably in the literature, the term supercapacitor will be used herein.

There are two types of supercapacitors, which are differentiated by their charge storage mechanisms: electrochemical double layer capacitors (EDLCs) and redox supercapacitors (also called faradaic pseudocapacitors). EDLCs store energy at the electrode-electrolyte interface via the separation of charge across the electrical double-

layer (EDL), i.e. the charge storage is electrostatic, not faradaic. The most common materials used in EDLCs are porous, high surface area carbons.[2] In contrast, the redox supercapacitor stores charge via the reversible faradaic reaction of an appropriate redox-active material. The most common materials used are conducting polymers and transition metal oxides.[1,2] Both EDLCs and pseudocapacitors will be explored in greater detail, including charge storage mechanisms and detailed characteristics of electrode materials, in Section 1.3 and 1.4, respectively.

As mentioned, supercapacitors have enhanced capacitances and energy densities compared to conventional capacitors. This is attributed to the differences between the way charge is stored in these devices. The first capacitor was discovered in 1745 by Ewald Georg von Kleist, and was known as the Leyden jar.[1] It formed the basis for the conventional electrostatic capacitor, which as mentioned earlier, stores charge on conductive plates that are separated by an insulating material. These capacitors have capacitances in the range of 10^{-12} to 10^{-6} F, and are typically reported in picofarads or nanofarads. In 1921, Julius Edgar Lillienfeld created the electrolytic capacitor, a term which sometimes causes confusion with the electrochemical capacitor. Electrolytic capacitors are composed of two conducting aluminum foil electrodes. One of the electrodes is coated in an insulating layer of Al_2O_3 which acts as the dielectric as well as a paper spacer soaked in a liquid electrolyte. The two Al foil electrodes are then rolled up in a cylindrical fashion, where the foil insulated by the oxide layer functions as the anode, while the liquid electrolyte and the other Al foil functions as the cathode.[1] These devices

typically exhibit capacitances in the range of 10^{-5} to 10^{-3} F, and are usually reported in microfarads.

In an EDLC, charge is stored across the EDL at the electrode-electrolyte interface; for example between a porous carbon electrode and an aqueous electrolyte. A simple model of a charged and discharged EDLC is shown in Figure 1.2. For these devices, the total cell capacitance, C_{Cell}, is calculated as follows:[1,2]

$$\frac{1}{C_{Cell}} = \frac{1}{C_1} + \frac{1}{C_2} \qquad \text{(Equation 1.3)}$$

where C_1 and C_2 are the capacitances of the first and second electrodes, respectively. These devices can achieve capacitances (C_{Cell}) up to 10 F using aqueous electrolytes, with values as high as 5000 F reported for carbon EDLCs using non-aqueous electrolytes.[2] Because of these relatively large values, capacitances for supercapacitors are most often reported as specific capacitances, in units of farads per gram of electroactive material (F g^{-1}). Both EDLCs and the electrical double-layer will be discussed in more detail in Section 1.3.1.

The increased charge storage and hence capacitance of supercapacitors is attributed to two factors. First, the separation of charge across the EDL takes place in a very small distance (0.3 to 0.5 nm in thickness) comprising the three-dimensional interphase between the electrode and electrolyte.[1] Second, EDLCs typically use electrode materials with very high surface areas, the significance of which is illustrated by the following equation:[2]

$$C_{dl} = \frac{\varepsilon A}{4\pi t} \qquad \text{(Equation 1.4)}$$

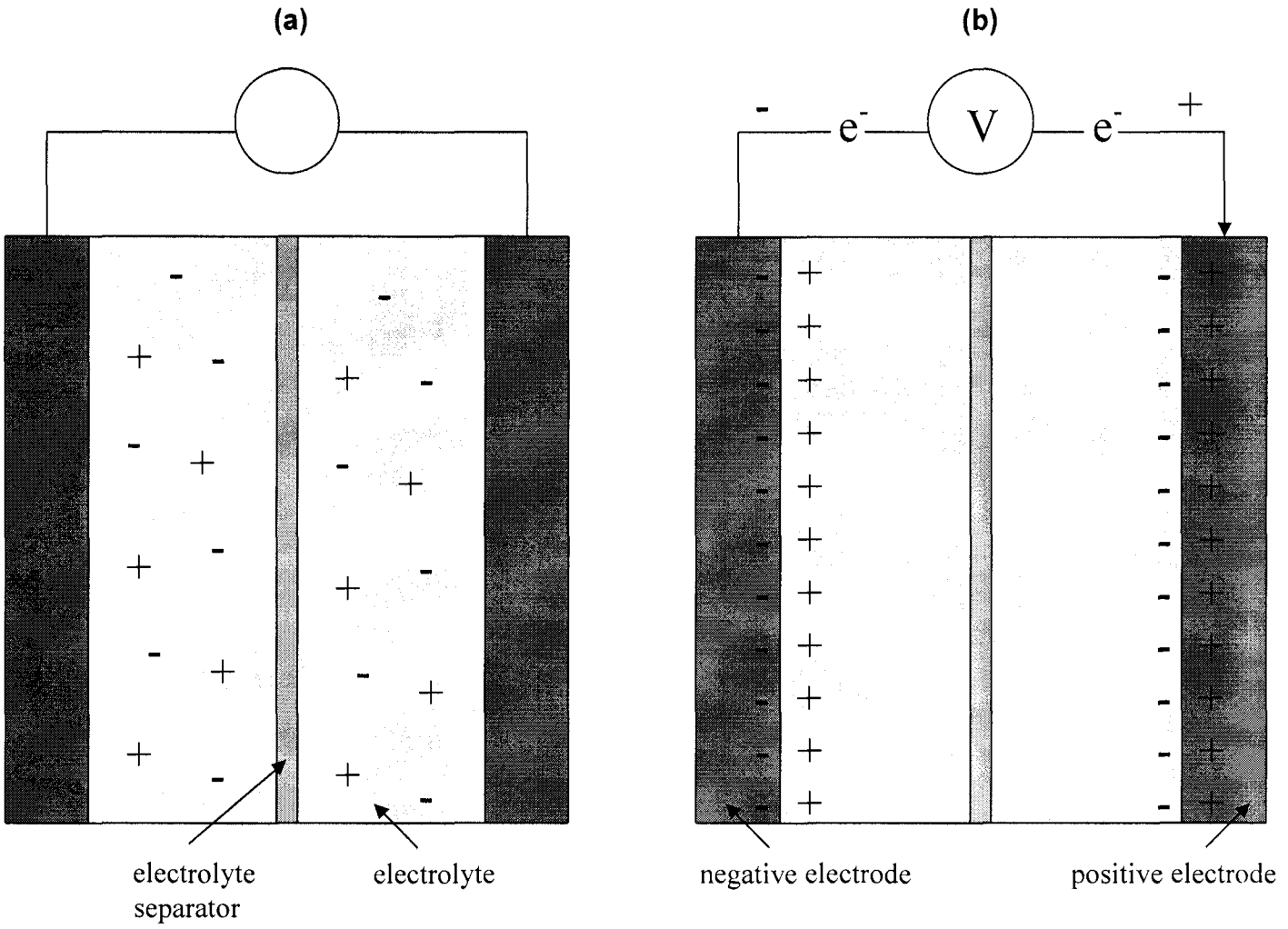

Figure 1.2. Simple model of a supercapacitor illustrating the (a) discharged and (b) charged states.

where C_{dl} is the double-layer capacitance, ε is the dielectric constant of the EDL interphase, A is the surface area of the electrode and *t* is the thickness of the EDL. Since the maximum attainable capacitance is directly proportional to the surface area of the electrode(s), this is an area where the supercapacitor excels. The incorporation of electrodes composed of porous, high surface area carbonaceous materials ranging from 100 m^2 g^{-1} to an impressive 2500 m^2 g^{-1} allows for significant gains in the amount of charge stored.[2] These two characteristics allows EDLCs to store charge (and hence energy) on a scale several orders of magnitude greater than either electrostatic or electrolytic capacitors. For example, the specific energy of an electrolytic capacitor is less than 0.1 W h kg^{-1}, while that of a supercapacitor ranges anywhere from 1 to 10 W h kg^{-1}.[2] In terms of power, supercapacitors are governed by the following equation:[2]

$$P_{max} = \frac{V^2}{4R} \qquad \text{(Equation 1.5)}$$

where P_{max} is the maximum power of the supercapacitor, V is the initial voltage across the device, and R is the equivalent series resistance (ESR) which is dominated by the electrolyte resistance. R is often low, resulting in very high power densities that approach 10^6 W kg^{-1}.[2] Electrolytic capacitors are capable of achieving somewhat lower specific power values in excess of 10^5 W kg^{-1}. Overall, comparison of the nanofarad capacitance range of electrostatic capacitors and the millifarad capacitance range of electrolytic capacitors to the farad capacitance range of supercapacitors highlights why these devices have emerged as the next evolution of the capacitor.

Supercapacitors offer numerous advantages as energy storage devices. First, they have long lifetimes, in excess of 500 000 cycles.[2] They require only seconds to minutes to become fully charged or discharged. They have high power densities, especially compared to electrostatic capacitors and batteries.[2] And as discussed above, they are extremely capacitive, with specific capacitance values in the range of 100 to 1000 F g^{-1}. Also, their materials are relatively non-toxic. In terms of their operation, they are based on relatively simple principles (e.g., compared to batteries) and are easily constructed using battery fabrication technology.[1,3] In addition, they can be combined with batteries to create hybrid power systems for use in a number of applications (discussed in Section 1.2.4).[1-3] And for the most part, the materials used to make them are inexpensive, especially when incorporating aqueous electrolytes.[1,4]

There are several drawbacks to supercapacitors, however, which limit their use given certain requirements. The biggest is their low energy density, especially compared to batteries,[1,4] which limits their use in several applications, a niche currently satisfied by batteries. This also translates to a poor volumetric energy density.[1] As well, supercapacitors have low operating voltages compared to electrolytic capacitors, with aqueous electrolyte voltages in the range of 0 to +1.4 V and non-aqueous electrolyte voltages at ca. +4.5 V (which translates to +3.5 V in practice).[1,2] When using said non-aqueous electrolytes, water-free materials must be used, increasing costs.[1] They are also prone to high self-discharge, especially compared to batteries.[5] Finally, given the lower operating potentials, the supercapacitors must be stacked to be used in high voltage applications.[1,4,5] These disadvantages have led current research to both find ways to

overcome the limitations of supercapacitors as well as develop systems containing supercapacitors which compliment, not replace, current electrochemical technology.

1.2.2 Historical Development

The supercapacitor is a relatively new device, having first been development by Becker and co-workers at General Electric in 1957.[6] Becker's patent involved using a high-area porous carbon material soaked with an aqueous electrolyte to store electrical energy via the charge held in the *interfacial* double-layer.[6] While the device exhibited high capacitance, its charge storage mechanism was unknown. In 1966, the SOHIO Corporation of Cleveland, Ohio patented a device similar to Becker's containing high surface area carbon materials which confirmed that the high capacitance was due to the storage of charge in the electrical double-layer.[7] Additionally, SOHIO used an electrolyte containing a tetraalkylammonium salt dissolved in a non-aqueous solvent.[7] This choice of electrolyte allowed operating voltages between 3.4 and 4.0 V to be achieved, as non-aqueous solvents are oxidized at higher potentials.[1] Since the amount of energy stored is proportional to the square of the potential achieved when fully charged, these systems also exhibited higher energy densities than those based on aqueous electrolytes.[1,7] This was followed by another patent for an "electrolytic capacitor" which consisted of a disc-like device containing an ion-permeable membrane which separated porous carbon paste electrodes soaked in a non-aqueous electrolyte.[1,8] This in fact was the first double-layer capacitor, and led to the use of the term "ultracapacitor" to describe such systems.[2] When

SOHIO was sold to NEC in 1971, double-layer capacitor development continued, successfully producing devices for memory backup.[2]

It was around this time that RuO_2 was first being examined as a potential electrode material by Galizzioli, Tandardini and Trasatti.[9-11] This idea was adopted by Conway *et al.* under contact with Continental Group in 1975. The group discovered that an energy-storage capacitor could be created based on the potential dependence of electrodeposited metal monolayers of Pb, Bi, and Cu, as well as electrochemically absorbed hydrogen, on Pt or Au electrodes.[12] This capability was labeled as "pseudocapacitance", as it did not rely on the traditional separation of charge for energy storage. The concept of pseudocapacitance was carried over to the study of solid metal oxide redox systems, namely RuO_2. It was discovered that RuO_2 films in aqueous H_2SO_4 yielded near ideal capacitive behaviour with relatively high values of capacitance. These pseudocapacitors had long life cycles greater than 10^5 cycles, and were highly reversible between charged and discharged states. The high capacitance values associated with these RuO_2 materials led to the term "supercapacitor".[1]

From here the development of these so-called double-layer capacitors and pseudocapacitors was largely in the commercial sector. Companies such as Matsushita Electric Industrial Company (the Gold Capacitor) and ELNA (Dynacap) developed double-layer capacitors for commercial use in the 1980s, while Pinnacle Research Corporation and PRI Ultracapacitor developed metal oxide redox systems primarily for military applications.[1] Significant academic interest began to grow in supercapacitors in the early 1990s, and has been building ever since. Promising new developments in both

EDLC and pseudocapacitor materials have been reported; these will be examined in detail in Sections 1.3 and 1.4, respectively. Concurrently, new commercial supercapacitors with increasing voltages and capacitances have entered the market to capitalize on the growing interest in supercapacitors as energy storage devices.[2]

1.2.3 Comparisons with Batteries and Fuel Cells

Supercapacitors are one of three types of electrochemical energy conversion and storage devices, the other two being batteries and fuel cells. These devices both convert chemical energy to electrical energy via redox reactions at the anode and cathode. However, the manner in which they store and convert energy is quite different. Batteries are considered closed systems in which the energy is both stored and converted in the same compartment. The anode and cathode are "active masses" which function as both redox-active materials and charge-transfer devices.[1,3] In contrast, fuel cells are considered open systems in which energy is stored and converted separately. The energy is stored externally as a fuel, i.e., hydrogen in a pressurized tank, alcohols in containers, and an oxidant, i.e., oxygen from the air or separate tank. The fuels are delivered to the fuel cell where they undergo redox reactions at the anode and cathode, which function as catalytic charge transfer media.[1,3] In both batteries and fuel cells, electrons complete the circuit by travelling through an external load thereby providing electricity for work. Illustrations of a basic battery (the Daniel cell) and a proton exchange membrane fuel cell (PEMFC) are shown in Figure 1.3.

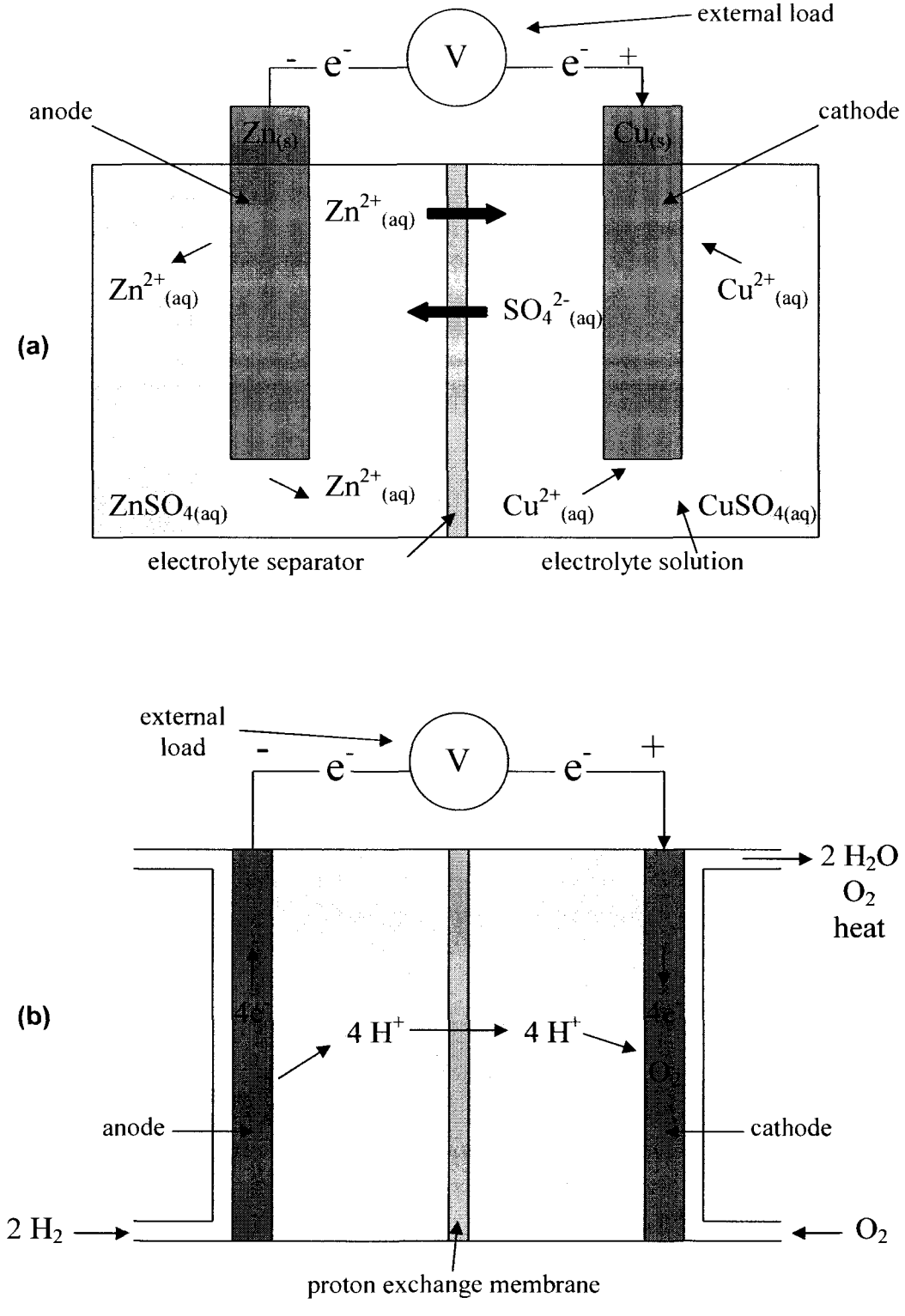

Figure 1.3. Diagrams of (a) a basic battery and (b) a PEMFC.

By contrast, supercapacitors are energy storage devices only; they do not convert chemical energy into electrical energy, but rather store energy via charge separation in the EDL in response to an applied potential. As such, they cannot be used as a source of electrical energy, but rather as a device for significant energy storage.[1,3] In terms of energy and power capabilities, supercapacitors differ significantly. Figure 1.4 shows a Ragone plot which compares the power and energy densities of different electrochemical devices. As seen, supercapacitors have specific power values greater than both batteries and fuel cells. However, they have significantly lower energy densities than batteries and especially fuel cells. For this reason, supercapacitors function as high-power devices, while fuel cells served as high energy devices.[3] As seen by the overlap in the Ragone plot with both aforementioned systems, batteries exhibit intermediate power yet high energy characteristics.[3] Accordingly, batteries have the greatest general application among the three, and are found in virtually all portable electronic devices.

In terms of electrochemical, power, and energy capabilities, supercapacitors are most similar to batteries. However, the two function on different electrochemical energy storage principles which produce individual strengths and weaknesses. For example, in EDLCs, no chemical or phase changes take place during the charge/discharge of the electric charge stored in the double-layer. This allows for an extended cycle life in excess of 500 000 cycles as mentioned previously.[2] In contrast, batteries undergo kinetically irreversible redox reactions which involve the irreversible phase change of the electroactive masses, i.e., electrodes. This significantly reduces cycle life, limiting the number of cycles to ca. 1000.[2] It also reduces the useful lifetime of the battery, as the

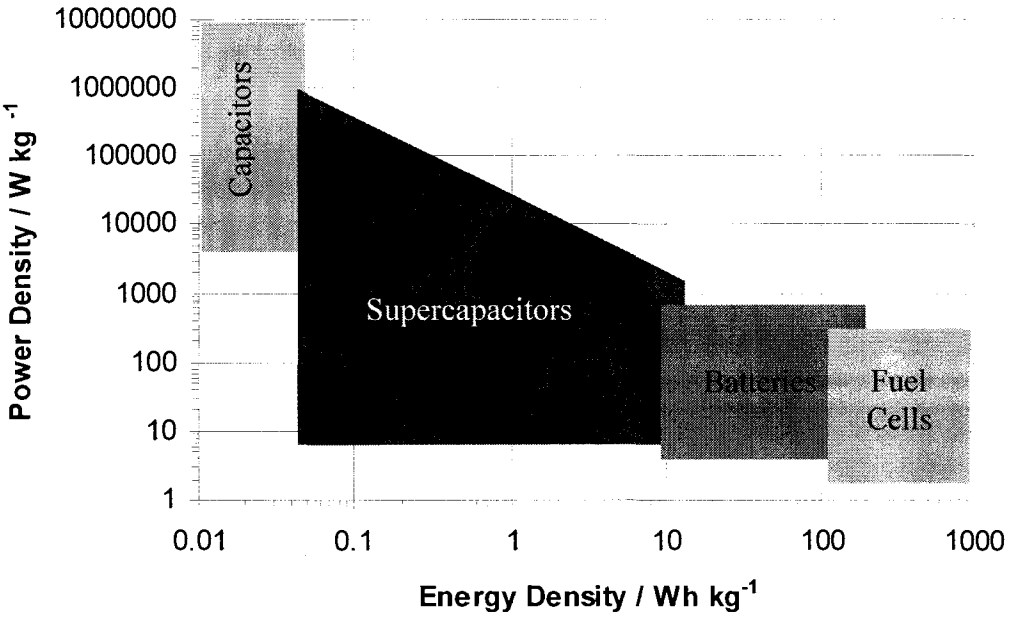

Figure 1.4. Ragone plot showing energy and power densities for different electrochemical energy conversion and storage devices. Adapted from Ref. 2.

electrodes become destabilized by repeated degradation and reformation during operation.[1] By comparison, supercapacitors have a superior lifetime, and are only impaired by minute problems such as current collector corrosion.[1] Supercapacitors also charge and discharge in as fast as a few minutes or seconds, while batteries typically require several hours to do so.[2] In addition, the potential of a supercapacitor both increases and decreases linearly when charged and discharged, respectively, making the amount of charge remaining easy to discern. By comparison, a battery maintains an almost constant potential when charged and discharged, making inherent charge

determination difficult.[1] As discussed earlier, the specific energy of supercapacitors (ca. 1 to 10 Wh kg^{-1}) is noticeably less than that of certain batteries (ca. 10 to 100 Wh kg^{-1}). However, the specific power of supercapacitors ranges from 500 to nearly 10^6 W kg^{-1}, easily besting the less than 1000 W kg^{-1} of batteries. In both cases however, the power is limited by the internal resistance of the device.[1,2]

1.2.4 Applications

The comparisons in the previous section illustrate that while supercapacitors are not a complete replacement for batteries, both devices are quite complimentary. While supercapacitors have higher power densities, longer cycle lives and rapid charge/discharge rates, batteries have higher energy densities, higher operating voltages and the means to produce electrical energy via conversion from chemical sources. It is for these reasons that supercapacitors are being touted for use with batteries in hybrid power systems.[4] In such a system, the supercapacitor and battery are placed in parallel. At low current loads the battery charges the supercapacitor; when high current loads are required, the supercapacitor rapidly discharges to provide high power.[5] In this way, battery life is extended and performance is enhanced. Such hybrid systems are being applied to electric vehicles, where the supercapacitor discharges during high power scenarios such as rapid acceleration and hill-climbing and recharges during deceleration, known as regenerative braking.[5,13] Additionally, this system may find use in environmentally friendly "idling stops" where an electric vehicle shuts down while stopped (e.g., at a red light or in heavy traffic) and uses the supercapacitor to rapidly

start-up again in order to accelerate.[14] Beyond electric vehicles, these hybrid systems also have applications in robotics.[1] Finally, hybrid systems using supercapacitors and portable fuel cells have been used to improve performance during high current loads.[5]

In addition to use in hybrid systems, supercapacitors are also employed as stand-alone pulse-power devices.[1,4] They have been used in heavy-load diesel vehicles to assist with starting, motor drives and actuators, military applications such as weapon systems and medical equipment, notably defibrillators.[1,3,4] They are also being developed as possible substitutes for batteries in future generations of portable consumer electronics including laptop computers, cellular phones, PDAs, portable media players, external hard disks and CD/DVD drives and GPS devices.[1-4] Finally, supercapacitors are also found in stationary electronic devices including uninterruptible power supplies, electric utility load leveling units and memory protection equipment.[1,13,14]

1.3 Electrochemical Double Layer Capacitors

1.3.1 Charge Storage Method

As defined earlier, EDLCs store energy at the electrode-electrolyte interphase via the separation of charge across the electrical double-layer (EDL), i.e. the charge storage is electrostatic, not faradaic. As the region is 3-dimensional, the term *interphase*[15] is used rather than *interface*, which implies a 2-dimensional boundary. The EDL itself has been the basis for extensive research in the past, and an understanding of its role in charge storage is important for EDLC development. The concept of the EDL was first observed by von Helmholtz who studied the quasi-2-dimensional interface and distribution of

oppositely charged colloidal particles.[16] His work led to the development of the first EDL model, known as the Helmholtz double-layer model.[16] In it, an array of oppositely charged surface ions and solution counterions form a so-called "double-layer" of negative and positive charges.[1,16] This model was later applied by Gouy to electrode interfaces in solution.[17] It was found that the double layer was not completely static, but rather was composed of a 3-dimensional diffuse region of electrolyte anions and cations adjacent to the electrode surface.[17,18] This model was refined by Chapman[18] to produce the Gouy-Chapman diffuse-layer model.[17,19] This was succeeded by the Stern model, which combined the Helmholtz and Gouy models.[20] In it, the EDL is composed of two layers: the Helmholtz layer (or compact layer), which accounts for finite ion sizes in the electrolyte, and the diffuse layer, which accounts for thermal fluctuations in solution.[20]

The most widely accepted model of the EDL was proposed by Grahame,[21] whose work was a further refinement of the Stern model. In this model, which is illustrated in Figure 1.5, the Helmholtz layer is treated as two separate planes.[3,21] The first, called the inner Helmholtz plane (IHP), refers to the distance of closest approach to the electrode surface that can be achieved for specifically absorbed anions and solvent molecules.[1,3] The second, called the outer Helmholtz plane (OHP), refers to the distance of closest approach for solvated, nonspecifically absorbed ions.[1,3] Limited by their solvation radii, these species cannot achieve the same distance of approach to the electrode as anions. As such, they form an outer layer over the inner layer of anions absorbed on the electrode where they are capable of long range coulombic interactions with the surface charge.[1,3]

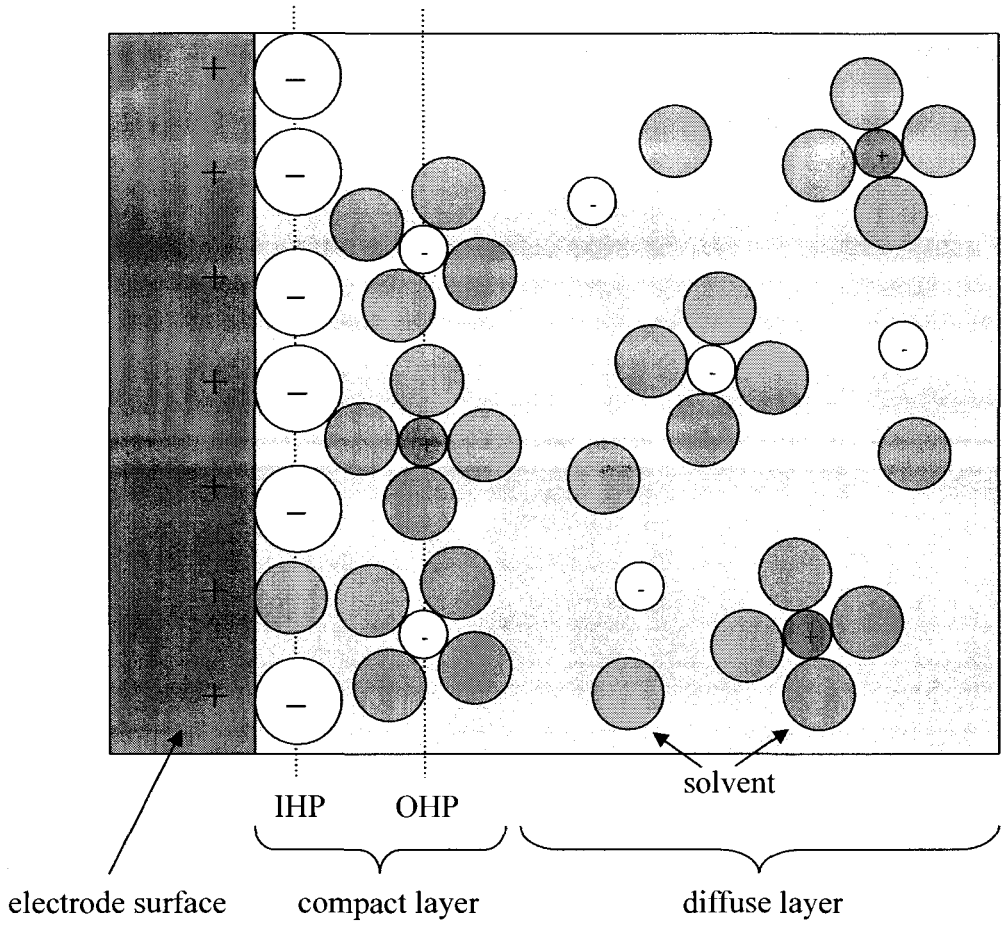

Figure 1.5. General representation of the Gouy-Chapman-Stern-Grahame model of the double layer.

Extending from the OHP into the bulk solution is a 3-dimensional region of scattered ions and solvent molecules called the diffuse layer.[22] As with the Stern and Gouy-Chapman models, it corresponds to the random ion dispersion caused by thermal fluctuation in opposition to the ordering caused by the electrical field.[3,22]

The Gouy-Chapman-Stern-Grahame model of the double layer leads to the concept of the "ideally polarizable electrode" which is essential to the phenomenon of double layer capacitance.[1] In an ideally polarizable electrode, the flow of charge to or from the electrode only changes the charge density on the electrode and ion density in the electrolyte at the interphase.[21] Thus, when the potential is changed, charge from the external load and ions from the electrolyte only move to and accumulate at the double layer itself, with no charge actually passing across the double-layer interphase.[21] In this way, the double-layer and interphase act as a capacitor, where the total charge of the compact and diffuse layers is equal in magnitude and opposite in sign to the net charge of the electrode surface.[22] This gives rise to the double-layer capacitance, C_{dl}, which is the combination of the capacitance of the compact layer in series with the diffuse layer. The capacitances are related by the following equation:

$$\frac{1}{C_{dl}} = \frac{1}{C_H} + \frac{1}{C_{diff}} \qquad \text{(Equation 1.6)}$$

where C_H is the capacitance of the compact layer and C_{diff} is the capacitance of the diffuse layer.[1] When sufficiently high electrolyte concentrations are used, the value of C_{diff} is small and C_{dl} is dominated by C_H.[22] It is in this manner that EDLCs store charge, with the value of C_{dl} for carbons and metals usually ranging from 10 to 40 $\mu F\ cm^{-2}$.[3,22]

1.3.2 Carbon Electrode Materials

Carbon materials are commonly used in energy-storage devices as electronically conductive additives and binders, supports for redox-active materials and intercalation

hosts.[23] These characteristics formed the initial basis for experimenting with carbon in EDLCs. Presently, EDLCs are fabricated almost entirely using carbon materials.[2] Carbon has numerous physical and chemical characteristics that make its different forms particularly attractive for use as supercapacitor electrode materials. These include high conductivity, high surface area values, controlled pore structures, stability at higher temperatures, resistance to corrosion, compatibility in composite materials and low material costs.[1,2]

Chief among these for use in supercapacitors are high surface areas and controlled pore structures. These properties are normally imparted during carbon material preparation via the processes of carbonization and activation. In carbonization, carbon-containing precursor materials such as hydrocarbons, coal, polymers and biomass undergo thermal decomposition in an inert atmosphere. This produces crystalline carbon fibers or amorphous carbons powders, depending on the precursor.[2] The carbons then undergo either thermal or chemical activation to increase their areas and pore sizes. In thermal activation, the carbon is heated in a controlled manner in the presence of an oxidizing gas such as steam or CO_2. This results in a controlled "burn-off" of carbon and residue pyrolysis products, resulting in greatly enhanced surface areas and pore volumes.[2] In chemical activation, the dehydration action of agents such as KOH at lower temperatures (ca. 400-700°C) is used to removed some carbon and pyrolysis products. The carbon is then washed to remove any residual material, resulting in substantial increases in surface area and porosity.[2] The surface areas range from 10 to over 2500 m^2 g^{-1}, while the pores are classified as either micropores (<2 nm), mesopores (between 2

and 50 nm) and macropores (>50 nm).[2,24,25] Generally, the carbon materials must be largely micro- and mesoporous[25] with surface areas[1] greater than 1000 m^2 g^{-1} to be effective as supercapacitor materials. Note that amorphous carbons often do not require activation, as they usually exhibit high surface areas and large pore sizes after carbonization.[2]

Overall, the high capacitance of these materials arises due to the combination of their characteristics. As an electrode, the carbon particles have good intra- and interparticle electronic conductivity.[1] The size of the pores as well as the extent of porosity of the carbon grants the electrolyte access to most of the carbon's expansive surface area.[1,2] With the carbon wetted by the chosen electrolyte, electrical double-layers as described above are established at the electrode-electrolyte interphases all along the surface area of the carbon.[2] Thus charge is stored in quantities far beyond that of conventional capacitors.

There are many different types of carbon used in EDLCs, namely glassy carbons, carbon aerogels, carbon fibers, carbon nanostructures and carbon blacks.[1,2,4,26-28] Glassy carbons (also called vitreous or polymeric carbons) are graphitizing carbons typically derived from the carbonization of polymer resins, such as phenolic resins.[2] Due to a largely inaccessible surface area and significant isolation of pores (which are 1-5 nm in size), they require either thermal or electrochemical oxidative activation to generate the high surface areas required by EDLCs.[29,30] Once activated, the volumetric surface area can reach as high as 1800 m^2 g^{-1} with a double layer capacitance of ca. 20 uF cm^{-2}.[30,31]

They are available in many forms including powders, individual films and thin sheets, making them highly versatile.[2,31,32]

Carbon aerogels are formed via the carbonization of organic aerogels.[33] These organic aerogels are prepared via a sol-gel method typically involving the poly-condensation of precursor materials, typically resorcinol and formaldehyde.[33,34] This technique results in highly porous carbon materials with uniform pores sizes in the range of 2 to 50 nm and high surface areas ranging from 400 to 1000 $m^2 g^{-1}$.[2] Further thermal activation of the aerogels increases the surface area to an even greater extent, with values as high as ca. 2500 $m^2 g^{-1}$ reported in the literature.[33] However, it was found that while surface area does increase with thermal activation, the capacitance of the carbon reaches a maximum at 1000 $m^2 g^{-1}$ of surface area.[33] In this case, the specific capacitance of the unactivated aerogel was 115 F g^{-1} while that of the activated carbon aerogel was ca. 180 F g^{-1}.[33] Carbon aerogels can be fabricated in many forms, namely monoliths, thin films, powders, composites and microbeads.[2] Binders are used to fashion the aerogel powders into electrodes, while the binder-less electrodes are prepared by mixing carbon fibers or fabrics with the sol-gel precursor solution.[35,36]

Carbon fibers are fabricated via the extrusion of an organic precursor through a die with subsequent stretching into a thin fiber.[2] The precursor fibres are commonly made of cellulose, phenolic resin, or pitch-based resin. The fibres are then carbonized and if desired, activated or graphitized at higher temperatures; at this point, they are called activated carbons fibres (ACFs). ACFs derived from pitch precursors have better electrical characteristics, while those obtained from phenolic resins have higher surface

areas.[37] ACFs are mostly microporous and come in several forms, including bundles, mats, threads and cloths. Of these, ACF cloths can achieve the highest surface areas,[2] up to 2500 $m^2 g^{-1}$.

Carbon nanotubes (CNTs) are prepared via the controlled catalytic decomposition of hydrocarbons. They have generated considerable interest for use in supercapacitors due to their accessible structures by way of high porosities. However, they are largely mesoporous and require activation to both increase surface areas and capacitances. Unactivated CNTs with surface areas between 120 and 400 $m^2 g^{-1}$ exhibit lower specific capacitances in the range of 10 to 15 F g^{-1}, while CNTs activated with KOH exhibit higher specific areas and capacitances of 1035 $m^2 g^{-1}$ and 90 F g^{-1}, respectively.[38] Oxidative treatment with HNO_3 has been shown to impart pseudocapacitive characteristics, further bolstering the specific capacitances to ca.130 F g^{-1} for multi-walled nanotubes (MWNTs).[39,40] Finally, carbonized single-walled nanotubes (SWNTs) mixed with polyvinylidene chloride (PVDC) binder to create composite electrodes have yielded maximum specific capacitances up to 180 F g^{-1} in KOH.[41]

Carbon blacks are derived from the carbonization of hydrocarbons in the gas phase. This is typically achieved via the thermal decomposition of gases, oils and distillates.[42] This process produces colloidal-sized particles which fuse into aggregates and agglomerates containing nearly spherical carbon particles.[42] These materials are characterized by their small particle size, high porosity and highly branched, open structure.[2] These characteristics make them ideal conductive fillers in electrodes for certain batteries and supercapacitor (when not used as the primary material)

electrodes.[43,44] Their porosity arises from surface pitting, hollowed out particle interiors, and voids between and within the aggregates of fused carbon particles.[2] Compared to other carbonaceous materials, the highly porous nature of carbon blacks allows the surface area to be more readily accessed by electrolytes.[43] This has resulted in carbon blacks with surface areas greater than 1500 $m^2 g^{-1}$ yielding specific capacitance values as high as 250 F g^{-1} when mixed with binders.[45,46] Overall, there are many types of carbon blacks, encompassing a wide range of surface areas and degrees of porosity, which are classified individually according to their preparation methods.

1.4 Redox Supercapacitors

1.4.1 Charge Storage Method

In contrast to EDLCs, redox supercapacitors (or pseudocapacitors) store charge via reversible redox reactions of appropriate electroactive materials. The method of charge storage involves faradaic reactions between the electrode material and the electrolyte resulting in charge transfer across the double-layer.[1] This charge transfer is linearly dependent on voltage due to thermodynamics, such that the extent of charge transfer, q, is a continuous function of electrode potential, V. The derivative of this relationship, dq/dV, has properties which are equivalent to a capacitance.[1] This differs from the faradaic behaviour of devices such as batteries, in which the potential changes only slightly based on the state of charge. Such a capacitance is observed when the extent to which the charge-transfer process occurs is limited by a finite quantity of electrode surface area or material.[1,2] As this method of *faradaic* charge storage is fundamentally

different from the classical *electrostatic* double-layer capacitance discussed in Section 1.3.1, it is referred to as pseudocapacitance (sometimes denoted C_Φ).[1,2] At a given weight and/or volume, supercapacitors using pseudocapacitive materials are capable of producing capacitances that are 10 to 100 times greater than those of EDLCs.[1]

Thermodynamically, pseudocapacitance is observed in an electrochemical system when a property proportional to charge transferred is related to potential according to the following equation:[1]

$$\frac{y}{(1-y)} = K \cdot \exp\left(\frac{VF}{RT}\right) \qquad \text{(Equation 1.7)}$$

where y is the proportional charge transfer property, K is the equilibrium constant, V is the potential, F is Faraday's constant, R is the gas constant and T is temperature. The derivative of this equation yields d*y*/dV, which is analogous to d*q*/dV and hence, pseudocapacitance. Charge transfer properties according to this equation are found in 3 different systems used in supercapacitors.[47] In underpotential deposition, *y* is related to charge via the fractional coverage of deposited adatoms on the electrode surface. In intercalation systems, y represents the extent of fractional absorption of a species, such as Li^+, into an intercalation host.[47] Most importantly, in redox systems, *y* represents the extent of conversion between the oxidized (Ox) and reduced (Red) forms of species in solution or hydrous oxide materials according to the simple redox equation:[22, 47]

$$Ox + ne^- \rightleftharpoons Red \qquad \text{(Equation 1.8)}$$

The potential of this reaction is a logarithmic function of the ratio of concentrations (or activities) of the oxidized and reduced forms as governed by the Nernst equation:[22]

$$E = E^{o} + \frac{RT}{nF} \ln \frac{[Ox]}{[\mathrm{Re}\, d]} \qquad \text{(Equation 1.9)}$$

where E is the potential, E^{o} is the standard potential, and [Ox] and [Red] are the concentrations of the oxidized and reduced species. When [Ox] and [Red] are expressed as the relative fractions [Ox]/([Ox]+[Red]) and (1-[Ox])/([Ox]+[Red]), the general term X = [Ox]/([Ox]+[Red]) can be used to express ln [Ox]/[Red] as ln (X/(1-X)).[47] In this form, X/(1-X) is analogous to the term y/(1-y) from Equation 1.4, and is logarithmically related to potential.[1,47] Hence, such redox systems exhibit a pseudocapacitance during charge/discharge. It is redox reactions exhibiting pseudocapacitance which comprise the majority of research on faradaic pseudocapacitors.

1.4.2 Electrode Materials

There are presently two major types of materials used as redox supercapacitors: conducting polymers and transition metal oxides. Electronically conducting polymers are conjugated polymer chains capable of being chemically and/or electrochemically oxidized and reduced in a reversible fashion.[1] This involves "doping" the polymer via the insertion or withdrawal of electrons at the electrode interface to generate radical anion and cation charge centres.[1] Electronic conductivity is achieved through electron hopping via the delocalized π system of the conjugated polymer backbone.[22] The extents of the redox reactions are potential dependent, and so pseudocapacitance arises. Some of the most studied types of conducting polymers for use in supercapacitors are polyaniline,[48-50] polypyrrole[50,52] and derivatives of polythiophene.[53,54] The polymers are typically

produced *in situ* on substrates such as metal gauzes and foils or electronically conductive carbon fibre substrates.[1] Supercapacitors employing conducting polymers benefit from their high conductivity, relatively good reversibility with cycling, relatively high specific capacitances (ca. 450 F g^{-1}), cheap raw materials and easy fabrication.[1]

Transition metal oxides have received great attention in recent years as potential materials for use in supercapacitors.[1,2,4] These oxides, namely Co_3O_4,[47] MoO_3,[47] WO_3,[47] MnO_2,[55-58] NiO_x,[59-61] IrO_2,[47] and most importantly, RuO_2.[1,9-11,47,27,62-65] have been shown to exhibit variable, yet substantial capacitive capabilities. For a transition metal oxide to be considered sufficiently pseudocapacitance, it must meet three criteria.[1] First, it must be electronically conductive. Second, it must have two or more oxidation states which facilitate electron hopping during oxidation and reduction without associated irreversible phase changes in the oxide. Finally, the oxide must have ionic conductivity to allow proton insertion and withdrawal (in aqueous systems) throughout the material so that O^{2-} sites can be converted to OH^- and vice versa. This is ideally achieved via hydrous oxide lattices, as is the case with $RuO_2 \cdot xH_2O$.[1]

1.4.3 Ruthenium Oxide

Ruthenium oxide (RuO_2) is used in a number of fields due to its excellent electronic conductivity, electrocatalytic properties and mechanical stability.[1,66] Electrodes composed of RuO_2 on different substrates as well as RuO_2-TiO_2 binaries are used as dimensionally stable anodes for the production of sodium hydroxide and chlorine gas from brine in the chloro-alkali industry.[67,68] Such materials have also been used as

cathodes for oxygen reduction[69] and electrodes for studying the electrocatalytic behaviour of alkenes.[66] In recent years, hydrous RuO_2 in Pt-Ru anodes of direct methanol fuel cells (DMFCs) has been shown to play an important role in electrocatalysis.[70] In energy storage, RuO_2 has been vital to the development of redox supercapacitors based on transition metal oxides, and indeed, supercapacitors in general. Its application to electrochemical energy storage was first recognized by Trasatti and Buzzanca,[9] who grew oxide films on solid Ru electrodes using cyclic voltammetry. They observed that as the RuO_2 film grew with repeated cycling, the electrode exhibited nearly featureless, rectangular voltammagrams resembling the constant current vs. potential response of a capacitance.[9]

Crystalline RuO_2 is a d-band metallic conductor, exhibiting a specific capacitance of ca. 350 F g^{-1} at 100 mV s^{-1}.[71] In contrast, it as been shown that hydrous ruthenium oxide ($RuO_2 \cdot xH_2O$) in an amorphous form has by far the greatest specific capacitance amongst the transition metal oxides, and is in fact the most capacitive material yet discovered.[27] An impressive 720 F g^{-1} at 2 mV s^{-1} for amorphous $RuO_2 \cdot xH_2O$ prepared by the sol-gel method and annealed at 150°C has been reported.[27] The high specific (pseudo) capacitance of $RuO_2 \cdot xH_2O$ (also expressed as RuO_xH_y) is attributed to its mixed electronic-protonic conductivity.[72] In aqueous electrolyte, the pseudocapacitive charge storage mechanism involves the "double insertion" of electrons and protons into sites at the surface of the hydrous oxide according to the following equation:[26,67,72]

$$RuO_x(OH)_y + \delta H^+ + \delta e^- \rightleftharpoons RuO_{x-\delta}(OH)_{y+\delta} \qquad \text{(Equation 1.10)}$$

In this redox reaction, the Ru^{n+} species are reduced while the oxygen is protonated to achieve charge balance. This is shown for the Ru^{4+}/Ru^{3+} couple below:[72-74]

$$Ru^{4+}-O^{2-}+H^{+}+e^{-} \rightleftharpoons Ru^{3+}-OH^{-} \qquad \text{(Equation 1.11)}$$

This yields a changing Ru oxidation state between Ru^{4+}, Ru^{3+}, and Ru^{2+} overall.[75] In the $RuO_2 \cdot xH_2O$, proton transfer occurs through the hydrous oxide matrix, while electron transfer occurs through the conduction band of RuO_2.[72] When redox occurs as above, interactions between sites with different oxidation states results in energy sharing for ruthenium oxidation.[1] This results in the overlap of successive redox couples (predominately Ru^{4+}/Ru^{3+} and Ru^{3+}/Ru^{2+}) over a broad range of redox potentials which effectively extends the potential window for oxidation to over 1 V.[75,76] The resultant current is continuous and largely dependent on potential, classifying the process as pseudocapacitive.[1,75] The magnitude of the capacitance is determined by the number of reaction sites within the oxide's surface, bulk, or both.[76]

The pseudocapacitance of $RuO_2 \cdot xH_2O$ is influenced most by its crystallinity and hydration. Although crystalline RuO_2 is a metallic conductor, the degree of crystallinity influences the proton conductivity of $RuO_2 \cdot xH_2O$. With increasing crystallinity, the water content of the oxide decreases, resulting in the loss of protonated oxygen sites.[76,77] This results in decreasing porosity in which protons are unable to penetrate the increasingly ordered crystalline lattices to reach protonated RuO_2 within the bulk.[77,78] The charge/discharge process according to Equations 1.10 and 1.11 then becomes limited by the mass transport of protons into the bulk oxide, with the only contribution to capacitance arising from redox of accessible surface Ru sites.[27,47,76] Crystalline

$RuO_2 \cdot 0.03H_2O$ reported by Jow *et al.* has a very low specific capacitance value of 19 F g^{-1}.[27] In the extreme case, Rolison et al. reported a specific capacitance of only 0.75 F g^{-1} for crystalline, anhydrous RuO_2.[74] Both confirmed that capacitance is maximized when a hydration state of $x = 0.5$ mol % H_2O is achieved with little crystallization of the oxide at low annealing temperatures.[27,74] Amorphous $RuO_2 \cdot 0.5H_2O$ prepared by a sol-gel method and annealed at 150°C yielded a specific capacitance of 720 F g^{-1}, emphasizing the need for sufficient hydration and non-crystallinity. Recent studies of $RuO_2 \cdot xH_2O$ have suggested that it is not truly amorphous, but rather exists as a network of rutile-like nanocrystalline RuO_2 with water dispersed between the boundaries of the nanocrystals.[72] Electrons are conducted by the rutile RuO_2 while structural water associated with Ru–O provides proton conductivity.[72]

The pseudocapacitance of $RuO_2 \cdot xH_2O$ is also influenced to a lesser extent by its surface area. Even when hydration is substantial, a large surface area is desired so as to maximize the number of readily accessible protonated oxygen sites for participation in the charge/discharge mechanism.[1] The surface area of $RuO_2 \cdot xH_2O$ also gives rise to a small double-layer capacitance which is only a fraction of the total specific capacitance of the material.[1]

To date, no one explanation of the structure or charge storage capability of $RuO_2 \cdot xH_2O$ has proven to be definitive. Regardless, RuO_2 must be prepared as a hydrous oxide, amorphous in character, with a high porosity leading to a high surface area. All of these requirements are met in the ideal material, amorphous $RuO_2 \cdot 0.5H_2O$.

1.5 Introduction to Sol-Gels

Sol-gels are 3-dimensional networks of nanoscale inorganic particles surrounded by a continuous, highly mesoporous volume of free space.[74,79] They are formed from the gelation of a colloidal suspension in a series of hydrolysis and polycondensation reactions. Sol-gels are characterized by their high surface areas, low densities, and large mesoporosities which facilitate rapid mass transport of molecules throughout the gel structure.[79] These properties give rise to a number of applications for sol-gels in fields such as catalysis, electrocatalysis, sensors, nonlinear optics and charge storage.[79,80-83]

Sol-gel synthesis can be broken down into two types: aqueous-based, which uses a solution of a metal salt, and alcohol-based, which uses an organometallic precursor dissolved in an suitable alcohol.[84] Alcohol-based methods are more commonly used as organometallic precursors can be chosen to control the chemistry, processing and thus morphology of the final gel. [79] The most popular precursors are metal alkoxides of the general form $M(OR)_n$, where M is Al, Cr, Si, V, Ti, V, Mo, Ru, etc. and OR is an alkoxy ligand.[79, 84]

The sol-gel process involves four distinct steps: hydrolysis and condensation, gelation, aging and drying.[84] The starting materials usually consist of a metal alkoxide such at titanium(IV) isopropoxide, water, solvent such as methanol or ethanol, and an acid or base catalyst.[85] In the first step, the catalyst initiates the hydrolysis of a metal alkoxide precursor, producing alcohol groups (ROH) and hydroxylated metal centres (M–OH), as shown below:[79,84]

$$M(OR)_n + H_2O \rightarrow [M(OR)_{n-1}(OH)] + ROH \qquad \text{(Equation 1.12)}$$

This is followed by condensation reactions involving the formation of oxygen bridges and expulsion of XOH species, as follows:[79]

$$M\text{–}OH + M\text{–}OX \rightarrow M\text{–}O\text{–}M + XOH \qquad \text{(Equation 1.13)}$$

where X = H or R. At this point, the mixture is called a sol, a colloidal suspension that is liquid in character containing colloidal sized oxide particles in the range of <1 to 100 nm.[85]

As the above hydrolysis and polycondensation reactions continue, cross-linking and cluster growth of the colloidal particles propagates in 3-dimensions, creating the M–O–M gel network.[85] This is known as gelation, in which the gel incorporates the dispersed sol into a coherent solid framework which is interpenetrated by a liquid phase (usually the solvent).[84] Gelation is accompanied by a sharp increase in viscosity, with the "gel point" occurring once the a particular polymer structure is "frozen in".[86]

The gel then sets while still immersed in its mother liquor in a process called aging. Polymerization continues as further polycondensation reactions occur, increasing the number of linkages.[84] The gel also begins to shrink, expelling liquid from its pores. Smaller particles in the gel dissolve and re-precipitate onto larger ones in a process known as coarsening.[84] This process increases pore sizes while decreasing specific surface area.[86] Finally, phase transformations occur in which the solid phase separates from the liquid phase on a local scale.[84] Overall, aging results in a strengthening of the gel network, with longer aging times producing stronger gels.[84]

After aging, the liquid phase is removed from the porous solid network in the drying step. As the solvent evaporates, the solid shrinks in volume equal to that of the

liquid, such that the liquid-vapour phase only exists at the exterior surface of the solid.[84] The internal shrinking stops once the solid becomes too rigid, allowing the liquid to migrate from the exterior to the interior of the network where it becomes isolated in pockets.[84] The liquid-vapour interface within the interior contributes to capillary pressure which stresses the "walls" of the network, resulting in a collapse of the gel.[79] Thus, the method with which this internal liquid is removed from the pores determines the final structure, porosity and density of the gel. Supercritically drying the gel to remove the internal liquid results in no capillary pressure, producing high surface area (>1000 m^2 g^{-1}),[84] highly porous (up to 99%)[87] and low density solids called aerogels. In many cases, aerogels are desirable as they retain the surface area and porosity of the original sol-gel.[79] Drying by simple evaporation in ambient conditions results in strong capillary pressure which collapses the gel to produce a condensed solid called a xerogel.[79,84] In comparison to aerogels, xerogels have lower surface areas (150-900 m^2 g^{-1}) and porosities (ca. 25%), and are more dense.[84,85] The xerogel continues to shrink until the structure is able to withstand the tensile strength of the liquid.[84] If the gel is not dried prior to use but rather is aged in the mother liquor to increase the solvent content it is called a hydrogel.[79]

The final structure and size of a sol-gel is determined by the rates of hydrolysis and condensation, which are largely pH dependent.[84] When an acid catalyst is used, hydrolysis is rapid and condensation becomes rate-determining, producing small hydroxylated oligomers which form a linear polymeric gel network with small pores.[79,85] Conversely, when a base catalyst is used, condensation is rapid and hydrolysis is rate

determining, producing a gel network of cross-linked colloidal particles with large pores.[79,85]

Sol-gels have applications in electrochemical energy storage and conversion. MnO_2, MoO_3 and especially V_2O_5 sol-gels have been studied as intercalation materials for lithium-ion batteries.[79] V_2O_5 aerogels are the most prominent, as they reversibly intercalate with greater capacities than other metal oxide aerogels.[79] Lithiated V_2O_5 aerogels also have much higher specific energies than crystalline intercalation electrode materials such as $LiCoO_2$ or $LiMn_2O_4$.[79] MnO_2 aerogels are lithium-ion intercalation materials being studied as lower cost and lower toxicity replacements for $LiCoO_2$.[79] However, they are limited by high discharge rates resulting in diminished lithium capacity.[79] MoO_3 aerogels are also capable of reversibly intercalating Li^+ with good capacities and discharge properties.[79,88] In addition, MoO_3 in fuel cells anodes containing Pt-Mo electrocatalysts helps improve CO tolerance.[79]

Several sol-gel materials have been explored for use in supercapacitors. Several of these will be discussed in Section 3.1.

1.6 Thesis Objectives

The main objective of the work contained herein is to prepare and characterize new, high capacitance materials containing ruthenium oxide for use in supercapacitors. To achieve high capacitances, it is necessary to fabricate materials with high surface areas which allow a maximum effective loading of ruthenium oxide to be achieved while minimizing the total mass of the electroactive material.

Chapter 3 describes the preparation of RuO_2-TiO_2 hydrogels, the capacitive capability of which is measured by cyclic voltammetry. Electrochemical setup, corrosion and hydrogel stability issues are identified and addressed accordingly.

Chapter 4 describes the preparation and characterization of carbon-supported ruthenium oxide composites using two types of carbon black supports. Cyclic voltammetry is used to measure capacitances, while transmission electron microscopy, X-ray photoelectron and X-ray diffraction are used to characterize the composites.

1.7 References

1. Conway, B. E. *Electrochemical Capacitors: Scientific Fundamentals and Technological Applications*, New York: Kluwer Academic / Plenum Publishers, 1999.

2. Hollenkamp, A. F.; Pandolfo, A. G. *J. Power Sources*. **2006**, *157*, 11.

3. Brodd, R.; Winter, M. *Chem. Rev.* **2004**, *104*, 4245.

4. Burke, A. *J. Power Sources* **2000**, *91*, 37.

5. Buchmann, Isidor. "The Supercapacitor." Batteries in a Portable World. 2001. Cadex Electronics, Inc. <http://www.buchmann.ca/chap2-page10.asp>

6. Becker, H. E., "Low voltage electrolyte capacitor", U.S. patent 2800616 (to General Electric Co.) (1957).

7. Rightmire, R.A., "Electrical energy storage apparatus", U.S. patent 3288641 (to Standard Oil of Ohio Co.) (1966).

8. Boos, D. L. "Electrolytic capacitor having carbon paste electrodes", U.S. patent 3536963 (to Standard Oil of Ohio Co.) (1970).

9. Buzzanca, G.; Trasatti, S. *J. Electroanal. Chem.* **1971**, *29*, A1.

10. Galizzioli, G.; Tandardini, G.; Trasatti, S. *J. Appl. Electrochem.* **1974**, *4*, 57.

11. Galizzioli, G.; Tandardini, G.; Trasatti, S. *J. Appl. Electrochem.* **1975**, *5*, 203.

12. Conway, B. E.; Kozlowska, H. A. *Acct. Chem. Res.* **1981**, *14*, 49.

13. "Capacitors and Supercapacitors." 2005. MPower Solutions, Ltd. <http://www.mpoweruk.com/supercaps.htm>

14. "Supercapacitor Applications." 2004. NEC TOKIN Corporation. <http://www.nec-tokin.com/english/product/supercapacitor/application02.html>

15. Guggenheim, E. A. *J. Chem. Phys*, **1936**, *4*, 689.

16. von Helmholtz, H. *Ann. Phys. (Leipzig)*, **1853**, *89*, 211.

17. Gouy, G. *J. de Phys.*, **1910**, *9*, 457.

18. Chapman, D. L. *Phil. Mag.*, **1913**, *25*, 185.

19. Gouy, G. *Ann. Phys., Paris*, **1917**, *7*, 129.

20. Stern, O. *Zeit. Elektrochem.*, **1924**, *24*, 508.

21. Grahame, D. C. *Chem. Rev.*, **1947**, *41*, 441.

22. Wang, J. *Analytical Electrochemistry*, New York: Wiley-VCH, 2000.

23. Fialkov, A. S. *J. Electrochem.* **2000**, *36*, 389.

24. Chesneau, M.; Fauvarque, J. F.; Gamby, J.; Simon, P.; Taberna, P. L. *J. Power Sources* **2001**, 101, 109.

25. Lin, C.; Ploehn, H. J.; Popov, B. N. *J. Electrochem. Soc.* **2002**, 149, A167.

26. Chen, C.P.; Tilak, B.V.; Sarangapani, S. *J. Electrochem. Soc.* **1996**, 143, 3791.

27. Cygan, P.J.; Jow, T.R.; Zheng, J.P. *J. Electrochem. Soc.* **1995**, 142, 2699.

28. Belanger, D.; Hill, I. R.; Quinn, D.; Toupin, M. *J. Power Sources.* **2005**, 140, 203.

29. Alliata, D.; Haas, O.; Haring, P.; Kotz, R.; Siegenthaler, H. *Electrochem. Solid-State Lett.* **1999**, *2*, 33.

30. Bartsch, M.; Braun, A.; Hass, O.; Kotz, R.; Merlo, O.; Schnaffner, B.; Schnyder, B.; Wokaun, A. *Carbon*, **2003**, *41*, 759.

31. Bartsch, M.; Braun, A.; Goerigk, J.; Hass, O.; Haubold, H.-G.; Kotz, R.; Schnyder, B. *J. Non-Cryst. Solids*, **1999**, *260*, 1.

32. Bartsch, M.; Braun, A.; Hass, O.; Kotz, R.; Schnyder, B.; Wokaun, A. *Carbon*, **2002**, *40*, 375.

33. Fricke, J.; Probstle, H.; Wiener, M. *J. Porous Mater.*, **2003**, *10*, 213.

34. Pekala, P. W. *J. Mater. Sci.* **1989**, *24*, 3221.

35. Fricke, J.; Probstle, H.; Schmitt, C. *J. Non-Cryst. Solids*, **2001**, *285*, 277.

36. Fricke, J.; Probstle, H.; Schmitt, C. *J. Power Sources*, **2002**, *105*, 189.

37. Nishino, A.; Tanahashi, I.; Yoshida, A. *Carbon*, **1990**, *28*, 611.

38. Beguin, F.; Cazorla-Amoros, D.; Delpeux, S.; Frackowiak, E.; Jurewicz, K.; Szostak, K. *Chem. Phys. Lett.* **2002**, *361*, 35.

39. Beguin, F.; Bertagna, V.; Frackowiak, E.; Metenier, K. *Appl. Phys. Lett.* **2000**, *77*, 2421.

40. Beguin, F.; Frackowiak, E. *Carbon*, **2001**, *39*, 937.

41. An, K. H.; Bae, S. C.; Choi, Y. C.; Chung, D. J.; Kim, W.S.; Lee, D. C.; Lim, S. C.; Park, Y. C. *Adv. Mater.* **2001**, *13*, 497.

42. Bansal, R.C., Donnet, J.B. and Wang, M. J. *Carbon Black Science and Technology*, 2nd ed., Marcel Dekker, New York, 1993.

43. Jow, T. R.; Zheng, J. P. *J. Power Sources*, **1996**, *62*, 155.

44. Liu, X.; Nojima, M.; Osaka, T. *J. Power Sources*, **1998**, *74*, 122.

45. Beck, F.; Dolata, E.; Grivei, E.; Probst, N. *J. Appl. Electrochem.* **2001**, 31, 845.

46. Muller, S.; Richner, R.; Wokaum, A. *Carbon*, **2002**, *40*, 307.

47. Birss, V.; Conway, B. E.; Wojtowicz, J. *J. Power Sources*, **1997**, *66*, 1.

48. Genies, E. M.; Tsintavis, C. *J. Electroanal. Chem.* **1985**, *195*, 109.

49. Feldberg, S. W.; Gottesfeld, S.; Redondo, A. *J. Electrochem. Soc.* **1987**, *134*, 217.

50. Belanger, D.; Davey, J.; Gottesfeld, S.; Ren, X.; Uribe, F. *J. Electrochem. Soc.* **2000**, 147, 2923.

51. Kim, K.-H.; Kim, S.-J.; Lee, K.-H.; Sung, J.-H. *J. Power Sources.* **2004**, 133, 312.

52. Inganas, O.; Lundstrom, I.; Mohammadi, A. *J. Electrochem. Soc.* **1986**, *133*, 947.

53. Davey, J.; Ferraris, J. P.; Gottesfeld, S.; Raistrick, I.; Rudge, A. *J. Power Sources*, **1993**, *49*, 87.

54. Carlberg, J. C.; Inganas, O. *J. Electrochem. Soc.* **1997**, *144*, L61.

55. Goodenough, J. B.; Lee, H. Y. *J. Solid State Chem.* **1999**, 144, 220.

56. Anderson, M. A.; Chapman, T. W.; Pang, S.-C. *J. Electrochem. Soc.* **2000**, 147, 444.

57. Hu, C.-C.; Wang, C.-C. *J. Electrochem. Soc.* **2003**, 150. A1079.

58. Athouel, L.; Belanger, D.; Brousse, T.; Crosnier, O.; Dugas, R.; Toupin, M. *J. Electrochem. Soc.* **2006**, 153, A2171.

59. Anderson, M. A.; Liu, K. C.; *J. Electrochem. Soc.* **1996**, 143, 124.

60. Srinivasan, V.; Weidner, J. W. *J. Electrochem. Soc.* **1997**, 144, L210.

61. Srinivasan, V.; Weidner, J. W. *J. Electrochem. Soc.* **2000**, 147, 880.

62. Hu, C.-C.; Huang, Y.-H. *J. Electrochem. Soc.* **1999**, 147, 2465.

63. Carette, P. L.; Hagans, P. L.; McKeown, D. A.; Rolison, D. R.; Russell, A. E.; Swider, K. E. *J. Phys. Chem. B* **1999**, 103, 4825.

64. Haran, B. S.; Popov, B. N.; Ramani, M.; White, R. E. *J. Electrochem. Soc.* **2001**, 148, A374.

65. Kim, I.-H.; Kim, K.-B. *Electrochem. Solid-State Lett.*, **2001**, 4, A62.

66. Boodts, C.; de Andrade, A. R.; Zanta, C. L. P. S. *J. Appl. Electrochem.* **2000**, *30*, 467.

67. Trasatti S. *Electrochim. Acta*, **1991**, 36, 225.

68. De Battisti, A.; Ferro, S. *J. Phys. Chem. B* **2002**, *106*, 2249.

69. Chang, C.-C.; Wen, T.-C. *J. Appl. Electrochem.* **1997**, *27*, 355.

70. Hagans, P. L.; Long, J. W.; Rolison, D. R.; Swider, K. E. *Langmuir*, **1999**, 15 774.

71. I.D.Raistrick, in *The Electrochemistry of Semiconductors and Electronics-Process and Devices*, J. Mchardy and F. Luduig, Editors, p. 297, Noyes, Park Ridge, NJ (1992).

72. Dmowski, W.; Egami, T.; Love, C. T.; Rolison, D. R.; Swider-Lyons, K. E. *J. Phys. Chem. B* **2002**, *106*, 12677.

73. Goodenough, J. B.; Yamada, A. *J. Electrochem. Soc.* **1998**, *145*, 737.

74. Long, J.-W.; Merzbacher, C. I.; Rolison, D. R.; Swider, K. E. *Langmuir*, **1999**, 15 780.

75. Conway, B. E.; Liu, T.; Pell, W. G. *Electrochim. Acta* **1997**, *42*, 3541.

76. Kvastek, V.; Horvat-Radosevic, V. *J. Electroanal. Chem.* **2001**, *511*, 65.

77 Chang, K.-H.; Chen, W.-C.; Hu, C.-C. *J. Electrochem. Soc.*, **2004**, 151, A281.

78. Lee, Y.-H.; Kim, I.-H.; Kim, J.-H.; Kim, K.-B. *J. Electrochem. Soc.*, **2005**, 152, A2170.

79. Dunn, B.; Rolison, D. R. *J. Mater. Chem.* **2001**, *11*, 963.

80. Rolison, D. R. *Science* **2003**, *299*, 1698.

81. Anderson, M.L.; Rolison, D.R.; Stroud, R.M. *NanoLett* **2002**, *2*, 235.

82. Anderson, M. L.; Elder, I. A.; Leventis, N.; Merzbacher, C. I.; Rolison, D. R. *Chem. Mater.* **1999**, *11*, 2837.

83. Kutsch, B.; Lyon, O.; Mennig, M.; Schmidt, H.; Schmidt, M. *J. Non-Cryst.* **1997**, *217*, 143.

84. Alber, K. S.; Cox, J. A. *Mikrochim. Acta* **1997**, *127*, 131.

85. Gesser, H. D.; Goswami, P. C. *Chem. Rev.* **1989**, *89*, 765.

86. Hench, L. L.; West, J. K. *Chem. Rev.* **1990**, *90*, 33.

87. Hagans, P. L.; Merzbacher, C. I.; Rolison, D. R.; Swider, K. E. *Chem. Mater.* **1997**, *9*, 1248.

88. Kumagai, N.; Kumagai, N.; Pereira-Ramos, J. P. *J. Power Sources* **1995**, *56*, 87.

Chapter 2

Materials, Methods and Instrumentation

2.1 Chemicals and Materials

All chemicals and materials were used as received. Two different types of carbon black were used as the carbon support materials: Vulcan XC72 (Cabot Corp.), with a specific area of 250 m^2 g^{-1} and Black Pearls 2000 (Cabot Corp.), with a specific area of 1500 m^2 g^{-1}. For the sol-gel materials, $RuCl_3 \cdot xH_2O$ from both Sigma-Aldrich, Inc. (ca. 41% Ru) and Precious Metals Online, Ltd. (43% Ru) was used as the ruthenium precursor, while titanium(IV) isopropoxide ($Ti(O^iPr)_4$), 97% (Sigma-Aldrich, Inc.) was used as the titanium precursor. $RuCl_3 \cdot xH_2O$ (Precious Metals Online, Ltd.) was also used as the ruthenium precursor for the carbon-supported composites. $NaBH_4$ (BDH, Inc.) was used as the reducing agent for the ruthenium precursor. Finally, Toray Carbon Fibre Paper (CFP), (TGP-H-090, FuelCellStore.com) which was 78% porous with a 0.28 mm thickness was used as the supporting electrode material during composite fabrication and testing.

2.2 Electrochemical Instruments and Measurements

A Pine Instrument Company Potentiostat coupled with customized data acquisition software was used to perform the majority of cyclic voltammetry (CV) measurements. Other CV measurements were made using a Solartron 1286 electrochemical interface. All voltammetry measurements were performed in a three-electrode cell using the composite chemically modified electrode (CME) as the working electrode with a saturated calomel electrode (SCE) as the reference electrode and Pt wire as the counter electrode. 0.5 M H_2SO_4 was used as the electrolyte in all experiments.

Prior to all measurements, the cell was sealed with parafilm and the electrolyte was degassed with N_2 for at least 15 minutes.

Capacitance was calculated according to the following equation:[1]

$$C = \frac{i}{\nu} \qquad \text{(Equation 2.1)}$$

where C is the capacitance in farads, i is the response current in amps, and v is the scan speed, $\pm\ dV/dt$ in volts per second. It should be noted that CFP by itself produces a negligible background current (on the order of tens of microamperes) and thus was considered negligible when calculating the capacitance.

2.3 X-ray Photoelectron Spectroscopy

X-ray photoelectron spectroscopy (XPS) spectra for composite materials were acquired using a VG Microtech MultiLab ESCA 2000 XPS system. An MgK_α (0.7 eV) X-ray source was used at an operating voltage of 14.6 kV. All experiments were conducted under high vacuum between 1.5×10^{-8} to 1.5×10^{-9} Torr at an initial x-ray energy of 1253.6 eV. To mount the samples, double sided adhesive tape was placed on the sample stub. The composite powder was then sprinkled onto the adhesive with no applied pressure and the stub was inverted to liberate any loose powder. This process was repeated until the stub was evenly coated with sample with no loose powder evident.

2.4 X-ray Diffraction

X-ray diffraction (XRD) patterns of the carbon-supported ruthenium oxide composites were obtained using a Rigaku D/Max-2200V-PC x-ray diffractometer. A Cu

K_α source (λ = 1.5418 Å) was used for x-ray generation. The scans were typically performed from 10.0 degrees to 90.0 degrees at an average scan rate of 6.0 degrees per minute. To mount the samples, a small portion of the composite was mixed with a small amount of isopropanol on the glass slide substrate, then spread as evenly as possible. This process was repeated to ensure an even distribution of the composite on the slide.

2.5 Transmission Electron Microscopy

Transmission electron microscopy (TEM) images were acquired using a Zeiss 109 high resolution TEM at an operating voltage of 70 keV. Composite samples for TEM measurements were prepared as follows: approximately 2 mg of the composite was dispersed in 5.0 mL of absolute ethanol via sonication for 30 min. A drop of the resulting ink was then deposited onto a carbon-coated copper grid and dried at room temperature.

2.6 Preparation of Electroactive Materials and Electrodes for Supercapacitors

2.6.1 Preparation of Sol-Gels

The ruthenium-titanium oxide sol-gel precursor solutions were prepared according to a procedure developed by Rolison *et al.*[2] First, $RuCl_3 \cdot xH_2O$ was refluxed in absolute ethanol (abs-EtOH) for approximately 1.5 to 2 hours to create a 9.1 wt % solution of $RuCl_3$ in ethanol. This was then combined with DDW and the acid catalyst, concentrated HNO_3, to form the ruthenium precursor solution. Separately, titanium(IV) isopropoxide ($Ti(O^iPr)_4$) was combined with abs-EtOH at room temperature to create the titanium precursor solution. The precursor solutions were then combined using two

different methods to form the sol-gel (see Section 2.6.3). The gelation time for different sol-gels batches was variable, on average taking 5 minutes to as little as 45 seconds.

2.6.2 Preparation of Carbon-Supported Ruthenium Oxide Composites

The ruthenium-carbon composites were prepared as follows: x milligrams of either Vulcan Carbon XC-72 or Black Pearls 2000 were combined with 30 mL of distilled deionized water (DDW). Next, $(100 - x)$ mg of the $RuCl_3 \cdot xH_2O$ precursor was combined with 30 mL of DDW. The ruthenium precursor solution was then added dropwise to the carbon black suspension with stirring and sonication. Next, an aqueous solution containing a 2 times molar excess of $NaBH_4$ was added to the ruthenium precursor / carbon black solution with stirring and sonication. The final product was collected via suction filtration and rinsed with copious amounts of DDW. The composites were air-dried for at least 24 hours prior to electrode preparation.

2.6.3 Preparation of Chemically Modified Electrodes

Chemically modified electrodes (CMEs) incorporating the carbon-supported ruthenium composites were prepared as follows: carbon fibre paper (CFP) strips were cut with dimensions 3.0 cm (l) x 0.4 cm (w) x 0.025 cm (d). To make the CMEs, both inks and pastes of the composites were prepared using small amounts of isopropanol (0.1 to 0.5 mL) and/or Nafion binder (1% w:w). The pastes were spread onto the CFP electrode surfaces using a spatula, while the inks were used to impregnate the CFP using a fine

brush. All CMEs were air-dried for at least 12 hours prior to electrochemical characterization.

To prepare CMEs incorporating the sol-gels, two different methods were used, dubbed SG1 and SG2. The SG1 method was used in initial experiments, where the bulk ruthenium solution was added to the bulk titanium solution in air with stirring to form the sol, as outlined by Rolison *et al.* The rapidly gelling sol was then portioned out into individual vials in 0.3 mL volumes into which CFP strips were inserted to form the CMEs. However, gelation as rapid as 45 seconds made allocation of the sol-gel into vials for electrode fabrication difficult. In addition, the sol was often not able to soak through the CFP as gelation often took place before the strips could be inserted. Thus, Rolison's method was modified to produce the SG2 method, in which the CFP strips were individually soaked in equal volumes of the titanium precursor solution in separate glass vials. Next, appropriate volumes of the ruthenium precursor solution were added to each glass vial followed by sonication for ca. 1 minute to form individual sols. This ensured that gelation would take place within the porous matrix of the CFP with a relatively uniform distribution of the sol-gel.

2.7 References

1. Conway, B. E. *Electrochemical Capacitors: Scientific Fundamentals and Technological Applications*, New York: Kluwer Academic / Plenum Publishers, 1999.

2. Hagans, P. L.; Merzbacher, C. I.; Swider, K. E.; Rolison, D. R. *Chem. Mater.* **1997**, *9*, 1248.

Chapter 3

Preparation and Characterization of Ruthenium Oxide-Titanium Oxide Sol-Gels for Use in Supercapacitors

3.1 Introduction

In recent years, sol-gels of different chemical compositions have been used as electroactive electrode materials in supercapacitors. For example, MnO_2 sol-gels have gained popularity for use in supercapacitors due to their ease of preparation and low cost.[1-3] Specific capacitances as high as 698 F g^{-1} have been claimed for dip-coating sol-gel derived MnO_2 films on nickel foil.[3] NiO_x sol-gels[4,5] have been used recently due to their low cost and toxicity.[4] A specific capacitance of 696 F g^{-1} has been reported for sol-gel derived NiO_x xerogels in 7 M KOH electrolyte.[4] Sol-gel derived CoO_x xerogels[6] have also been studied, with specific capacitances ranging from 192 to 450 F g^{-1}.

The most widely studied sol-gel material for supercapacitors and perhaps the most important, is RuO_2. The specific capacitance of 720 F g^{-1} reported by Jow *et al.*[7] for amorphous $RuO_2 \cdot xH_2O$ prepared as a sol-gel has become a standard of sorts for supercapacitor material research. Due to the high cost of ruthenium, several studies of binaries containing sol-gel derived ruthenium oxide have been undertaken in order to decrease the amount of RuO_2 needed to attain high values of capacitance. For example, ruthenium-tin oxides created via a sol-gel process and annealed in air between 150°C and 250°C yielded a maximum specific capacitance of 860 F g^{-1} for the RuO_x component.[8] The sol-gel binary was found to be more stable and capacitive than Ru-Sn oxides generated via a co-annealing method.[9] Ruthenium-iridium oxides have also been studied as potential supercapacitor materials.[10]

One binary which has potential as a capacitive material is ruthenium-titanium oxide. In the chloro-alkali industry, RuO_2-TiO_2 electrodes are used as anodes for the

production of chlorine gas from brine.[11] More recently, Ru-Ti oxides have been produced via sol-gel methods in order to ascertain their potential for use in supercapacitors. According to Rolison *et al.* the surfaces of the bulk aerogel form of RuO_2-TiO_2 are comprised of highly defective hydrous RuO_2 and/or (Ru-Ti)O_x which insulates the electronically conductive hydrous RuO_2 regions.[12] As such high electronic conductivity of such materials cannot be achieved, which translates into poor capacitive capabilities. A specific capacitance of only 1.2 F g^{-1} was obtained for these (Ru-Ti)O_x aerogels,[13] suggesting that the conductive RuO_2 regions were indeed insulated in the aerogel structure. To overcome this problem, it appears necessary to ensure that the RuO_2 domains remain hydrated and that the sol-gel remains amorphous.

It was reasoned that Ru-Ti oxide sol-gels which were not supercritically dried and annealed to produce aerogels would yield hydrated amorphous materials suitable for use in supercapacitors. Hence, this chapter reports the sol-gel synthesis and electrochemical measurements of RuO_2-TiO_2 hydrogels. Several experimental difficulties are identified and explained, and different temporary and long-term solutions are explored. For select electrodes where experimental difficulties do not bias the results, capacitance values are reported and discussed.

3.2 Experimental

3.2.1 Chemicals and Materials

$RuCl_3 \cdot xH_2O$ (Sigma-Aldrich Inc.) was used as the ruthenium precursor and titanium(IV) isopropoxide ($Ti(O^iPr)_4$) (Sigma-Aldrich, Inc.) was used as the titanium

precursor. Concentrated HNO_3 (Aristar) was used as the acid catalyst during sol-gel formation.

3.2.2 RuO_2-TiO_2 and TiO_2 Sol-Gels

The RuO_2-TiO_2 sol-gels were prepared as outlined in Section 2.6.1 and 2.6.3 using (Ru+Ti):H_2O:H^+:EtOH mole ratios of 1:4:0.08:20. The sol-gels produced were a dark, non-transparent brown colour. When CME results are displayed, the method of preparation for the sol-gel batch used is indicated (either SG1 or SG2).

The TiO_2 sol-gels were prepared using Ti:H_2O:H^+:EtOH mole ratios of 1:4:0.08:20. Initially, the $Ti(O^iPr)_4$ precursor was combined with abs-EtOH with stirring. Separately, the HNO_3 acid catalyst was combined with DDW to form the catalyst solution. The two were then combined using the SG2 method to form the sol (see Section 2.6.3). Gellation typically took place within 1 minute. The resultant gel was a cloudy, semi-transparent off-white colour. All gels were aged at least 24 hours prior to characterization.

3.2.3 Chemically Modified Electrode Preparation

CMEs were prepared as outlined in Section 2.6.3. Prior to CME fabrication, all CFP strips used were weighed on an analytical balance. Upon gelation, the CMEs were removed from their vials and any loosely attached gel was scraped off with a spatula. As the sol-gel solvent evaporated, the wet hydrogel CMEs were weighed to constant mass on an analytical balance. The mass loss due to evaporation was typically 20 to 25 mg,

indicating significant solvent content in the gels. The CMEs were then weighed a second time. This was used to determine the final mass of the sol-gel in the CFP by subtraction of the CFP mass. All masses were recorded to four decimal places (0.0001 g).

In initial experiments, noticeable background currents resulting in baselines shifts were observed in a large portion of CVs. This issue involved the corrosion of the electrical leads at the point of contact with the CMEs. This was due to the $H_2SO_{4(aq)}$ electrolyte soaking up through the CFP electrode material via capillary action to the contact point with the leads. This experimental issue and its impact upon initial results is discussed in Section 3.3. To remedy the problem, the central regions of the strips were impregnated with a hexane/paraffin wax solution to stop the corrosion of the potentiostat's leads. The presence of the wax prevented the capillary action of acidic electrolyte through the CFP electrode to the point of contact with the leads. This method was used for the remainder of the sol-gel CME measurements.

3.2.4 Electrochemical Measurements

The sol-gel CMEs were characterized by cyclic voltammetry. The current was measured from 0 V to +0.8 V vs. SCE at a scan rate of 50 mV s^{-1}. This scan rate was used for all CVs reported herein unless otherwise stated. Capacitance was calculated according to Equation 2.1. To calculate specific capacitance, the calculated capacitance values were divided by the total mass loading of sol-gel on the electrode the calculation of which is outlined in Section 3.2.2. The specific capacitance values for both the anodic and cathodic currents were then averaged over the CV potential range, resulting in a positive

and negative average specific capacitance value, respectively. The absolute average of these two values yielded the final value of the specific capacitance of the CME and thus, the hydrogel itself.

For information on electrochemical instrumentation, see Section 2.2.

3.3 Results and Discussion

Before any sol-gel CMEs were analyzed by CV, bare CFP was measured to determine whether or not it would make a significant contribution to the background current and hence overall current. Figure 3.1 shows a CV of bare CFP in acid electrolyte.

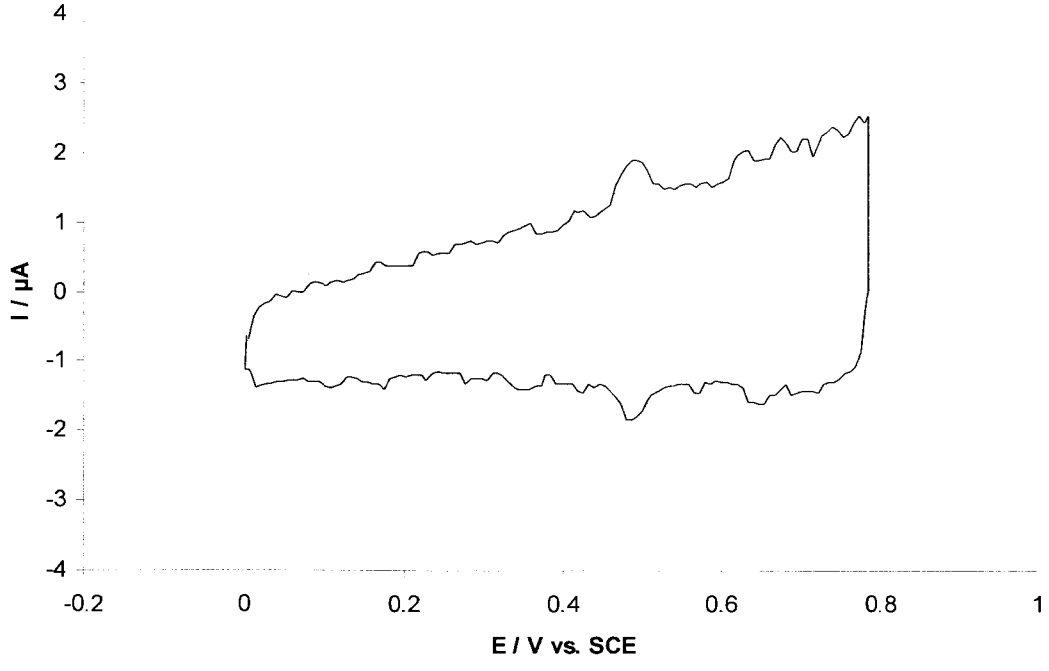

Figure 3.1. Cyclic voltammogram of bare CFP in 0.5 H_2SO_4 at 50 mV s^{-1}.

The magnitude of current produced by the CFP is very small, on the order of a few microamps in both the anodic and cathodic directions. While the CV is distinctly noisy at such a low current, its shape is mostly indicative of the double layer capacitance of the CFP. This is especially true in the negative direction, where the current response is relatively constant with decreasing potential.

Figure 3.2a shows the initial CV of a RuO_2-TiO_2 CME made from the first batch of hydrogel prepared according to the SG1 method (see Section 2.6.3). The current response was much greater than that of the bare CFP, as expected, and the faradaic features of the CV were broad and capacitive. In fact, this voltammogram would turn out to be the most ideal in terms of faradaic response and capacitive CV shape for all the RuO_2-TiO_2 hydrogels. The first two cycles of this hydrogel CME were indeed fairly capacitive, as suggested by their voltammogram shapes. The two CVs, expressed as specific capacitance against potential, can be seen in Figure 3.2b. The average specific capacitance of both cycles was ca. 10 F g^{-1}. The values were calculated as the average of the capacitances from the positive and negative sweeps at +0.4 V, the point at which the voltammogram's shape is most capacitive or "box like", i.e., the constant current with potential. This result is considerably higher than that reported for the aerogel form of RuO_2-TiO_2,[13] demonstrating the potential of RuO_2-TiO_2 hydrogels. However it is considerably less than literature values for sol-gels prepared using different materials such as MnO_2 and NiO_x.[3,4]

It was found in most cases that CMEs from the same sol-gel batch exhibited varying and often erratic electrochemical behaviour. Cyclic voltammograms for several

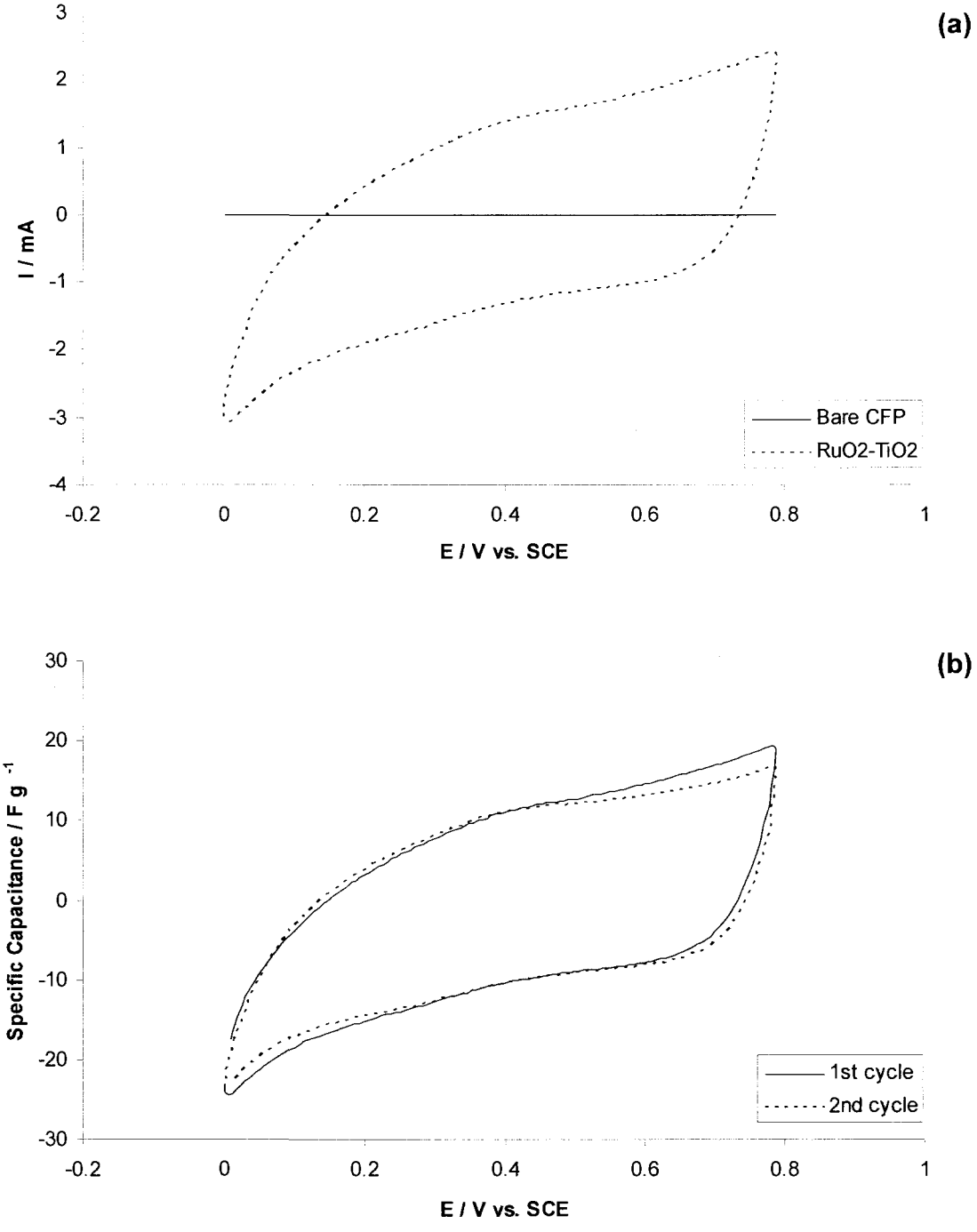

Figure 3.2. Cyclic voltammograms of a CME with a 2.5 mg RuO_2-TiO_2 loading prepared by the SG1 method displaying (a) current and (b) specific capacitance as a function of potential.

CMEs prepared from the same sol-gel batch as that of the previous figure are shown in Figure 3.3. The results are random, at best. Gel 1a produced the CV from the Figure 3.2, and acted as a reference for what would typically be possible from hydrogel CMEs. Gel 1b gave a flat, featureless CV which is linear in both the positive and negative current directions. Additionally, the magnitude of the current is more akin to that of bare CFP, indicating either very little electroactive Ru material or a very high resistance. Finally, Gel 1d displays a current magnitude more comparable to that of the Gel 1a, but has an

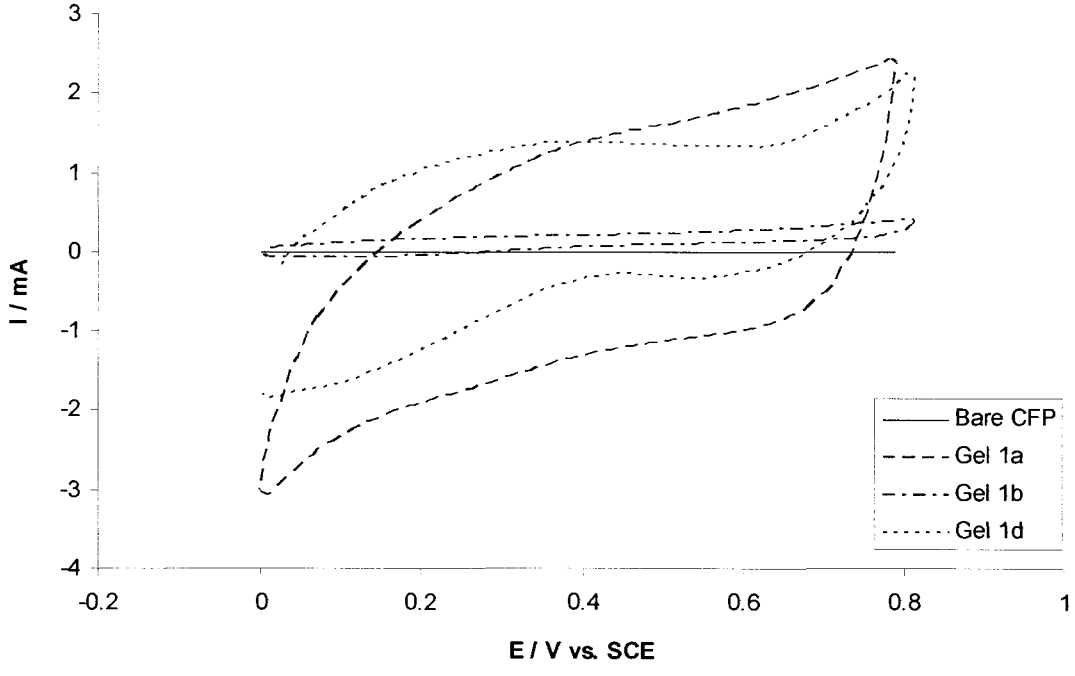

Figure 3.3. Cyclic voltammograms for RuO_2-TiO_2 CMEs of the same sol-gel batch prepared with the SG1 method. Mass loadings for Gels 1a, 1b and 1d were 2.5 mg, 4.8 mg and 2.5 mg, respectively.

unexpected, misshapen CV which is possibly indicative of an irreversible reaction taking place at the electrode surface.

In either event, the issue of shifted, sloping baselines due to high background currents was observed for almost all CMEs prepared from different RuO_2-TiO_2 sol-gel batches of the same composition. Figure 3.4 illustrates this point with several CVs exhibiting the same sloping baseline behaviour. While these CVs attained relatively high current levels, they exhibited high background currents. A capacitive CV would be

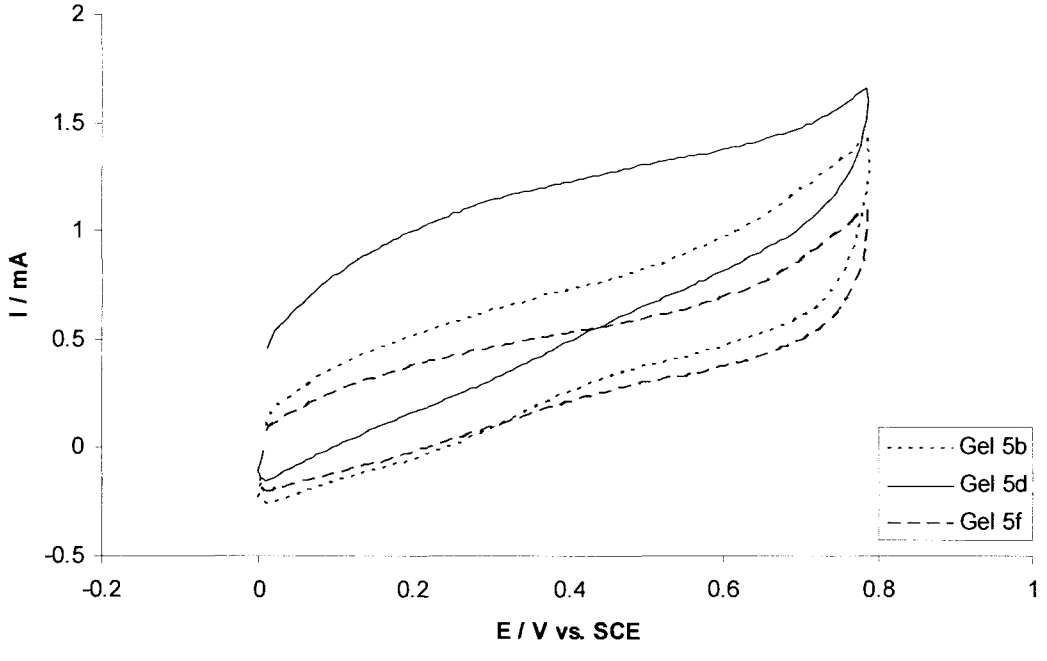

Figure 3.4. Cyclic voltammograms for RuO_2-TiO_2 CMEs from the same hydrogel batch highlighting the sloping baseline issue. Mass loadings for Gels 5b, 5d and 5f were 1.0 mg, 1.7 mg and 3.5 mg, respectively.

expected to produce a steep drop in current to negative current values in the reverse direction which would cross the potential axis within ca. +0.1 V from the upper limit, i.e., a small resistance-capacitance (RC) time constant. This is not observed in the negative sweeps of Figure 3.4. This linear relation between current and potential was suggestive of a high background current originating somewhere in the experimental setup, the consequences of which were sloping and somewhat shifted baselines yielding undesirable CV shapes. A comparison of CVs with shifted and relatively normal baselines is shown in Figure 3.5 to illustrate this point. The CV with the relatively normal baseline displays a more ideal "box-like" capacitive shape, wherein minor changes are current are observed with the changing applied potential. The CV with the shifted baseline does show this trend in the positive direction, but not the negative direction, where the current would normally change sign. As a result, the true capacitance of the CME becomes difficult to ascertain. It is conceivable that if the background currents in the setup were not present, the shifted baseline CV would be able to yield faradaic features in the reverse direction analogous to those of CVs with normal baselines.

It was initially unknown that the high background current problem originated in the electrochemical system setup and not in the CMEs themselves. As such, it was believed necessary to retrace the steps to the RuO_2-TiO_2 sol-gel formation to ensure that no errors were made during synthesis. As such, TiO_2 sol-gels were synthesized and CMEs prepared as outlined in Sections 3.2.2 and 2.6.3. During the course of testing the TiO_2 CMEs, it was observed that electrolyte was soaking up through the CFP to the point of contact with the lead. Upon further inspection, portions of the leads (specifically the teeth

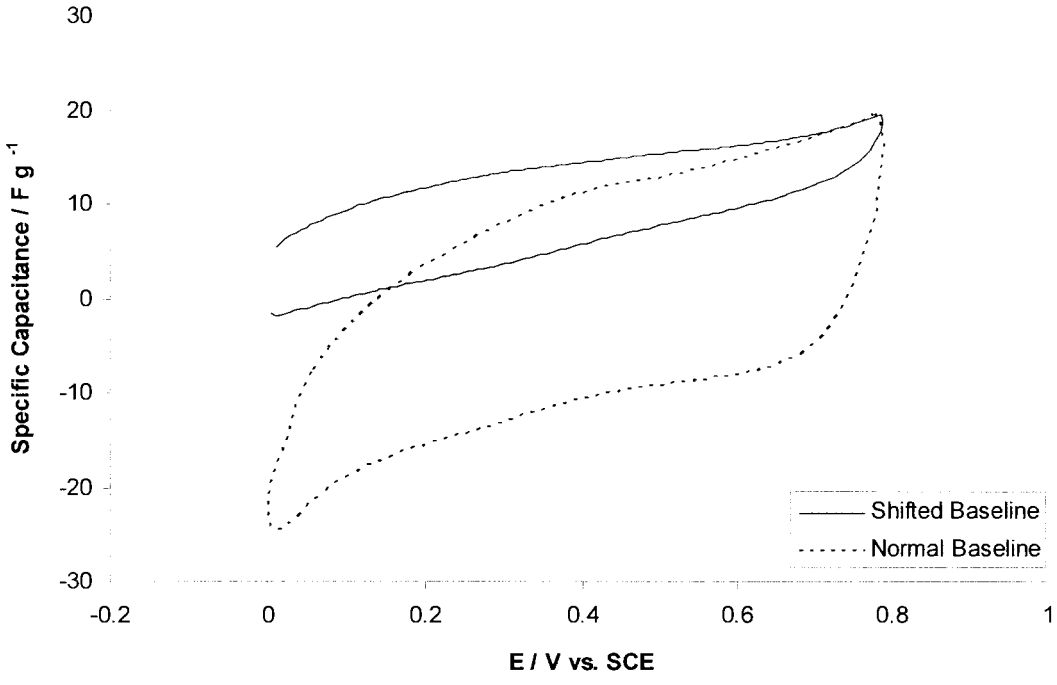

Figure 3.5. Comparison of cyclic voltammograms with normal and shifted baselines.

of the alligator clips) were found to be noticeably corroded. It was believed that this was the source of the high background currents during CV measurements. In order to test this, a small piece of platinum foil (which is corrosion resistant) was affixed to a bare CFP electrode at the point of contact with the lead. The lead was clipped onto the Pt foil and CV was performed, as shown in Figure 3.6. The noise level in the CV was greatly reduced and the shape of the CV was more characteristic of the expected double layer charging.

It was hoped that this modification would eliminate the background observed for the hydrogel modified CMEs. This was found to be the case for TiO_2 modified CMEs

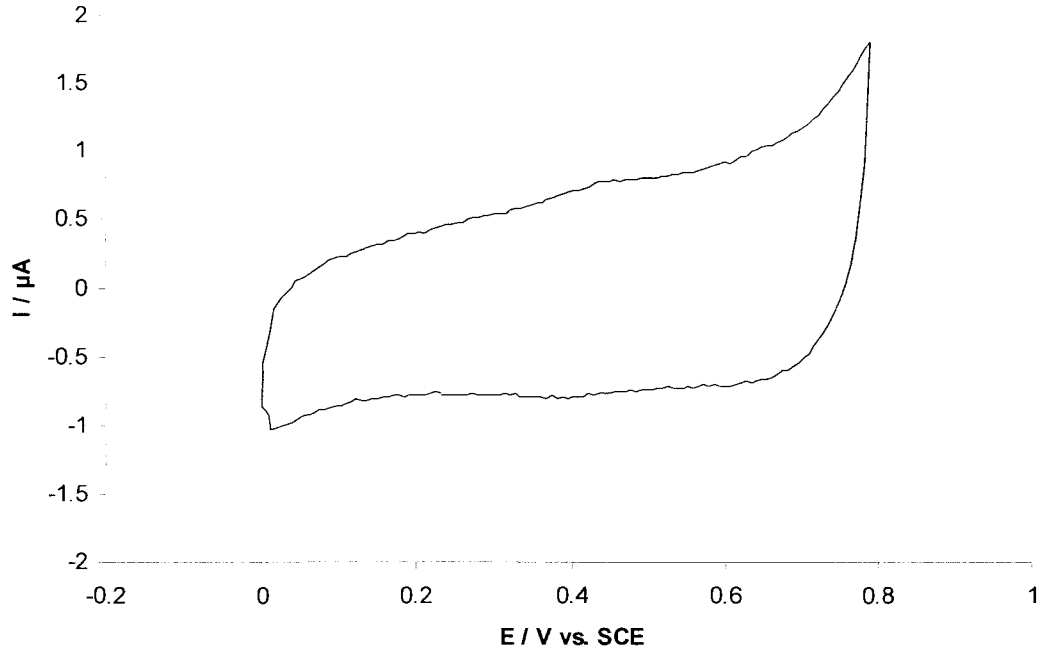

Figure 3.6. Cyclic voltammogram of a bare CFP electrode with Pt foil affixed to the lead contact point.

using Pt foil, as illustrated in Figure 3.7. When the lead was in direct contact with the electrode during CV, a high background current was observed, producing offset current values. When a chrome clip was used, the same result was observed, albeit with a smaller current offset. However, the lead was still susceptible to corrosion, resulting in background current. Finally, when Pt foil was used at the point of contact, the CV was far more characteristic of a capacitive current response, although a small background current was still evident in the CV. However, the magnitude of the current was greatly reduced, which was an expected result as TiO_2 by itself is an insulator and hence poorly conductive. This confirmed that modifying the electrode setup to prevent lead corrosion

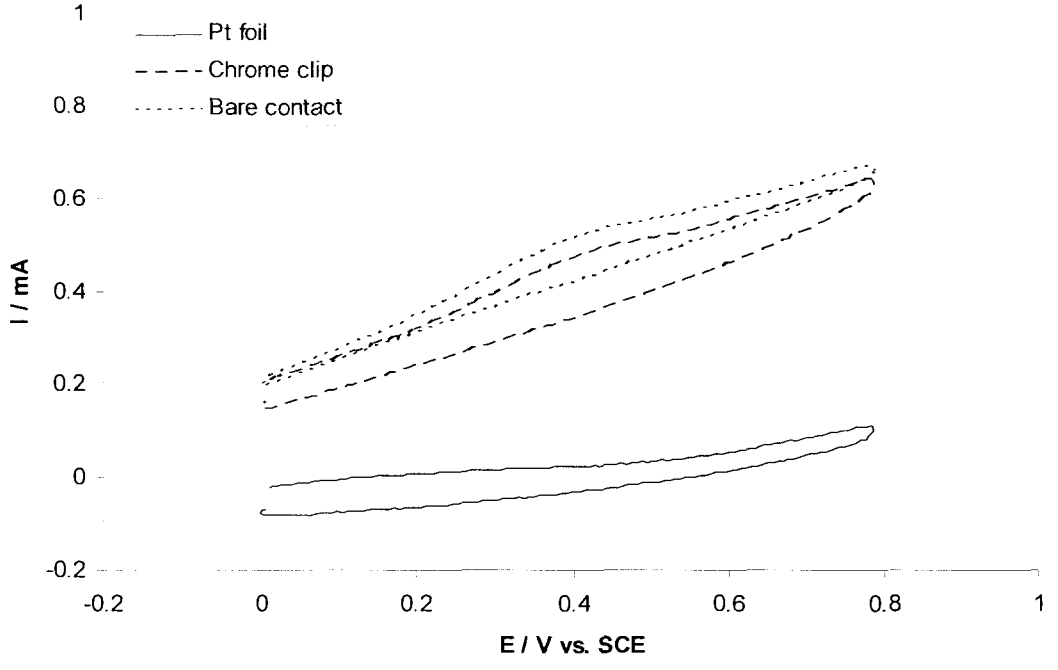

Figure 3.7. Cyclic voltammograms demonstrating the effect of modifying CFP electrode contact points for several TiO_2 CMEs.

greatly reduced the background problem. While these results were encouraging, the Pt foil proved difficult to work with, as it had to be attached to each individual electrode prior to CV. With time, the thin foil began to crack and break apart, prompting the need for an alternative solution. It was decided to impregnate the central regions of the strips with a hexane/paraffin wax solution as outlined in Section 3.2.3. This too prevented corrosion of the clip, as the wax impeded the capillary action of the electrolyte through the CFP, thereby eliminating the corrosion/high resistance issue while still allowing for full electrical conductivity of the electrode. Figure 3.8 shows a TiO_2 CME impregnated with hexane/paraffin wax in the central region (above the sol-gel modified region). The

result is similar to that of bare CFP, with very little noise and a capacitive current response, although the sol-gel itself was not very capacitive. The very rigid box-like shape of the CV was attributed to the wetting effect of the TiO_2. Although not very capacitive itself, the TiO_2 sol-gel formed within the pores of the CFP, coating and interconnecting the electrode's fibres. This allowed for greater wetting of the electrode surface, promoting a minor increase in the double layer capacitance and hence in the current response relative to the bare CFP (Figure 3.6). Also, the wetting promoted the rapid EDL charging when the potential reversed directions during cycling, as seen by the

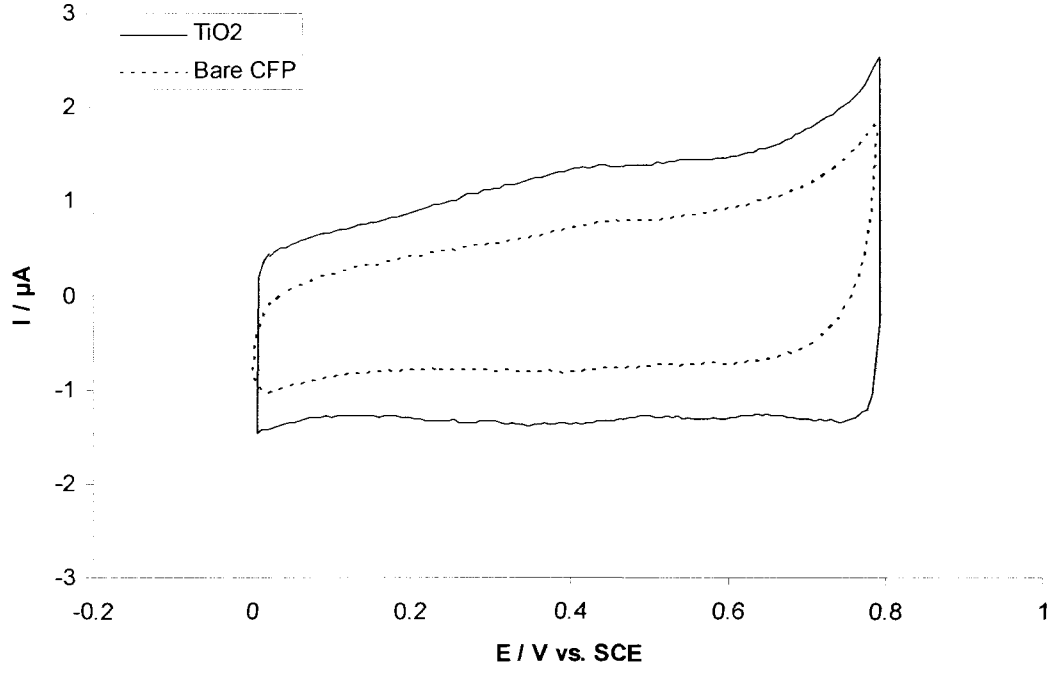

Figure 3.8. Cyclic voltammogram of bare CFP and a TiO_2 CME, the central region of which was impregnated with paraffin wax.

very RC time constant. Most importantly, the sloping baselines found in previous CVs for sol-gel CMEs was not observed, supporting the use of wax in future CFP electrodes to stop clip corrosion.

Having addressed the background current issue, fresh RuO_2-TiO_2 CMEs modified with paraffin wax were tested by CV. In order to test the stability and reproducibility of the electrodes, the CMEs were cycled repeatedly. Figure 3.9a illustrates the effect of repeated cycling on a RuO_2-TiO_2 CME prepared via the SG2 method (see Section 2.6.3). As shown, the current decreased significantly with each cycle. It was observed that while cycling, a yellow-brown discolouration was evident in the electrolyte. Upon further inspection, the discolouration was found to originate from the sol-gel modified portion of the CME. With repeated cycling, the intensity of the discolouration increased to the point where the electrolyte solution became either semi-transparent or opaque. This was believed to be due to the dissolution of ruthenium from the sol-gel in the acid electrolyte. This "leaching" of the Ru into the electrolyte corresponded with the decrease in current during cycling. In fact, after 50 cycles and heavy discolouration, the current response was similar to that of wetted TiO_2 CMEs, as shown in Figure 3.9b, suggesting almost a complete loss of ruthenium. This discolouration and corresponding current drop with cycling was observed for other RuO_2-TiO_2 hydrogel CMEs.

It was believed that the Ru leaching problem was due to one of two possibilities: either there was unreacted ruthenium precursor present in the wet hydrogel, and/or the acid electrolyte was dissolving the Ru in the sol-gel. In order to remedy the problem, several hydrogel CMEs were heated while still immersed in their bulk sol-gels. This was

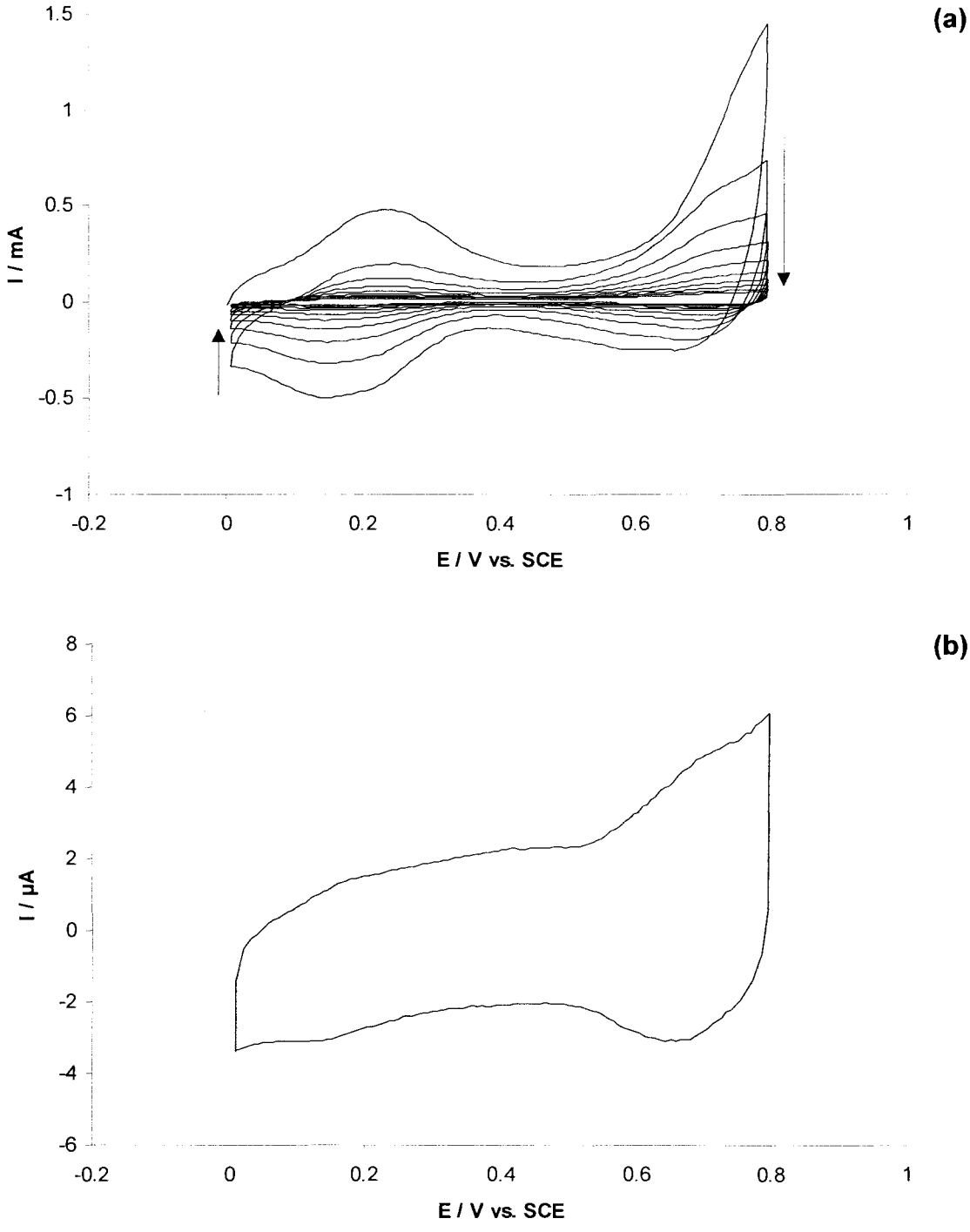

Figure 3.9. Cyclic voltammograms showing (a) the first 10 cycles and (b) the 50th cycle of an untreated RuO_2-TiO_2 CME prepared by the SG2 method. The mass loading was 1.0 mg.

done so as to maintain the amorphous structure of the sol-gels while minimizing the potential crystallization during heating. Figure 3.10a shows the initial cycles of a RuO_2-TiO_2 CME prepared by the SG2 method which was heated at ca. 64°C for 1 hour. As with the unheated sample, the current decreased with each cycle and was accompanied by increasing discolouration of the electrolyte. As shown in Figure 3.10b, after 50 cycles the current reached the microamp range, although not to the point of resembling a wetted electrode as with the unheated hydrogel CMEs. Regardless, the moderate heat treatment of the hydrogel CME did not result in increased stability of the Ru within the hydrogel.

Prolonged heating was only moderately successful at addressing the Ru leaching problem. Figure 3.11 shows the cycling of a RuO_2-TiO_2 CME (SG2 method) heat treated at 140°C in air for 4 hours. Initially, the current increased with repeated cycling; this was believed to be caused by the conversion of any unconverted Ru present in the sol-gel to RuO_2. This increase was observed for approximately 10 cycles, as shown in Figure 3.11a. However, after 10 cycles, the current began to decrease with each cycle, albeit less than previously tested CMEs. As with the other electrodes, a yellow discolouration of the electrolyte which increased in intensity with cycling was evident. The decrease in current continued through 50 cycles and onward as shown in Figure 3.11b until it dipped below that of the first cycle. Nonetheless, with the heat treatment the Ru leaching from the CME was reduced significantly, which in turn allowed the electrode to maintain higher currents and hence capacitance for longer than the untreated electrodes.

To reassess the initial increase and subsequent decrease in current of the heated CME, a second heat treated RuO_2-TiO_2 CME from the same sol-gel batch was cycled.

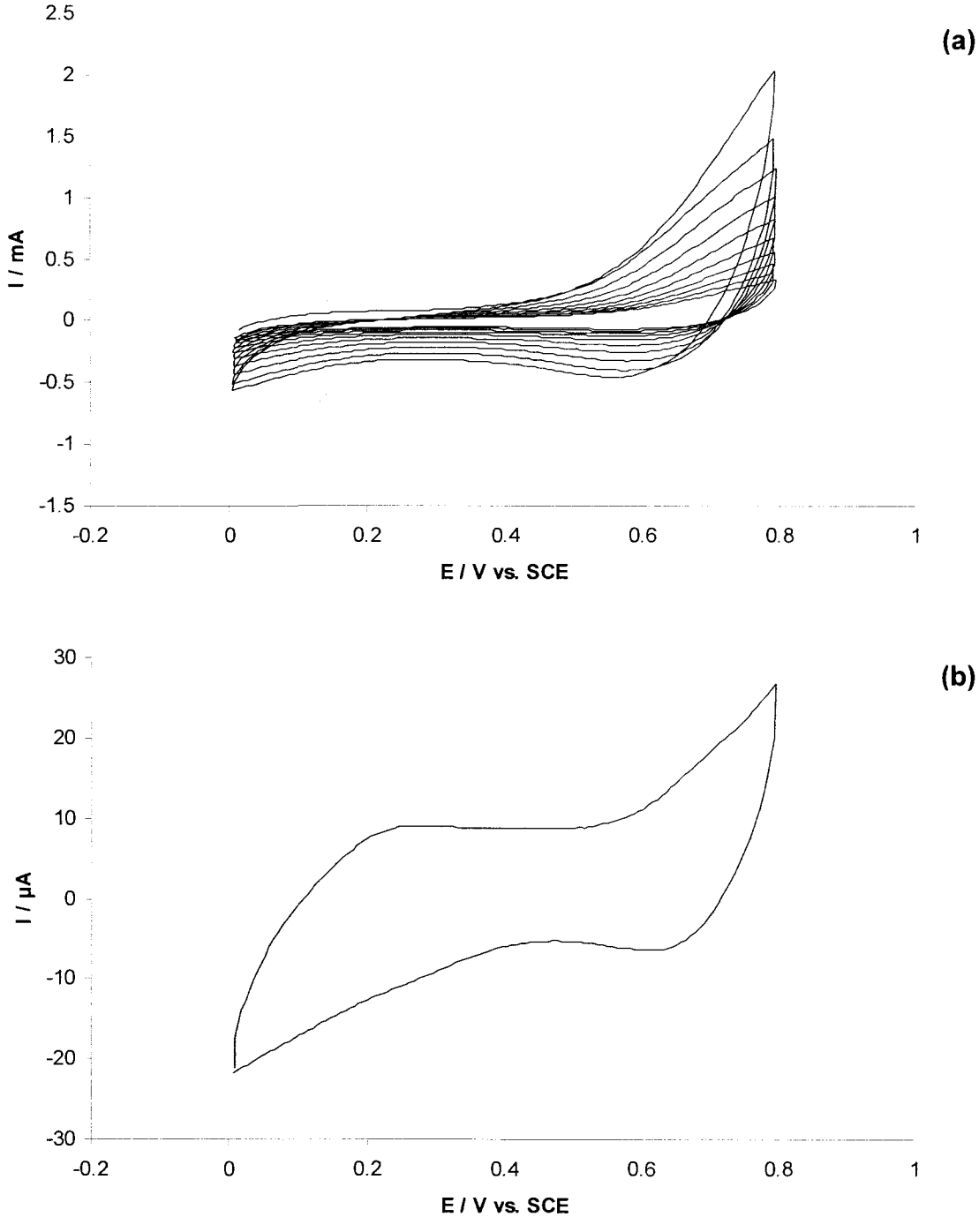

Figure 3.10. Cyclic voltammograms showing (a) the first 10 cycles and (b) the 50th cycle of a RuO_2-TiO_2 CME prepared using the SG2 method, heated at 64°C for 1 hour. The mass loading was 0.7 mg.

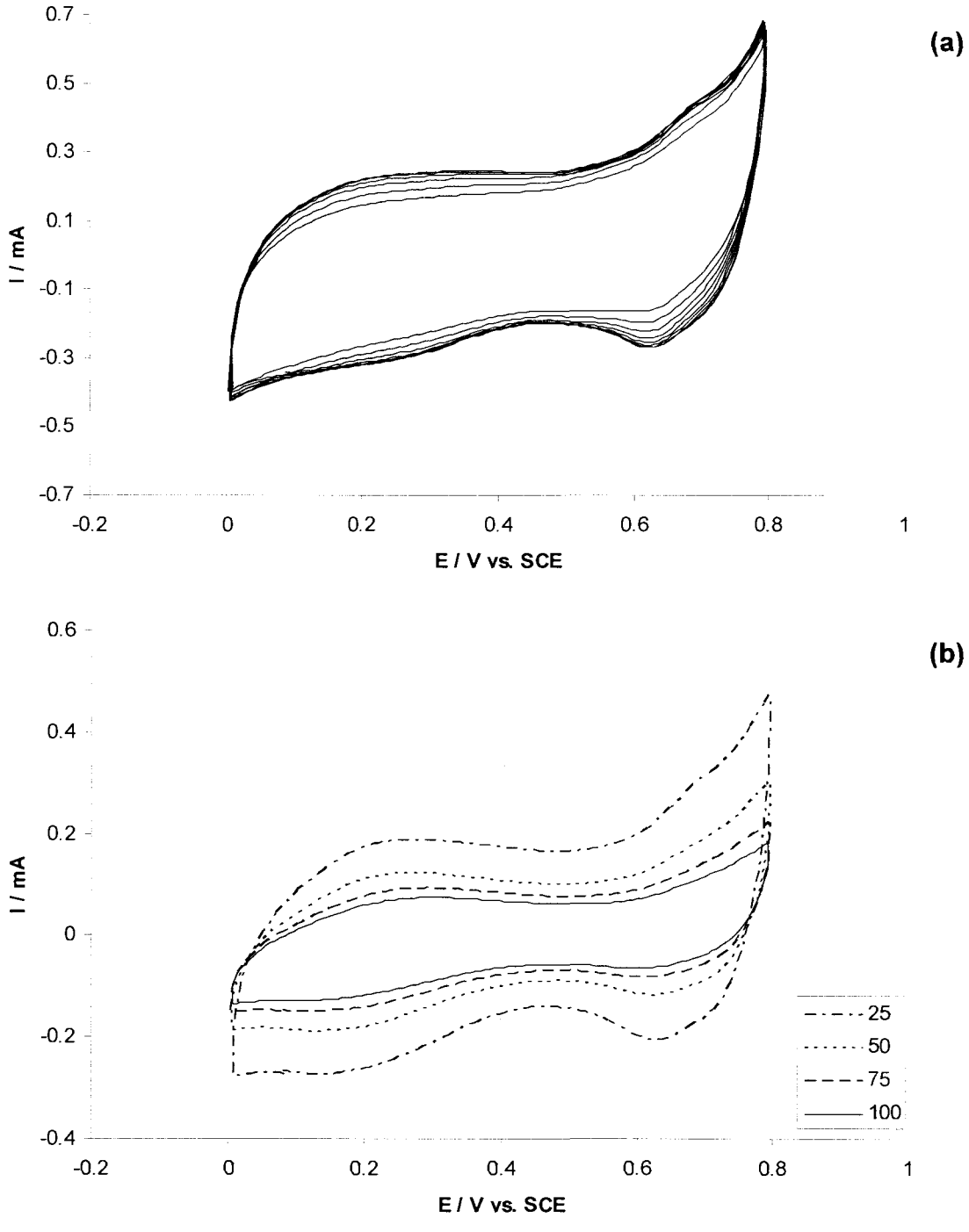

Figure 3.11. Cyclic voltammograms showing (a) the first 10 cycles and (b) select incremental cycles of a RuO_2-TiO_2 CME (SG2 method) heated at 140°C for 4 hours. The values shown in (b) indicate the cycle number. The mass loading was 0.8 mg.

This electrode produced a much different result, with no significant drop in current with successive cycles. This behaviour is illustrated in Figure 3.12. In addition, a noticeable background current was observed in the CVs; it is possible that the hexane/paraffin wax did not completely prevent the capillary action of the electrolyte. Finally, there was only a slight discolouration of the electrolyte, suggesting that despite the apparent shifts in the CVs, some Ru was lost when cycling near the potential limits. The two very different results for RuO_2-TiO_2 CMEs prepared using the same bulk sol-gel indicates that better

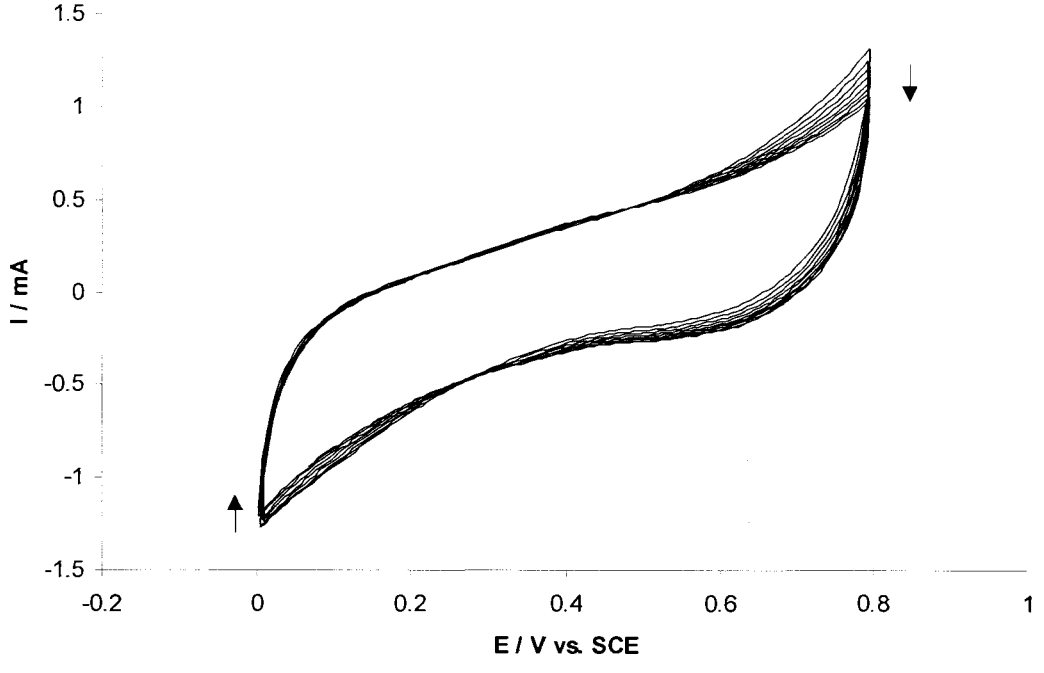

Figure 3.12. Repeated cycling of a RuO_2-TiO_2 CME (SG2 method) heated at 140°C for 4 hours.

control of the heat treatment process is required to fix the Ru leaching and hence produce CMEs with consistent current responses.

Since the acidic electrolyte was believed to be dissolving the RuO_2 in the sol-gel, especially at higher potentials, a 0.1 M potassium phosphate buffer solution, pH ~ 7.5 was substituted as the electrolyte to test for Ru leaching. Figure 3.13 shows repeated cycling in the phosphate buffer of a RuO_2-TiO_2 electrode heat-treated at ca. 150°C for 4 hours. The current response remained fairly constant with repeated cycling, especially in the range of -0.4 V to +0.4V. Towards the upper and lower potential limits, the current

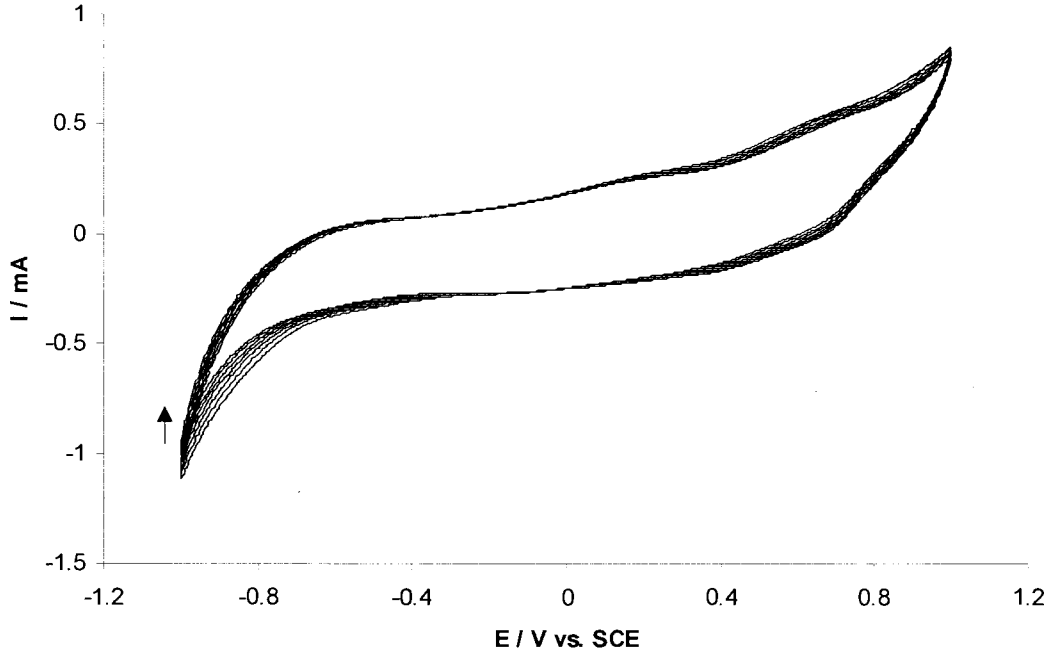

Figure 3.13. Cyclic voltammograms of a RuO_2-TiO_2 CME (SG2 method) heated at 150°C for 4 hours cycled in 0.1 M potassium phosphate buffer, pH ~ 7.5.

appeared to decrease slightly. Only the faintest trace of yellow discolouration was observed in the buffer solution, suggesting that the CMEs were more stable in higher pH electrolytes. However, the stability of the electrode did not translate into better capacitance. The average specific capacitance for the CME was ca. 2.6 F g^{-1}, less than what was hoped for yet similar to values reported in literature.[13]

At this point, it was decided that the RuO_2-TiO_2 CMEs were not performing as desired. Consequently, other methods of producing capacitive materials incorporating RuO_2 were sought.

3.4 Conclusions

Synthesizing stable, capacitive RuO_2-TiO_2 hydrogels via the sol-gel method proved challenging, as problems were encountered during different steps of electrode fabrication and testing. While initial CV measurements showed promise, the results were not reproducible. Initial difficulties caused by high background currents due to corrosion of the electrode clip resulted in lost productivity and often peculiar measurements. The results that were obtained were for the most part inconsistent, even amongst electrodes prepared from the same sol-gel batch. The use of Pt foil and eventually CFP impregnated with wax resolved the background current setback. However, new issues arose with the gels themselves. Ruthenium dissolution in the acidic electrolyte reduced the potential capacitance of the RuO_2-TiO_2 CMEs. The significant leaching problem with the hydrogels prompted the use of moderate heat treatment to encourage stability. This did mostly resolve the Ru dissolution issue in acid electrolyte, as evidenced in Figures 3.12

and 3.13. Overall, the lack of stability caused by persistent Ru leaching was a significant concern for the RuO_2-TiO_2 hydrogels.

The capacitance performance of the hydrogel CMEs showed promise however, with an average specific capacitance of 10 F g^{-1} on the first cycle for the best CME. This is comparatively high for RuO_2-TiO_2 sol-gels,[13] although substantially smaller than values reported in literature for other RuO_2-based capacitive materials.[7,8] Although annealing the gels produced CMEs with lower current responses which decreased with repeated cycling, it did solve the Ru leaching issue and increase stability. Unfortunately, heating the sol-gels negated the objective of testing the wet hydrogels for capacitance without annealing.

Overall, the RuO_2-TiO_2 hydrogels reported herein had variable stability which yielded inconsistent capacitance measurements, making the gels largely unsuitable for use as potential supercapacitor materials. As the wet hydrogels did not yield CMEs of increased capacitance as hoped, further refinement of the preparation of RuO_2-TiO_2 sol-gels is required. This includes a more controlled annealing process to find temperature and heating duration parameters which optimize the stability and capacitance of the gels.

3.5 References

1. Reddy, R. G.; Reddy, R. N. *J. Power Sources*, **2003**, 142, 330.

2. Athouel, L.; Belanger, D.; Brousse, T.; Crosnier, O.; Dugas, R.; Toupin, M. *J. Electrochem. Soc.* **2006**, 153, A2171.

3. Anderson, M. A.; Chapman, T. W.; Pang, S.-C. *J. Electrochem. Soc.*, **2000**, 147, 444.

4. Cao, G.-P.; Cheng, J.; Yang, Y.-S. *J. Power Sources*, **2006**, 159, 734.

5. Chen, A.; Gao, J.; Wu, M. *J. Porous Mater.*, **2006**, 13, 407.

6. Kim, H. J.; Park, S. G. *Electrochemistry*, **2001**, 69, 848.

7. Cygan, P.J.; Jow, T.R.; Zheng, J.P. *J. Electrochem. Soc.* **1995**, 142, 2699.

8. Hu, C.-C.; Wang, C.-C. *J. Electrochem. Soc.* **2005**, 150, A370.

9. Chang, K.-H.; Hu, C.-C.; Wang, C.-C. *Electrochim. Acta*, **2007**, 52, 2691.

10. Chang, K.-H.; Hu, C.-C.; Huang, Y.-H. *J. Power Sources.*, **2002**, 108, 117.

11. Trasatti S. *Electrochim. Acta*, **1991**, 36, 225.

12. Hagans, P. L.; Merzbacher, C. I.; Rolison, D. R.; Swider, K. E. *Chem. Mater.*, **1997**, 9, 1248.

13. Long, J.-W.; Merzbacher, C. I.; Rolison, D. R.; Swider, K. E. *Langmuir*, **1999**, 15 780.

Chapter 4

Preparation and Characterization of Carbon-Supported Ruthenium Oxide Composites for Use in Supercapacitors

4.1 Introduction

In the past 10 years, supercapacitors have emerged as a promising technology for energy storage due to their high power densities, long life cycles, good stability, low impedance and rapid charging capabilies.[1,2] These pulse power devices have applications in portable electronics, surge-power delivery systems in hybrid and electric vehicles, backup power sources and weapon systems.[1,2] Given the emerging global warming crisis, supercapacitors, in conjunction with batteries and fuel cells, can provide environmentally friendly alternative energy/power sources when compared to traditional sources such as combustion engines and gas turbines.[1]

There are two types of electrochemical capacitors: electrical double layer capacitors (EDLCs) and faradaic (or redox) pseudocapacitors. EDLCs store energy at the electrode-electrolyte interface via the separation of charge across the electrical double-layer, i.e. the charge storage is electrostatic, not faradaic. The most common materials used in EDLCs are porous, high surface area carbons. These include activated carbons, glassy carbons, carbon blacks, carbon cloth, nanotubes, aerogels, fibres and microbeads.[1-5] These carbonaceous materials have specific surface areas which range from less than 10 $m^2\ g^{-1}$ for graphitic carbon to greater than 2500 $m^2\ g^{-1}$ for certain carbon cloths and aerogels.[6] The carbon materials also exhibit high surface area to volume ratios, as well as variable amounts of micro-porosity and/or meso-porosity which make them ideal for use in EDLCs.[6-8] As such, they have been studied extensively, as well as having been incorporated into many present and upcoming commercial products.[3,6]

These carbonaceous materials are all capacitive to different degrees, with some carbons yielding very impressive specific capacitance values in the literature. For instance, heat-treated composites of SWNTs containing polyvinylidene chloride (PVDC) as a binder yielded an impressive specific capacitance of 180 F g^{-1} in potassium hydroxide.[9] Specific capacitances up to 250 F g^{-1} have been achieved from high surface area carbon blacks (>1500 m^2 g^{-1}) mixed with binders to produced supercapacitor electrodes.[10] These values indicate why, in addition to high surface area and porosity, different forms of carbon have been chosen as the electronic supports onto which pseudocapacitive electroactive materials, mainly metal oxides, are deposited in efforts to synthesize highly capacitive composites.

The second type of supercapacitor is the faradaic pseudocapacitor, which stores charge via the reversible faradaic reaction of an appropriate redox-active material. These materials are typically of two types: conducting polymers, such as polypyrrole[11] and polyaniline,[12] and transition metal oxides, including MnO_2,[13-16] NiO_x[17-19] and perhaps most important, RuO_2 (or rather, $RuO_2 \cdot xH_2O$).[4,20-23] Amorphous hydrous ruthenium oxide has the greatest specific capacitance amongst these, and is in fact the most capacitive material yet discovered.[4] Its crystalline form has lower values of capacitance compared to the amorphous material. A maximum specific capacitance of ca. 350 F g^{-1} at 100 mV s^{-1} was reported for crystalline ruthenium oxide.[24] Conversely, Jow *et al.*[4] reported a specific capacitance of 720 F g^{-1} at 2 mV s^{-1} for amorphous $RuO_2 \cdot xH_2O$ prepared by a sol-gel method and annealed at 150°C. This notable achievement in pseudocapacitor material development has largely resulted in extensive research aimed at

maximizing the capacitance of $RuO_2 \cdot xH_2O$ while minimizing the total loading of material so as to lower costs. Furthermore. it has been reported by Hu *et al.*[25] that only a few tens of mass % of the oxide is necessary to produce composites with exceptionally high specific capacitances. This has been primarily achieved by depositing and/or generating $RuO_2 \cdot xH_2O$ on high surface area carbonaceous materials in an effort to distribute the redox-active material in a uniform fashion over the greatest area possible.

A number of the previously examined carbonaceous materials as well as different methods for RuO_2 synthesis and deposition have been employed. A specific capacitance of 308 F g^{-1} at 2 mV s^{-1} was reported by Sato *et al.*[26] for a 7 wt % ruthenium oxide-loaded activated carbon composite. Popov *et al.*[27] reported a specific capacitance of 407 F g^{-1} at 1 mV s^{-1} for composites of RuO_2 deposited on carbon black (Vulcan XC72) via a colloidal method, with 860 F g^{-1} as the capacitance of the RuO_2 itself. MWNTs impregnated with 13 wt % RuO_2 reported by Park et al.[28] yielded a specific capacitance of 120 F g^{-1} at 20 mV s^{-1}, while that of the RuO_2 was ca. 800 F g^{-1}. Finally, Naoi et al.[29] used a novel incipient wetness method to fabricate composites of $RuO_2 \cdot xH_2O$ on carbon black (Ketjen Black). These composites (46 wt % Ru) exhibited a specific capacitance of 647 F g^{-1} at 2 mV s^{-1}, while the $RuO_2 \cdot xH_2O$ itself yielded an impressive 988 F g^{-1}. These composite materials are similar to those reported in this chapter and provide a basis of comparison with results reported herein.

This chapter reports the fabrication, characterization and capacitance measurements of composites of Ru/RuO_x prepared using two different types of carbon black as the carbonaceous support.

4.2 Experimental

4.2.1 Chemicals and Materials

$RuCl_3 \bullet xH_2O$ (Precious Metals Online, Ltd.) which was 43% Ru by mass was used as the ruthenium precursor. Both Vulcan XC72 (henceforth referred to as Vulcan), specific area of 250 $m^2\ g^{-1}$ and Black Pearls 2000 (henceforth referred to as Black Pearls or simply BP), specific area of 1500 $m^2\ g^{-1}$, were used individually as the high surface area carbon supports. $NaBH_4$ was used as the ruthenium reducing agent.

4.2.2 Carbon-Supported Ruthenium Oxide Composites

The carbon-supported ruthenium oxide composites were prepared as outlined in Section 2.6.2. The composites were prepared by using 10, 30, 50, 70 and 90 mass % of the $RuCl_3 \bullet xH_2O$ precursor to carbon.

Different approaches were used in order to convert the ruthenium metal to ruthenium oxide (RuO_x). Once the CMEs were prepared, the oxide was initially generated by sweeping the potential from -0.3 V to +1.4 V at 100 mV s^{-1} in 0.5 M H_2SO_4. This method proved ineffective (see Section 4.3.2) and was therefore abandoned. It was found that simply aging the CMEs in air yielded samples which produced the most consistent capacitance values. As such, aging was used to generate RuO_2 in all composites prior to characterization. The Vulcan carbon-based composites were aged for 20 weeks, while the Black Pearls based composites were aged for 8 weeks. To determine the actual ratios of C to RuO_x and any remaining Ru^0 in the composites (henceforth

denoted Ru/RuO_x), samples were sent to Canadian Microanalytical Services, Ltd. for elemental analysis. These results are discussed in Section 4.3.1.

4.2.3 Chemically Modified Electrode Preparation

CMEs were prepared as outlined in Section 2.6.3. In initial experiments, the central regions of the strips were impregnated with a hexane/paraffin wax solution to stop the corrosion of the potentiostat's leads. The presence of the wax prevented the capillary action of acidic electrolyte through the CFP electrode to the point of contact with the leads. This method was discontinued after switching to gold leads with titanium plates at the point of contact with the CFP to eliminate corrosion issues.

4.2.4 Electrochemical Measurements

Cyclic voltammetry was use to measure the capacitance of the CMEs and hence the composites themselves. The current was measured either from -0.2 V and/or 0 V to +0.8 V and/or +1.0 V depending on the magnitude of the contribution to the current from water reduction and/or oxidation. This ensured that all capacitances were measured over a 1.0 V range, allowing for proper comparison of results. Once the CMEs were prepared, CV was performed on at least 3 different electrodes of similar mass loading of the same composite. When testing multiple CMEs consisting of the sample composite material, the electrodes were switched on the fly using the same electrolyte with 15 minutes of degassing between samples. When CMEs of different composites were tested, fresh

electrolyte solution was always used. For information on electrochemical setup, methods and instrumentation, see Section 2.2.

Capacitance was calculated according to Equation 2.1 for each CME. To calculate the specific capacitance, the calculated capacitance values were divided by the total mass loading of composite on the electrode as measured by an analytical balance; the mass was recorded to five decimal places (0.00001 g). The specific capacitance values for both the anodic and cathodic currents were then averaged over a 1.0 V range, resulting in two average specific capacitance values. The absolute average of these two values was then calculated to yield the final value of the specific capacitance of the CME and thus, the composite itself.

4.2.5 Characterization of Composites

The composites were characterized by XPS, XRD, and TEM as outlined in Sections 2.3, 2.4, and 2.5, respectively. For TEM, all images were initially produced as negatives and then scanned using a conventional scanner to create digital images.

4.3 Results and Discussion

4.3.1 Elemental Analysis

The composites were prepared by combining the ruthenium precursor and carbon support material in known mass ratios. Once combined with the carbon and $NaBH_4$, the $RuCl_3$ is reduced to Ru^0. Assuming a complete conversion of $RuCl_3 \cdot xH_2O$ to Ru^0 and that all the Ru^0 was deposited on the carbon, this changes the starting mass % $RuCl_3 \cdot xH_2O$ to

a theoretical mass % Ru^0 on the carbon support. Table 4.1 shows the initial mass % of $RuCl_3 \cdot xH_2O$ and carbon as well as the theoretical mass % of the deposited Ru^0. This forms the basis for reporting the composites as theoretical mass % Ru on both carbon supports. However, in order to discern the actual percentage of the Ru/RuO_x on carbon, elemental analysis was performed on the aged samples. Using this method, a Ru analysis was attempted, but a suitable solvent could not be found to dissolve the metal, so only C, H, and N were analyzed. However, by subtracting out their contribution, the percentage of Ru was determined. The results of the analysis for the Vulcan composites are shown in Table 4.2. The analysis of unmodified Black Pearls powder indicated an impurity (likely oxygen) which was 6.57% by mass. As the elemental analysis could only analyze the carbon in the composite as opposed to the total elemental contribution from Black Pearls, the mass % of carbon was adjusted to account for the impurity in each composite sample. This was done by scaling up the mass % carbon in each composite by dividing it by the 93.43 mass % carbon in the 100% Black Pearls sample. The results of the elemental analysis for the Black Pearls composites, including original as well as adjusted values

Table 4.1. Mass percentages of Ru before and after reductive deposition on carbon.

mass % Carbon	Initial mass % $RuCl_3 \cdot xH_2O$	Theoretical mass % Ru^0
90	10	4.6
70	30	15.6
50	50	30.1
30	70	50.1
10	90	79.5

Table 4.2. Theoretical and Analytical Mass % Ru, RuO_2 and Ru/RuO_x on Vulcan Carbon Supports.

Theoretical mass % Ru	Theoretical mass % RuO_2	mass % C	mass % H	mass % N	Analytical mass % Ru/RuO_x
4.6	5.92	90.39	<0.3	<0.3	9.61
15.6	19.53	76.50	<0.3	<0.3	23.50
30.1	36.15	70.06	<0.3	<0.3	29.94
50.1	56.92	46.58	<0.3	<0.3	53.42
79.5	83.60	18.88	<0.3	<0.3	81.12

Table 4.3. Theoretical and Analytical mass % Ru/RuO_x on BP Carbon Supports.

Theoretical mass % Ru	Theoretical mass % RuO_2	mass % H	mass % N	mass % C		Analytical mass % Ru/RuO_x	
				Original	*Adjusted*	*Original*	*Adjusted*
4.6	5.92	1.19	<0.3	79.80	85.41	19.01	13.40
15.6	19.53	<0.3	<0.3	69.41	74.30	30.59	25.71
30.1	36.15	<0.3	<0.3	57.09	61.10	42.91	38.90
50.1	56.92	<0.3	<0.3	40.49	43.34	59.51	56.66
100% BP		<0.3	<0.3	93.43		-	

* insufficient amounts of 79.5 mass % for elemental analysis due to difficulties producing composite

(calculated from the scale up) of the mass % carbon and Ru/RuO_x are shown in Table 4.3. analysis for the Black Pearls composites, including original as well as adjusted values (calculated from the scale up) of the mass % carbon and Ru/RuO_x are shown in Table 4.3.

`The most plausible explanation for this is due to the lower theoretical mass % Ru and RuO_x for these samples. With lower Ru^0 loadings, the metal nanoparticles are most

likely spread over the high surface area of the carbon as opposed to existing as large clusters. Accordingly, more of the Ru metal is exposed to the air to promote oxidation, resulting in a more thorough conversion of Ru^0 to RuO_2. The increased amount of oxide is accompanied by an increased probability of hydration during oxide formation, meaning the RuO_2 within the composites likely exists as $RuO_2 \cdot xH_2O$. The hydrate mass would increase the mass contribution of the RuO_2 in the composite, increasing the mass % to values greater than the theoretical, anhydrous RuO_2 mass percent. It is also likely that a small fraction of the Ru^0 was converted to other RuO_x species such as RuO_3 and RuO_4, the greater masses of which would increase the analytical mass % Ru/RuO_x. Finally, it is possible that the composite also contained impurities from the precursor materials, most likely chloride ions, which artificially increased the apparent mass % Ru/RuO_x in the composites beyond those of the theoretical percentages.

Conversely, the 29.94 mass % Ru/RuO_x on Vulcan composite was lower than its theoretical mass % Ru. This was possibly due to incomplete reduction of $RuCl_3 \cdot xH_2O$ during composite synthesis, which would have decreased the amount of Ru^0 in the composite. Also, it is possible that the newly formed Ru^0 may not have been completely deposited on the carbon.

It should be noted that these results are most important when calculating the specific capacitance of the electroactive Ru/RuO_x material in the composites, which is discussed in Section 4.3.2. All results reported herein are expressed in terms of the analytical mass % Ru/RuO_x as discussed above unless otherwise stated. In certain cases,

Vulcan and Black Pearls composites of the same theoretical mass % Ru are compared to ensure that the comparisons between similarly prepared composites are not biased.

4.3.2 X-ray Photoelectron Spectroscopy Characterization

X-ray photoelectron spectroscopy was used to determine the oxidation states of the various RuO_x species (with RuO_2 expected to be dominant) as well as to qualitatively elucidate the extent to which oxidation of the deposited Ru^0 occurred. Prior to performing XPS on composites samples, several carbon black samples were tested. This was necessary as the binding energies of carbon and ruthenium are in the same range; carbon peaks are typically found in the range of 284 to 285 eV, while the various oxides of ruthenium have binding energies in the range of 281 to 284 eV. Thus having blank carbon black spectra provided a reference for discerning between ruthenium oxides and carbon in the likely event of overlapping peaks. Figure 4.1 shows the XPS spectrum of a Black Pearls sample. The significant shoulder peak located at 285.8 eV is due to carbon-oxygen bonds found in the carbon; the high intensity of this peak is most likely due to the large number of functional groups containing carbon and oxygen in the high surface area Black Pearls. For the majority of XPS samples that contain carbon, the primary carbon peak is typically found at ca. 285.0 eV. For the Black Pearls and Vulcan samples, this was found not to be the case, as the primary C 1s peak was located at ca. 284.0 eV. It is the confirmation of the C 1s peak at 284.0 eV which provided the most assistance in discerning between carbon and oxides of ruthenium during analysis of the composite spectra. Figure 4.2 shows the XPS spectra for a 30 mass % Ru/RuO_x on Vulcan (aged 23

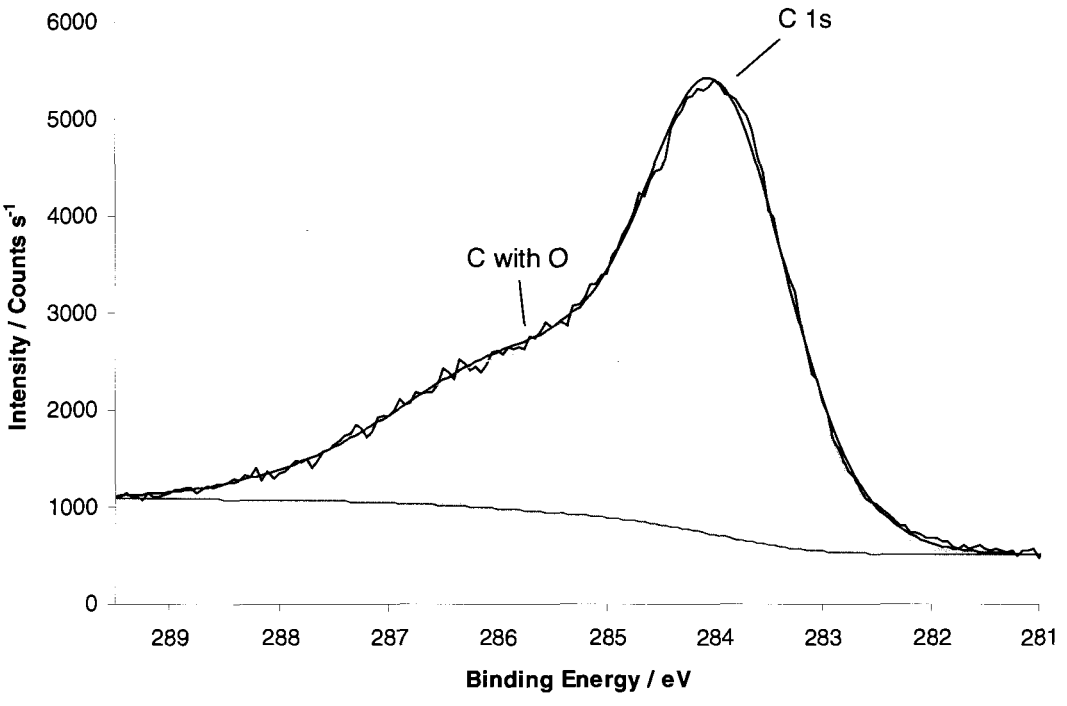

Figure 4.1. High resolution XPS spectrum of a Black Pearls 2000 sample.

weeks) and a 38.9 mass % Ru/RuO_x on Black Pearls (aged 10 weeks) composite. The C with O and C 1s peaks were again found at 285.8 eV and 284.0 eV as per the Black Pearls sample. In the range of the ruthenium oxides binding energies, a peak was found at 281.2 eV and 281 eV for the Vulcan and Black Pearls samples, respectively. These peaks were in the range of the binding energy of RuO_2. As no other significant peaks for RuO_x species were found in these samples, this result confirmed that RuO_2 was the dominate form of the oxide in the composites, as expected. All other composites analyzed by XPS confirmed this result.

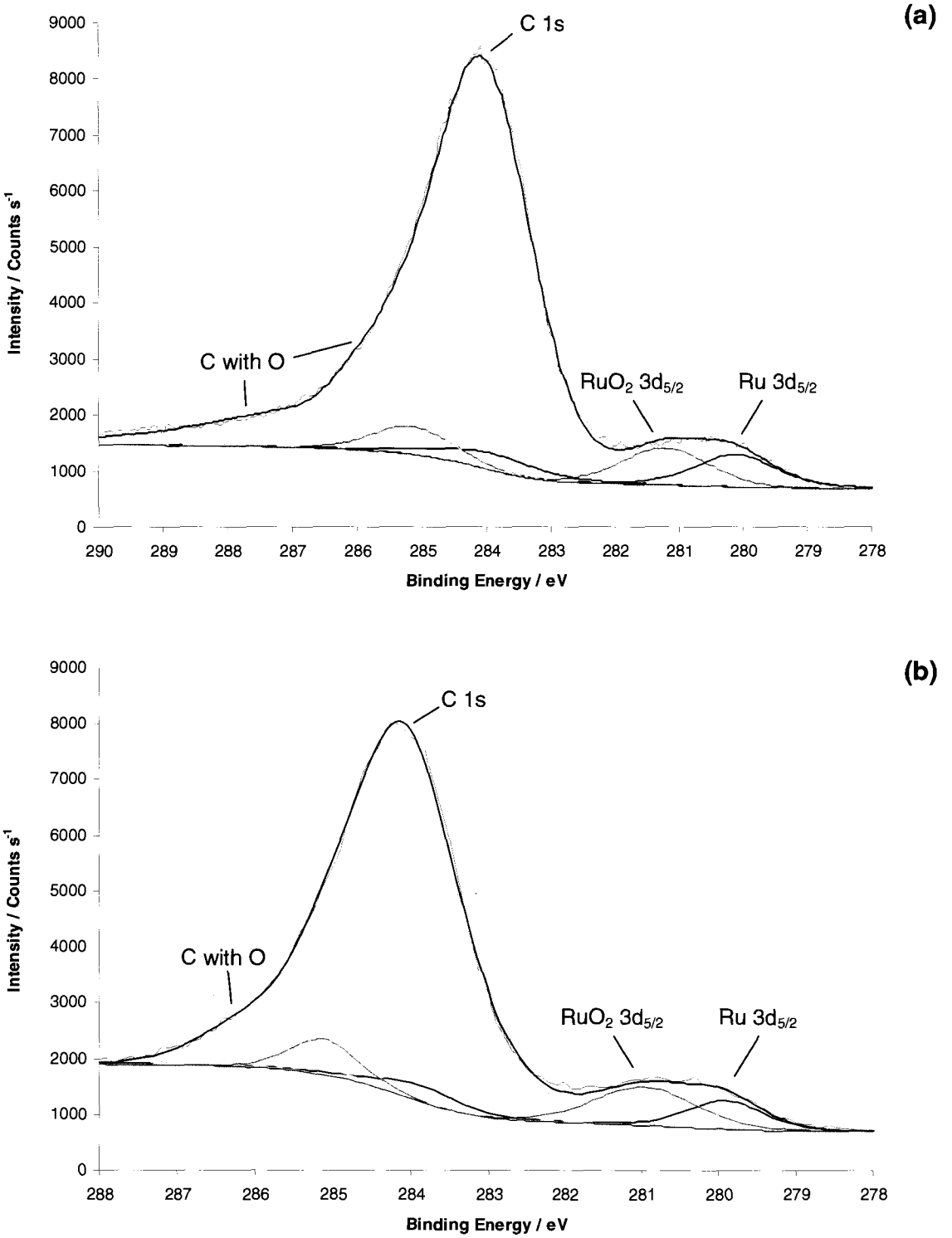

Figure 4.2. High resolution XPS spectra of composites containing (a) 29.94 mass % Ru/RuO_x on Vulcan and (b) 38.9 mass % Ru/RuO_x on Black Pearls.

capacitive character due to the inability of protons to penetrate the crystalline lattice and hence take part in the reaction with the electroactive RuO_2.[25,30] As such it is desirable to produce amorphous hydrous RuO_2 in the composites. Since annealing the sample increases its crystallinity with increasing temperature,[4] the aging in air method was more suitable for the formation of amorphous RuO_2. During XRD, such a material would not yield a diffraction pattern as it would not be crystalline. Thus, XRD was used to verify the assumption that the RuO_2 was amorphous and not crystalline. However, any remnant Ru^0 that was not oxidized would be expected to produce its own diffraction pattern. Finally, as all the composites contain carbon, the C (002) phase of both types of carbon black was expected in the composite diffraction patterns.

Figure 4.3 is shown to illustrate the various planes of Ru^0 found in the composites via the XRD pattern for a 29.94 mass % Ru on Vulcan carbon composite. The diffraction peak at ca. 25.0° is due to reflection of the C (002) plane as referred to previously. The large peaks at ca. 38.5° and 43.8°, as well as the shoulder peak at ca. 42.0° are due to the Ru (100), Ru (101) and Ru (002) planes of Ru^0, respectively. Meanwhile, the series of peaks at ca. 58.0°, 69.0°, 78.0°, 84.5° and 85.5° represent the reflections of the Ru (102), Ru (110), Ru (103), Ru (112) and Ru (201) planes, respectively. There were no peaks due to any reflection planes of RuO_2 in the diffraction pattern.

This result was typical of all the XRD patterns obtained for the composites, with varying degrees of peak intensity. Figure 4.4 shows the diffraction patterns of all the Vulcan carbon-based composites prior to extensive aging. The intensity of all the Ru^0 peaks increased with increasing amounts of Ru^0. Unsurprisingly the 9.6 mass % Ru/RuO_x

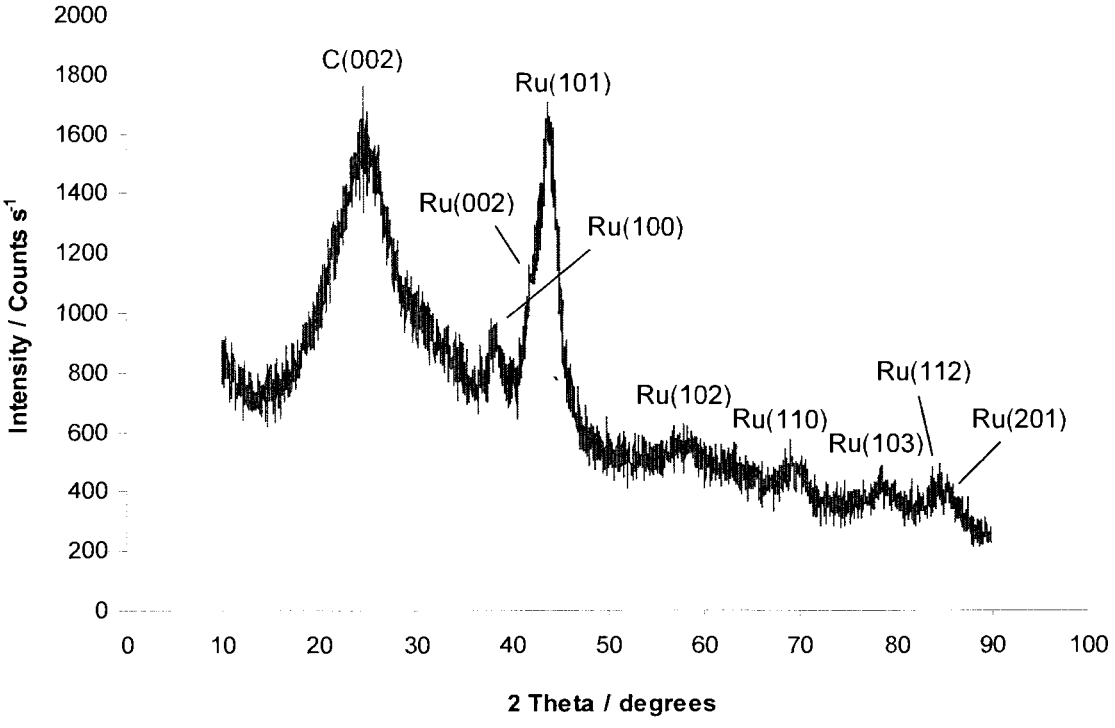

Figure 4.3. XRD pattern of a 29.9 mass % Ru/RuO_x on Vulcan composite.

composite yielded the least intense Ru^0 peaks, while both the 53.4 mass % and 81.1 mass % Ru/RuO_x composites yielded Ru^0 peaks of comparable intensity. This result confirmed that when the composites were first formed, they were composed of varying amounts of Ru^0, as would be expected. As in Figure 4.3, the composite XRD patterns contained no peaks due to any phases of RuO_2. The absence of any peaks from the diffraction pattern of RuO_2 indicated that any initial Ru^0 converted to the oxide had to have been amorphous.

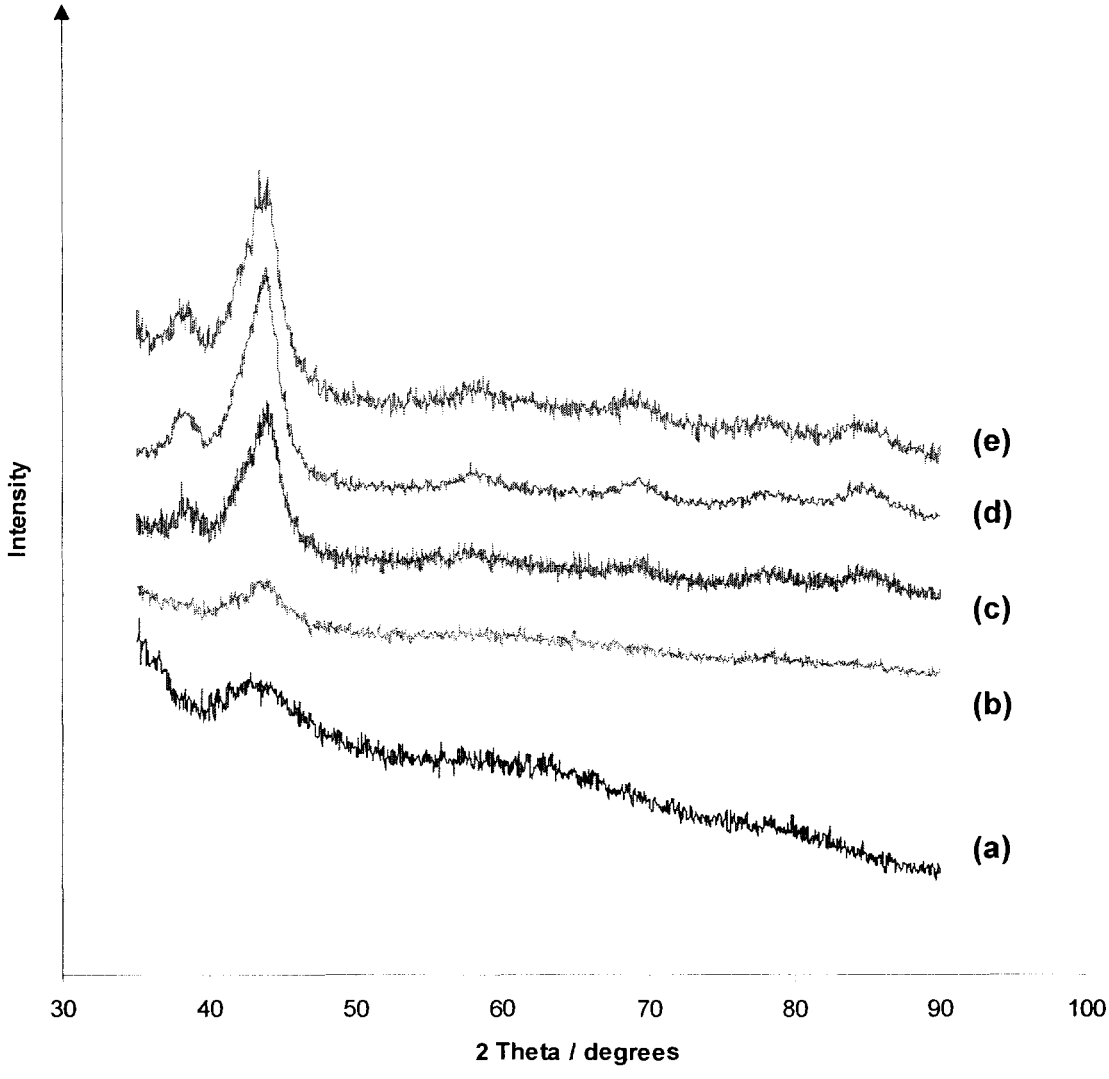

Figure 4.4. XRD patterns for Vulcan-based composites containing (a) 9.6 %, (b) 23.5 % (c) 29.9 % (d) 53.4 % and (e) 81.1 % Ru/RuO_x by mass.

Once the samples were aged further the XRD patterns were measured and compared with the initial patterns. Figure 4.5 shows the diffraction pattern of Figure 4.3 and that of the same sample after the aging process. The differences between the two diffraction patterns are indicative of a number of key characteristics of the composites. First, the intensity of the Ru (101) peak at ca. 43.8° decreased to about a quarter that of the composite after 20 weeks of aging. The Ru (100) peak at 38.5° and Ru (002) peak at 42.0° almost disappeared completely. Finally, the peaks at ca. 58.0°, 69.0°, 78.0°, 84.5°

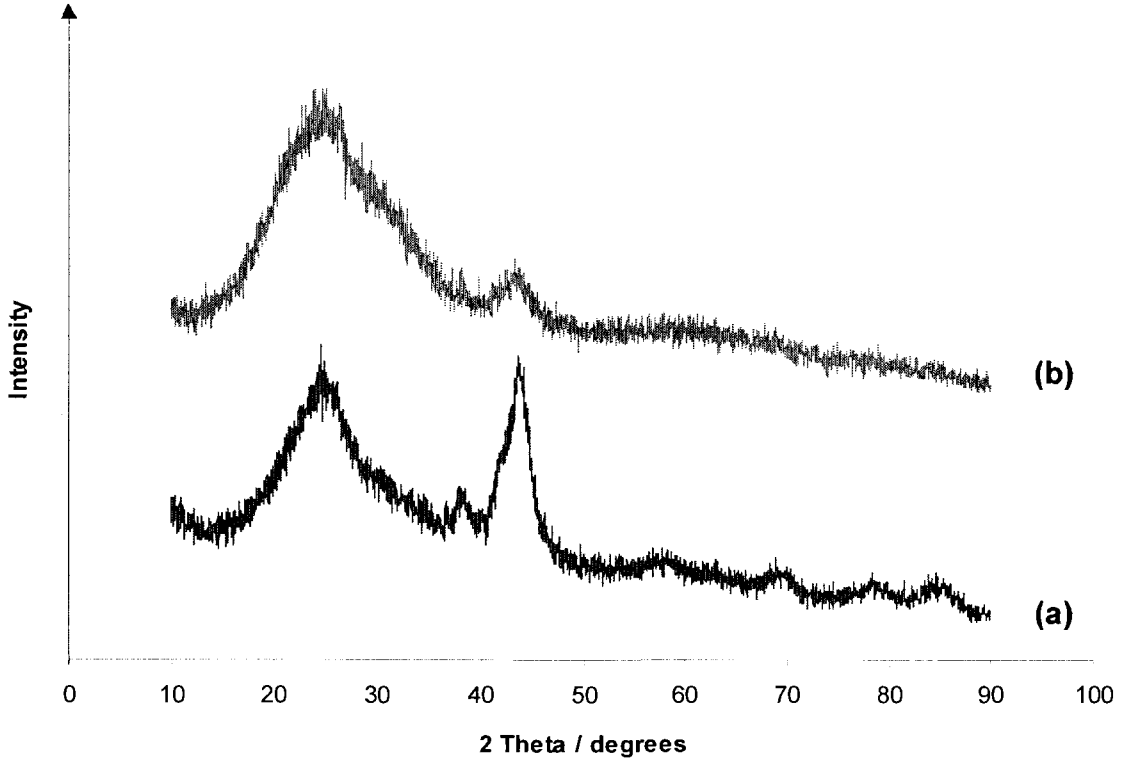

Figure 4.5. XRD patterns of a 29.9 mass % Ru/RuO_x on Vulcan composite after aging for (a) 1 week and (b) 20 weeks.

and 85.5° were no longer present in the diffraction pattern. These findings indicate that with aging, the Ru^0 was being consumed as it was converted to RuO_2. In addition, the lack of any crystalline RuO_2 pattern indicated that the Ru^0 was converted to amorphous RuO_2 with aging. This was an encouraging result which further supported the method of aging the composites to produce the oxide.

The remaining unconverted Ru^0 in the composites required further study. It was necessary to determine the average size of the Ru^0 nanoparticles in the samples in order to gain a better understanding of how they were distributed on the carbon support. As such, the mean particle diameter of the Ru^0 nanoparticles was estimated using the Ru (101) peak width according to the Scherrer equation:[31]

$$d = \frac{0.9\lambda}{B\cos\theta_B} \qquad \text{(Equation 4.1)}$$

where d is the mean particle diameter in nanometers, λ is the x-ray wavelength in nanometers, B is the full width of the peak at half the maximum value (FWHM) in radians, and θ is the diffraction angle in radians. For the 30 mass % Ru/RuO_x on Vulcan composite, the mean particle diameter was 4.3 nm after one week of aging. After 20 weeks of aging, the mean particle diameter had shrunk to 3.1 nm. A mean particle diameter of 3.1 nm was also found for the 42.9 mass % Ru/RuO_x on BP composite after 8 weeks of aging. Table 4.4 shows the mean particle diameters for the remaining Vulcan composites after four weeks of aging. As seen, the particles size increased slightly with the increasing mass % Ru/RuO_x in the composite. This supports the more thorough

Table 4.4. Mean particle diameters of Ru^0 in Vulcan-based composites.

Analytical mass % Ru/RuO_x on Vulcan	Mean Particle Diameter (nm)
9.61	3.0
23.50	3.1
29.94	3.1
53.42	3.2
81.12	3.8

conversion of Ru^0 to RuO_2 at lower Ru/RuO_x mass loadings as described earlier. Particle sizes for the remaining Black Pearls composites were not measured due to time restraints.

These results suggest that the Ru^0 nanoparticle diameters shrink with aging, as they were slowly converted to amorphous RuO_2. This led to the speculation that the composites consisted of crystalline Ru^0 metal "cores" surrounded by an amorphous RuO_2 "shell". This is illustrated in Figure 4.6. The existence of such core-shell structures would suggest that there is a limit to the amount of deposited Ru^0 that can be converted to RuO_2 via aging in air. If the amorphous RuO_2 shell surrounded the Ru^0 core, it would essentially cut off access of oxygen in the atmosphere to the Ru metal, which would hinder the formation of the oxide prematurely. This would yield composites with less than the maximum effective loading of RuO_2, which would translate into lower capacitance values. Consequently, it was necessary to confirm the validity of this theory.

While it was partially supported by XRD, the particle sizes of the entire core-shell structure were required. Essentially, this meant determining the mean particle diameter of RuO_2 particles in the composites, which was accomplished using TEM.

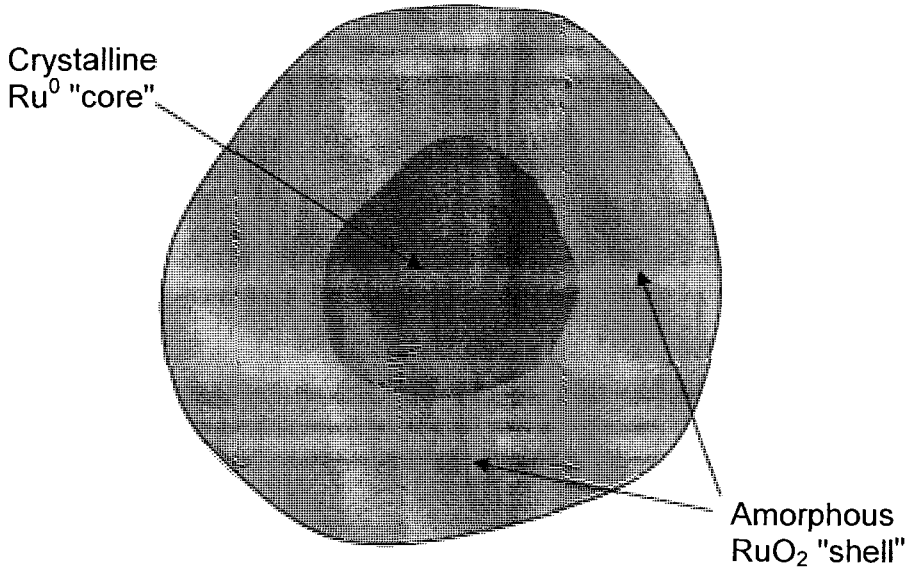

Figure 4.6. Diagram of the proposed crystalline Ru^0 nanoparticle "core" encased in an amorphous RuO_2 "shell".

4.3.4 Transmission Electron Microscopy Characterization

Several composites were imaged using TEM. Initially, the micrographs were used to determine whether or not the Ru^0 and/or RuO_2 nanoparticles were uniformly distributed on the carbon support. Figure 4.7 shows TEM micrographs of a 13.4 mass % Ru/RuO_x on Black Pearls composite. This image is used to indicate which portions of the

micrographs are the carbon support, and which portions are the Ru^0 and/or RuO_2 nanoparticles. As shown, the carbon support appears almost as disc-like amorphous entities with varying degrees of transparency due to overlap. When there is little overlap, the carbon appears transparent or semi-transparent, as highlighted. When the overlap is more pronounced, the carbon becomes less transparent and shows up as darkened spots.

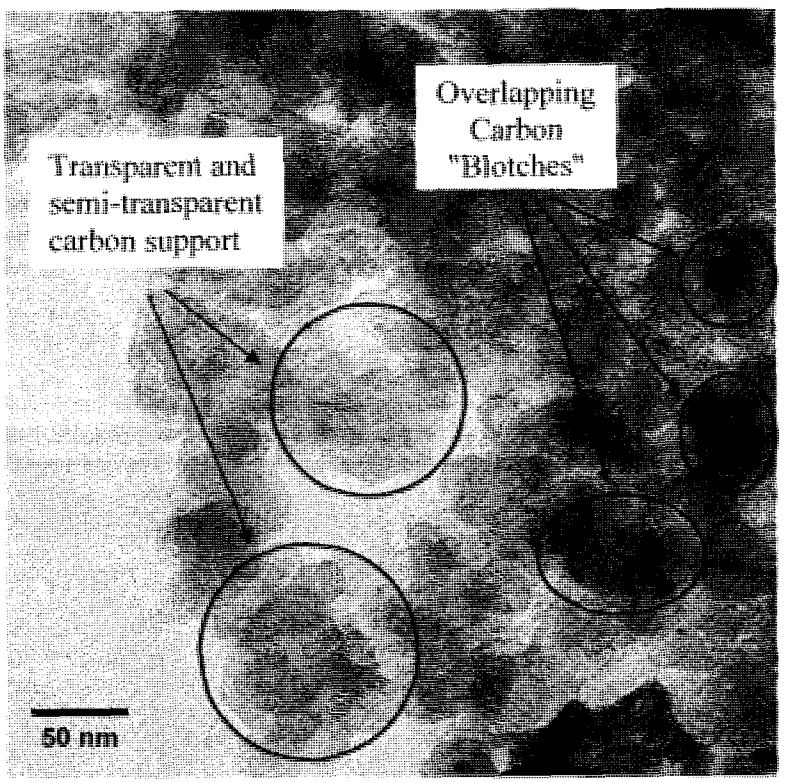

Figure 4.7. TEM micrograph of 13.4 mass % Ru/RuO_x on Black Pearls highlighting characteristics of the carbon support.

These blotches proved to be problematic as they sometimes masked the appearance of the nanoparticles of Ru^0, which appear as much smaller, darker spots on the carbon supports.

This was especially true of the Black Pearls composites. Figure 4.8 shows TEM micrographs of Black Pearls composites of 13.4 mass %, 25.7 mass % and 38.9 mass % Ru/RuO_x. The amount and distribution of the Ru^0/RuO_2 nanoparticles increases with the increases in mass % of ruthenium. In Figure 4.8a, there are few nanoparticles visible; the majority can be found in clusters on the right-half portion of the micrograph. The localization of the nanoparticles also indicates the lack of a uniform distribution throughout the composite. This is expected as there was very little ruthenium available for deposition initially. When the amount of $RuCl_3$ was increased to yield a theoretical 15.6 mass % Ru, the quantity of visible nanoparticles increased significantly, as did the distribution on the carbon support; this is seen in Figure 4.8b The distribution was still not uniform however, although it was a notable improvement over the previous composite. When moving to the 38.9 mass % Ru composite, the quantity of visible nanoparticles increased as expected, with the distribution on the carbon support becoming even more uniform. Figure 4.8c also shows several regions of overlap where discerning between carbon and ruthenium nanoparticles becomes difficult. For the most part, unfortunately, it was only possible to determine by eye which particles were Ru^0/RuO_2 and which were carbon for the BP composites. This distinction was necessary in order to analyze the size of the particles for comparison with the XRD results in order to confirm the proposed "core-shell" theory.

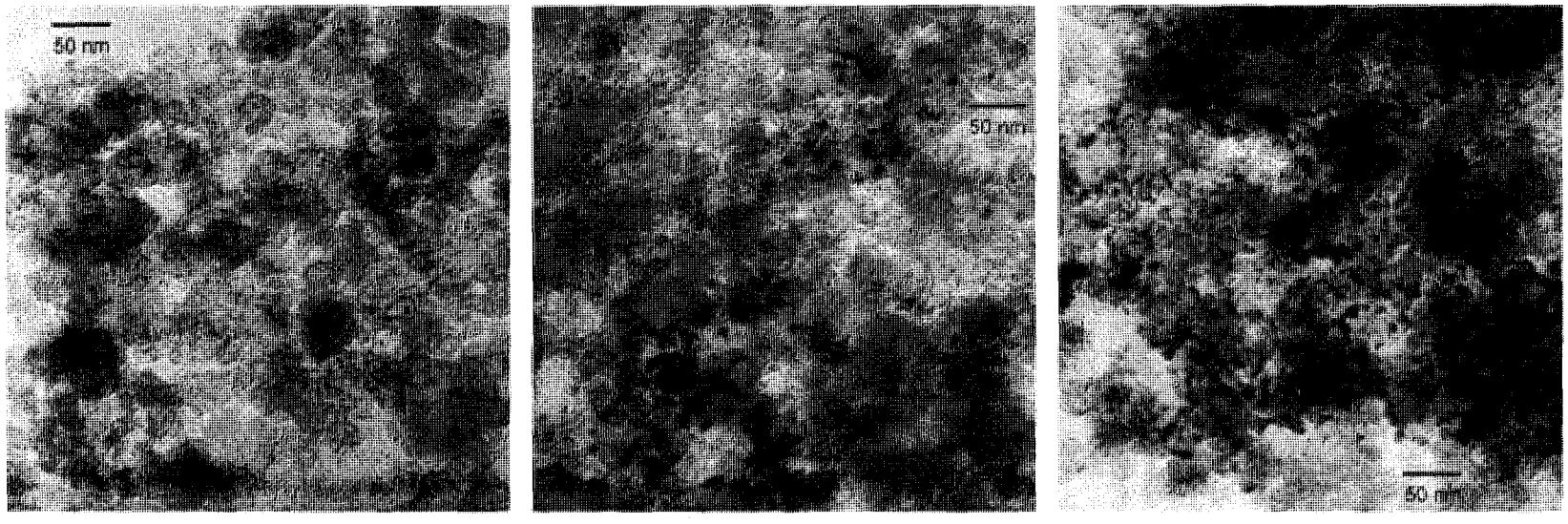

Figure 4.8. TEM micrographs of Black Pearls based composites composed of (a) 13.4 mass % Ru/RuO_x, (b) 25.7 mass % Ru/RuO_x and (c) 38.9 mass % Ru/RuO_x.

Once the XRD analysis of the composites led to the proposed core-shell theory, the micrographs were analyzed using ImageJ, an open source image processing and analysis program. The process involved taking the raw TEM micrograph, then subtracting out any background objects that would bias the analysis. In this case, the background consisted of the carbon support, as well as any anomalous shapes or objects that were not part of the composite. Next, the background subtracted image was analyzed according to user-defined parameters. In this case, default settings were mostly used, with the exception of the exclusion of objects with areas greater than 1000 nm^2. This area limitation was used because some Ru^0/RuO_2 nanoparticles were in regions of carbon overlap, resulting in large, darkened spots that would be mistaken for individual target particles during analysis. Finally, the program applied masks over all the particles in the micrograph that were analyzed. This process is shown for a 29.9 mass % Ru/RuO_x on Vulcan carbon composite TEM micrograph in Figure 4.9. It should be noted that only Vulcan-based composites were analyzed in this manner. The abundance and density of carbon overlap in the Black Pearls composites made background subtraction ineffective, resulting in numerous Ru^0/RuO_2 false positives during particle analysis. This is attributed to the higher surface area of Black Pearls carbon.

The results of the TEM analysis gave an average particle diameter of 8.9 nm, with particle diameters ranging from 1 nm to 20 nm. This was significantly larger than the Ru^0 nanoparticle sizes of 3.1 nm found for both the Vulcan and Black Pearls composites via XRD. The difference in particle size supports the ruthenium "core-shell" theory that was postulated after XRD analysis. Further support for the existence of structures of Ru^0 cores

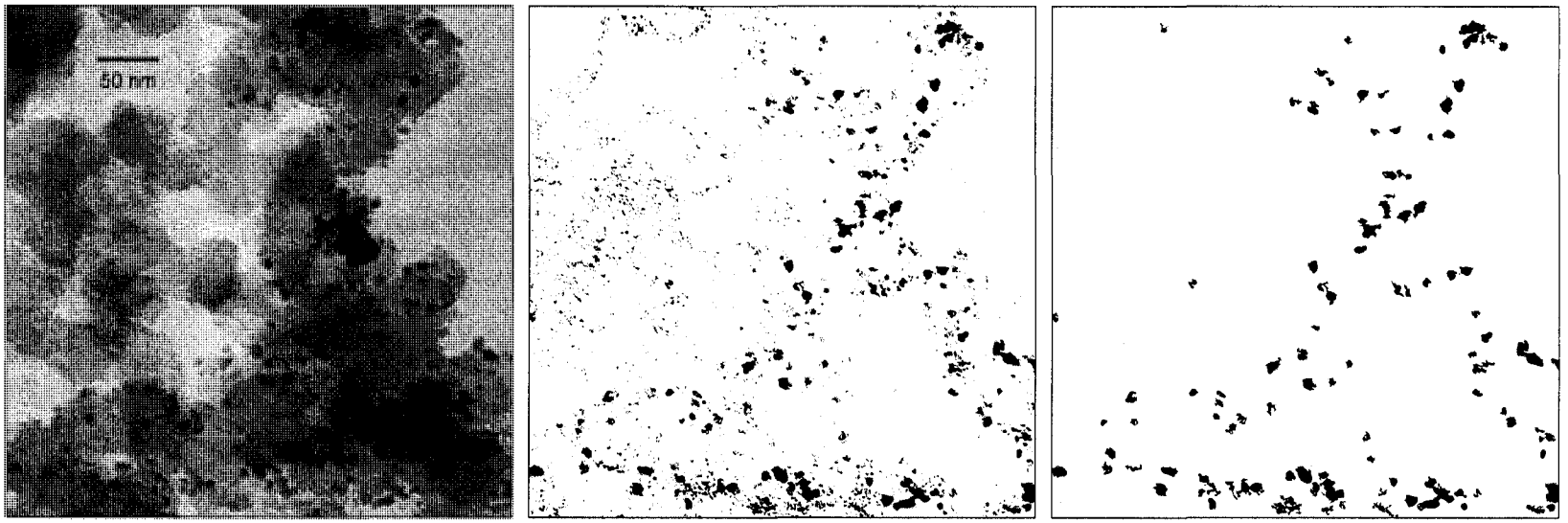

Figure 4.9. Sequential illustration of the image analysis process, showing (a) the original TEM micrograph, (b) the background subtraction and threshold correction and (c) the applied masks for particles used in the analysis.

with amorphous RuO_2 shells is shown in the TEM micrograph of Figure 4.10, which contains a mixture of nanoparticles. Larger particles in the range of ca. 10 nm to 25 nm are amorphous RuO_2 nanoparticles surrounding Ru^0 cores. Smaller nanoparticles less than ca. 5 nm are likely that of Ru^0, as they correlate to the mean particle diameters of Ru^0 particles determined by XRD. This is difficult to surmise, however, as the smaller

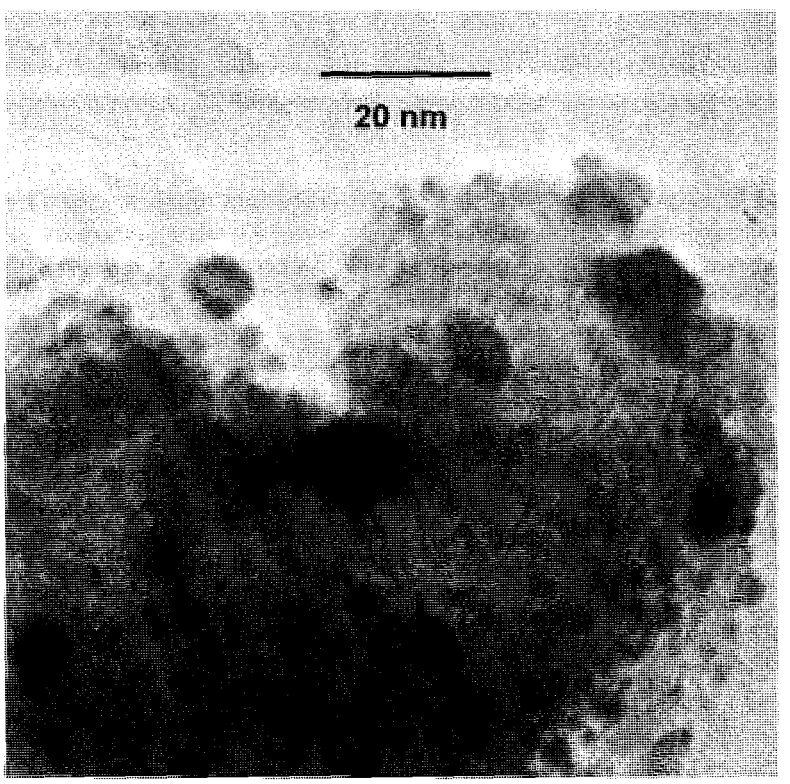

Figure 4.10. High magnification TEM of a 29.94 mass % Ru/RuO_x on Vulcan composite containing a mixture of nanoparticle sizes.

nanoparticles may be a mixture of Ru^0 particles and RuO_2 particles which themselves may have Ru^0 cores. However, this observation further supports the supposition that the Ru^0 and RuO_2 nanoparticles in the composites exist as "core-shell" structures.

4.3.5 Cyclic Voltammetry - Capacitance Measurements

Cyclic voltammetry was used in a three-electrode cell to measure the current for CMEs with different composites. A scan speed of 50 mV s^{-1} was used for initial experiments, but this was changed to 10 mV s^{-1} as literature scan speed values range anywhere from 2 to 20 mV s^{-1} for RuO_2-based supercapacitor materials.[26-29] Figure 4.11 illustrates the effect of different scan speeds on current and hence capacitance for a 29.94 mass % Ru/RuO_x on Vulcan aged for 1 week. Figure 4.11a shows that varying the scan speed results in different current responses as the potential is swept between upper and lower limits. This is because the current increases with the root of the scan speed.[32]

Thus, a higher scan speed results in higher current values at a given potential. It would appear likely then, that higher scan speeds would produce high values of capacitance, and hence specific capacitance. However, as capacitance from CV is the quotient of current and scan speed, the opposite is true experimentally, as lower scan speeds yield higher values of capacitance (and thus specific capacitance) than higher scan speeds. This is due to a number of reasons. First, at higher scan speeds the experimental time frame is reduced, which hampers the kinetics of the RuO_2 redox reactions. During reductive scans, a limited number of protons are able to reach the RuO_2 surface, resulting in proton depletion in the electrolyte within the electrode.[33] During oxidative scans, an

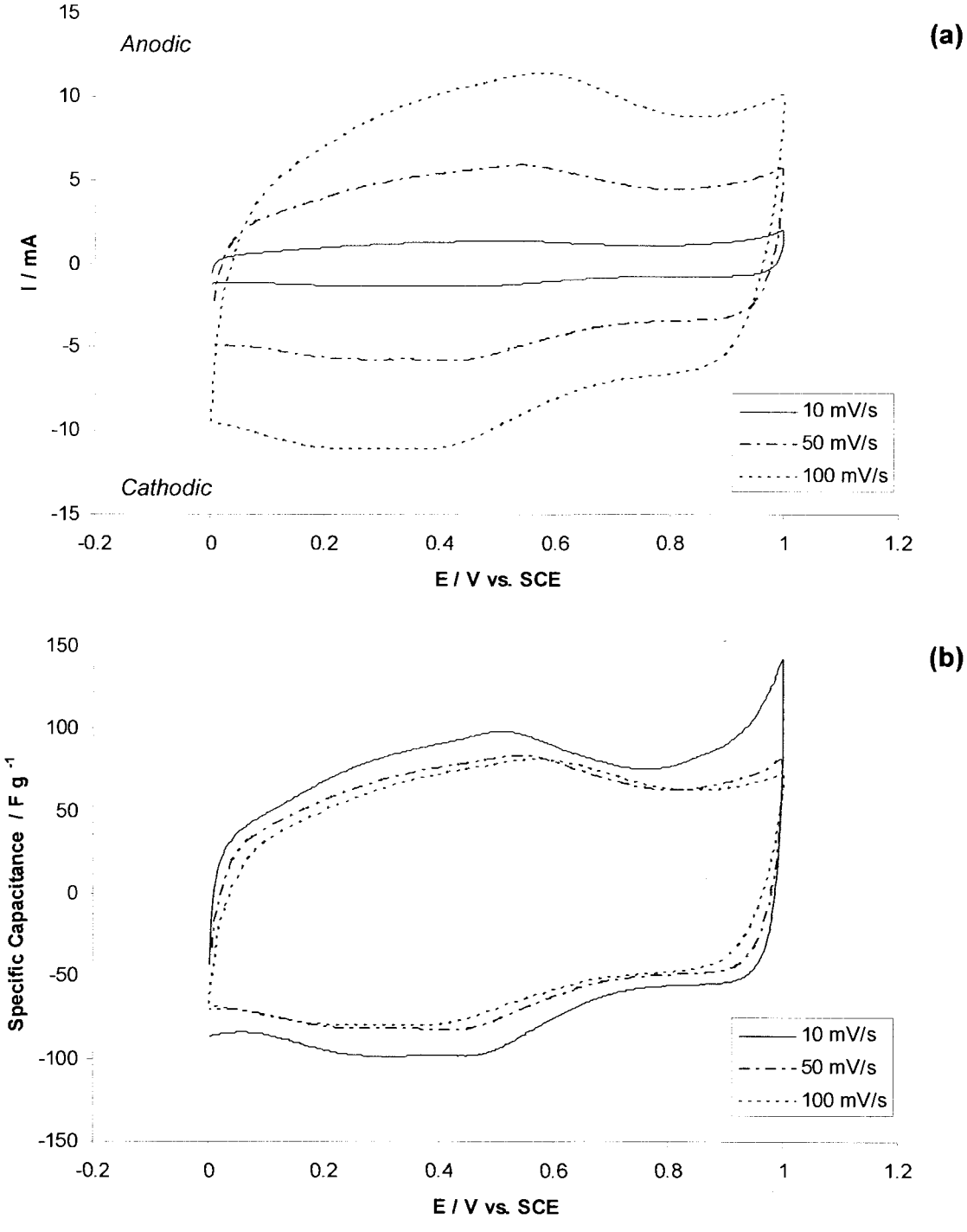

Figure 4.11. Cyclic voltammograms of 29.94 mass % Ru/RuO_x on Vulcan composite (aged for 1 week, mass loading 1.4 mg) showing (a) current and (b) specific capacitance as a function of potential at different scan speeds in 0.5 M H_2SO_4.

excess number of protons are released by the surface, resulting in proton oversaturation in the electrolyte.[33] Overall, this limits the redox capabilities of RuO_2 according to Equations 1.10 and 1.11, and therefore decreases capacitance. In addition, the proton depletion and oversaturation within the electrolyte produces a significant increase in ionic resistance, which causes a voltage drop within the electrolyte. Finally, when the scan direction is changed at high scan speeds the larger resistance increases the resistance-capacitance (RC) time constant of the electrochemical cell such that the output current cannot keep pace with the applied potential at the potential switching point.[34] These effects are illustrated in Figure 4.11b[†] in which the ten fold increase in scan speed from 10 mV s^{-1} to 100 mV s^{-1} results in a drop in specific capacitance of 20 F g^{1} at +0.5 V vs. SCE. This confirms that lower scan speeds provide higher values of specific capacitance.

Prior to making the composites, the specific capacitances of both Vulcan and Black Pearls were tested. The CVs for both forms of carbon are presented in Figure 4.12. As shown, the specific capacitance for Vulcan was 13 F g^{-1}, while that of Black Pearls was ca. 145 F g^{-1}. The specific capacitance of the Black Pearls CME was over an order of magnitude greater than that of the Vulcan; this can be attributed to its much higher surface area.[6] This also serves as the primary reason for choosing Black Pearls as a carbon support for ruthenium-based supercapacitor composites. For the most part, the CVs of both the Vulcan and Black Pearls CMEs did not exhibit any redox behaviour, and

[†] Since the sign of the current and scan speed are the same during a cycle, capacitance values are always positive. However, for any CV which plot specific capacitance on the y-axis instead of current, a negative sign is used for values in the cathodic direction in order to present the data as a standard voltammogram.

as such were mostly flat and featureless in both the anodic and cathodic directions. This is due to the fact that the vast majority of aqueous carbon supercapacitor materials attain their capacitance from charging of the electrical double-layer as opposed to pseudocapactiance.[6-8] However, a small reversible redox couple was observed at ca. +0.4 V vs. SCE for the Black Pearls samples. This is most easily observed as the cathodic peak on the reverse sweep at ca. +0.32 V vs. SCE in Figure 4.12. This was later found to be the redox couple of hydroquinone/quinone carbonyl groups; these groups have been

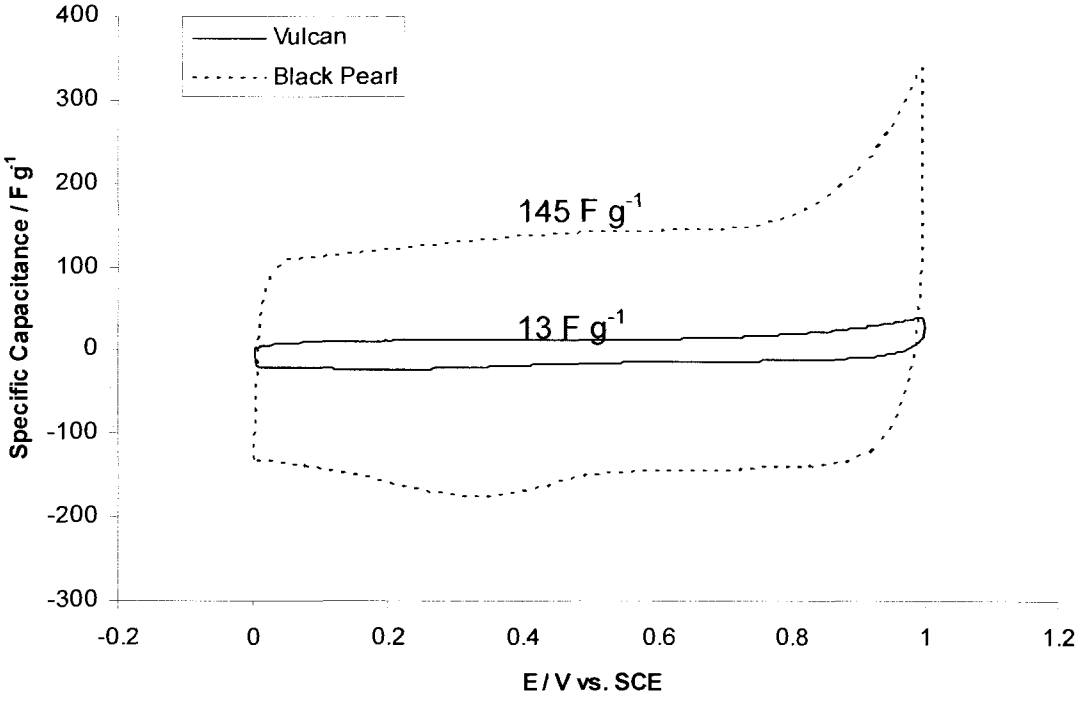

Figure 4.12. Comparison of cyclic voltammograms, expressed as specific capacitance against potential, for "blank" Vulcan and Black Pearls CMEs with mass loadings of 0.90 mg and 0.80 mg, respectively.

found to be responsible for a considerable percentage of the capacitance in certain EDLCs.[35-37] The presence of such a defined redox couple for hydroquinone/quinone is likely due to the greater surface area of the Black Pearls which corresponds to a significantly increased number of functional groups, including carbonyls and carboxylic acid groups.

As stated previously, different methods were used to convert Ru metal to RuO_2. The first technique used was to sweep the potential between upper and lower limits at either 50 or 100 mV s^{-1} to generate the oxide.[38,39] Figure 4.13 shows he initial and final

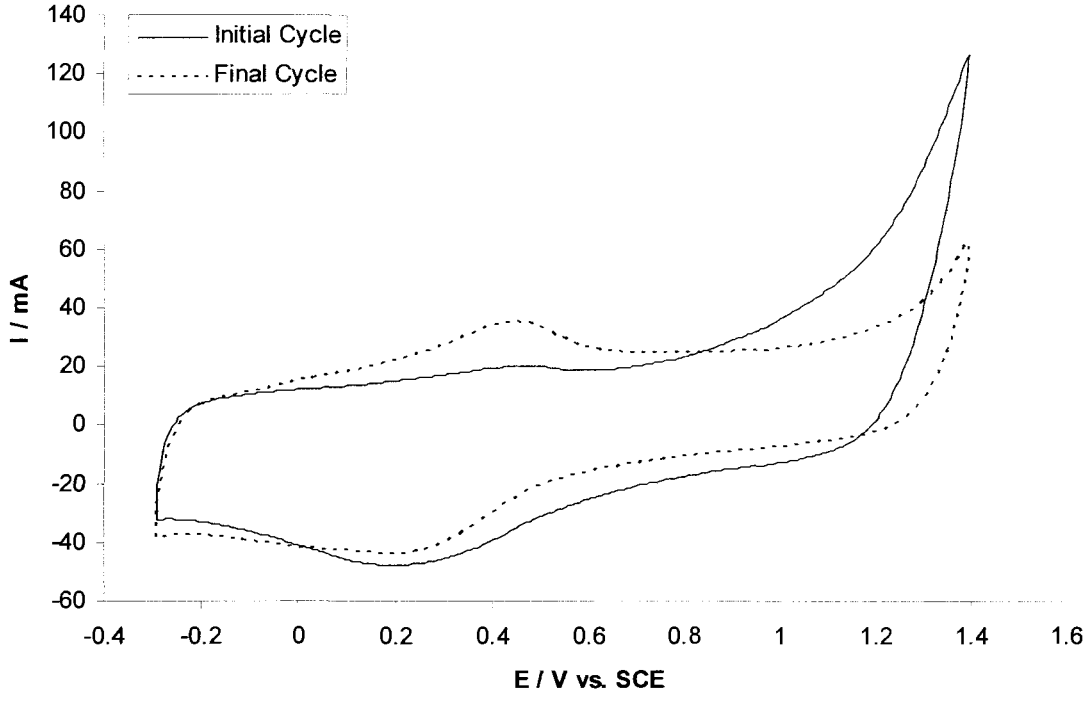

Figure 4.13. Initial and final cyclic voltammograms after 50 cycles at 100 mV s^{-1} to convert Ru^0 to RuO_2 for 0.92 mg of a theoretical 4.6 mass % Ru on BP composite.

voltammograms for a theoretical 4.6 mass % Ru on Vulcan composite. Over the course of cycling, a redox couple emerged at ca. +0.35 V vs. SCE. This was initially thought to be due to the ongoing production of RuO_2 during cycling. However, the RuO_2 redox couple (for samples which have not been annealed) is typically found around +0.5 V vs. SCE.[2,4] Furthermore, the RuO_2 couple is more quasi-reversible in character, with broad peaks and an approximate peak separation much larger than the standard 59 mV for a fast one-electron transfer.[32] The unidentified redox couple was found for several different Ru on BP composite CMEs. As such, it was theorized that the redox couple could be due to hydroquinone/quinone groups being generated from the carbon support during cycling. To test this, Black Pearls blank CMEs were cycled in the same manner as composite CMEs to look for evidence of quinone formation.

Figure 4.14 shows the CVs of a blank Black Pearls CME before and after cycling. Large anodic and cathodic peak currents were observed at +0.4 V and +0.3 V vs. SCE, respectively, after cycling indicating a redox couple around ca. +0.35 V vs. SCE. This was the same couple observed for composite CMEs; its presence on the blank Black Pearls CME ruled out generated RuO_2 as the origin of the couple. The redox couples of hydroquinone and several quinone derivatives are found in the range of +0.3 V to +0.46 V in aqueous media as reported by Hubbard *et al.*[40], thereby confirming that quinone groups were being formed during potentiometric cycling. In addition, the quinone groups were formed quite readily while very little evidence of substantial RuO_2 formation was found. The considerable current contributed by the hydroquinone/quinone redox couple also increased the capacitance of the blank Black Pearls CME. Prior to

quinone formation, the specific capacitance of the CME was 145 F g^{-1}; after generating the quinone groups, the specific capacitance of the CME jumped to ca. 300 F g^{-1}. While this result was encouraging, it did not fall in line with the experimental objective of using high surface area activated carbons as the support materials for more redox-active species such as RuO_2. However, further exploration of the capacitive character of quinone carbonyl groups on carbon supports could lead to stable and easily fabricated aqueous EDLCs.

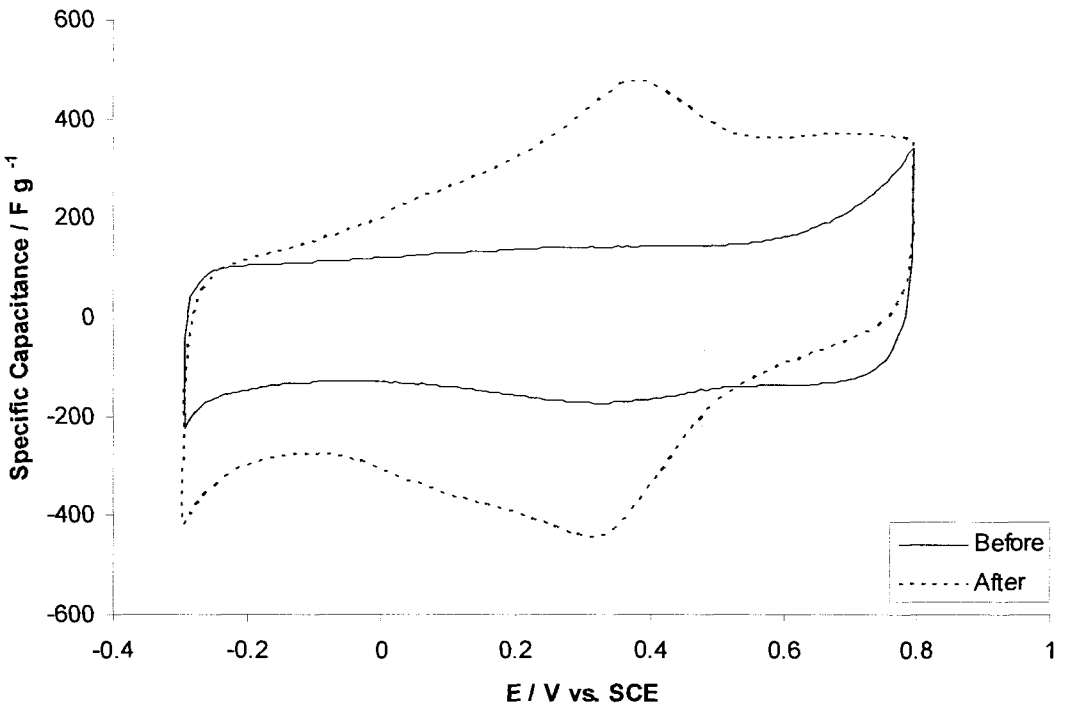

Figure 4.14. Specific capacitance of a blank Black Pearls CME (mass loading of 0.80 mg) before and after potentiometric cycling. For comparative purposes, the upper potential limit was decreased from +1.4 V to +0.8 V after 55 cycles to obtain a CV in the same potential range as the initial Black Pearls blank.

Apart from the formation of quinone at higher potentials, no significant overall increase in current was observed for composite CMEs before and after cycling. However, with prolonged cycling (usually greater then 10 cycles) at high potentials, Ru metal dissolution was observed for numerous CMEs. Once the potential exceeded +1.2 V, a light yellow discolouration of the electrolyte solution was observed streaming from the working electrode; the colour intensified with repeated cycles. With extended cycling, this resulted in composite CMEs with greatly diminished capacitance values, in stark contrast to the desired effect of cycling. In several cases, the capacitance of the original, non-cycled CME was higher than that of the cycled CME due to rapid dissolution of Ru metal in the electrolyte. The inconsistency of this method for generating ruthenium oxide led to a search for alternative methods for oxide formation. While simple annealing was attractive, it would have lead to the undesired crystallization of the RuO_2, a characteristic which can have detrimental effects on the specific capacitance of the composite.[25,30] As such, the method chosen was simple aging in air. While not the most rapid means of oxide formation, the consistency of specific capacitance results between composites with the same theoretical mass loading of Ru^0 lead to its exclusive use for RuO_2 formation.

The specific capacitance of the composites increased with extensive aging in air. This is illustrated in Figure 4.15a, which depicts CVs for a composite of 29.94 mass % Ru/RuO_x on Vulcan carbon measured at different aging intervals. When only aged for 1 week, the composite yielded a specific capacitance of ca. 90 F g^{-1}. However, extensive aging over a period of 20 weeks resulted in a specific capacitance of 182 F g^{-1}. This confirmed that prolonged exposure of Vulcan-based composites to the air resulted in

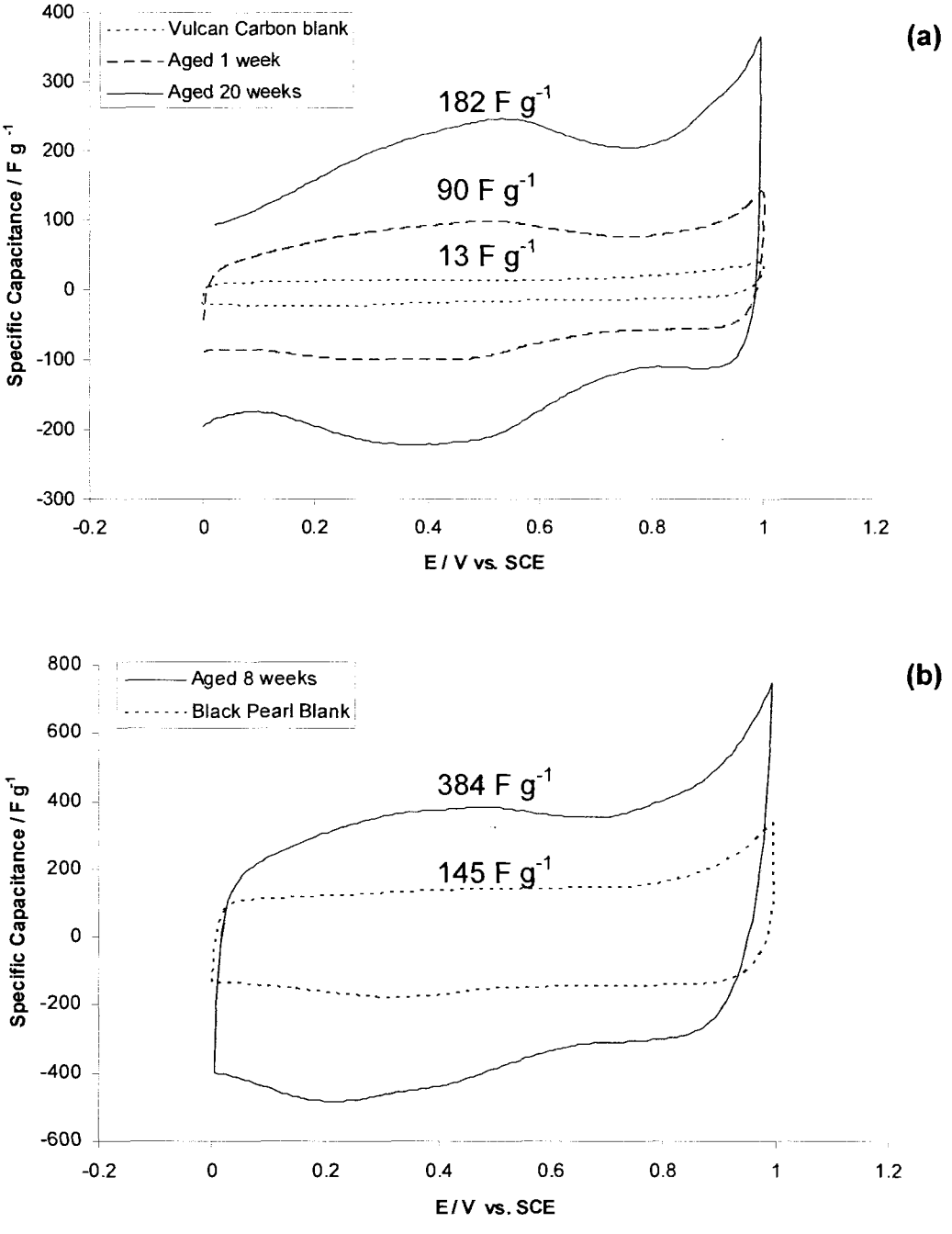

Figure 4.15. Cyclic voltammograms of (a) 29.94 mass % Ru/RuO_x on Vulcan (1.28 mg loading) and (b) 42.9 mass % Ru/RuO_x on Black Pearls (1.37 mg loading) composites aged for different time intervals in air. Blank carbon CMEs are shown for the respective carbon supports as references.

greater RuO_2 formation and hence a larger specific capacitance. The same result was found to be true for a 38.9 mass % Ru on Black Pearls composite. Figure 4.15b illustrates this, with the aged composite CME producing a specific capacitance of 382 F g^{-1}, well beyond the 145 F g^{-1} of the unmodified Black Pearls CME. In addition, the specific capacitance of the 38.9 mass % Ru on BP CME was more than double that of its Vulcan Carbon counterpart, despite the Black Pearls based composite being aged for less than half that of the Vulcan based composite. A comparison of the CVs of the two composites is shown in Figure 4.16. The significantly higher specific capacitance of the Black Pearls

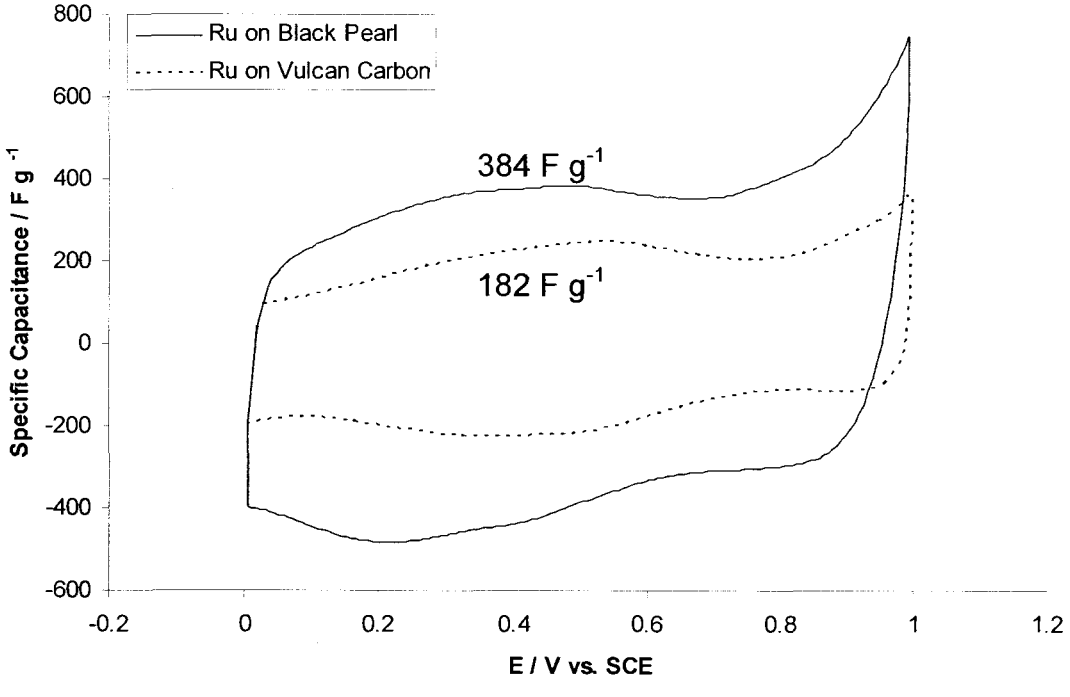

Figure 4.16. Comparison of cyclic voltammograms for 29.94 mass % Ru/RuO_x on Vulcan (1.28 mg loading) and 42.9 mass % Ru/RuO_x on Black Pearls (1.37 mg loading) composites.

Capacitance measurements were performed for all prepared composites using Vulcan and Black Pearls as the carbon support. In addition, the specific capacitance of the electroactive RuO_2 itself was calculated in order to determine its contribution to the total capacitance of the composite. The following formula was used to determine the specific capacitance of RuO_2:[25]

$$C_{S,RuO_x} = \frac{C_{S,Total} - (1 - m_{Ru/RuO_2})C_{S,Carbon}}{m_{Ru/RuO_2}} \qquad \text{(Equation 4.2)}$$

where $C_{S,RuOx}$ is the specific capacitance of RuO_x, $C_{S,Total}$ is the specific capacitance of the composite, $C_{S,Carbon}$ is the specific capacitance of the carbon support, and $m_{Ru/RuO2}$ is the mass fraction of Ru/RuO_2 in the composite. The results of these calculations as well as the capacitances of all the composites that were tested are summarized in Table 4.5. Not surprising, the highest theoretical mass % Ru/RuO_x composites on both Vulcan and Black Pearls (79.5 % by mass) yielded the highest achievable $C_{S,Total}$ values at 300 F g^{-1} and 574 F g^{-1}, respectively. These results compare favourably with specific capacitance values of similar carbon-supported RuO_2 supercapacitor materials as reported in the literature, with the Black Pearls composite's capacitance amongst the highest.[26-29]

In addition, the $C_{S,Total}$ values for the Black Pearls composites were all greater than their Vulcan composite counterparts. This confirmed that using a higher surface area carbon support resulted in greater utilization of the electroactive Ru material during capacitance measurements and hence, led to composites with increased specific capacitances overall.

Table 4.5. Summary of specific capacitance data for all composites.

Carbon Support	Theoretical mass % Ru	Analytical mass % Ru/RuO_x	$C_{S,Total}$ ($F\ g^{-1}$)	$C_{S,RuOx}$ ($F\ g^{-1}$)
Vulcan	4.6	9.6	58 ± 2	481 ± 23
	15.6	23.5	147 ± 2	**583 ± 7**
	30.1	29.9	182 ± 5	577 ± 15
	50.1	53.4	216 ± 16	393 ± 31
	79.5	81.1	**300 ± 11**	367 ± 14
Black Pearls	4.6	13.4	162 ± 11	272 ± 138
	15.6	25.7	253 ± 8	565 ± 58
	30.1	38.9	384 ± 13	**758 ± 44**
	50.1	56.7	482 ± 20	740 ± 38
	79.5	-	**574**	-

The specific capacitance of each composite was next plotted against both the theoretical mass % Ru and the analytical mass % Ru/RuO_x to search for any discernable trends or patterns. These plots are shown in Figure 4.17. As expected, increasing the theoretical percentage of Ru metal resulted in an increase in specific capacitance. In fact, when plotted against the theoretical percentages, a linear relationship between the mass % of Ru and $C_{S,Total}$ is observed for both types of carbon support composites, as shown in Figure 4.17a. This relationship justifies the practicality of using the mass ratios of

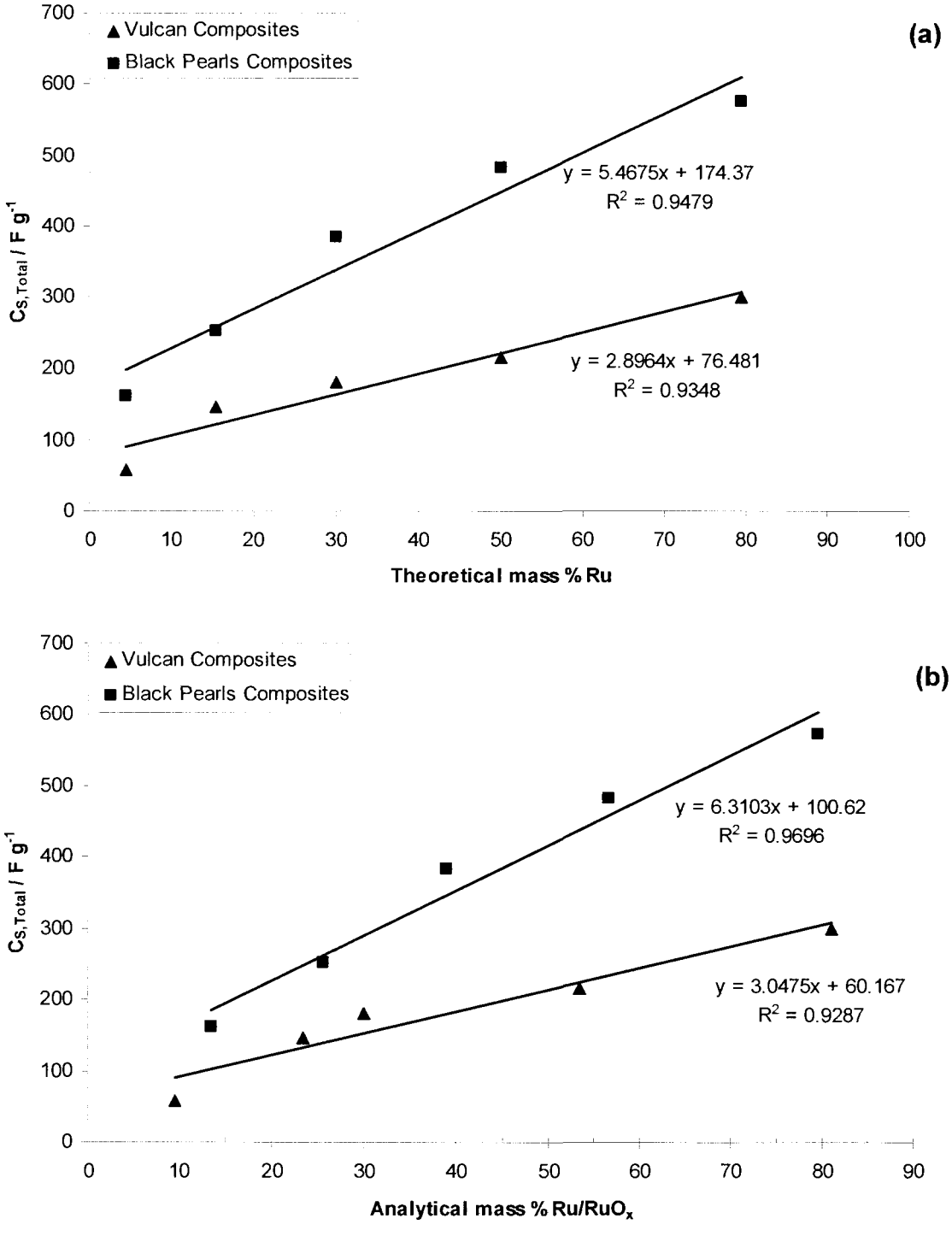

Figure 4.17. Comparison of specific capacitance values for both types of carbon-based composites plotted against the (a) theoretical mass % Ru and (b) analytical mass % Ru/RuO_x.

precursor materials as the basis for producing the composites. As the degree of oxidation of Ru^0 to RuO_2 is not easily discerned, the theoretical percentages provide a sound reference point for both predicting and reporting capacitance values. Additionally, when the analytical percentages are used, the linear relationship between $C_{S,Total}$ and the mass % Ru/RuO_x is maintained, as seen in Figure 4.17b.

The variability in capacitance is seen more clearly in Figure 4.18, which depicts the values of $C_{S,RuOx}$ plotted against the analytical mass % Ru/RuO_x. When comparing composites of approximately the same analytical mass % Ru/RuO_x almost no similar $C_{S,RuOx}$ values were found. This highlights, among other things, the measure of variability of oxide formation in the composites. The lone exception is found between ca. 23 and 30 mass % Ru/RuO_x where the $C_{S,RuOx}$ values for a Black Pearls and two Vulcan composites are 565 F g^{-1}, 577 F g^{-1} and 583 F g^{-1}. The slightly higher capacitance values for the Vulcan composites are likely due to their longer aging times (16 and 20 weeks) compared to the Black Pearls composite (1 week). This allowed for more extensive conversion of the available Ru^0 to RuO_2, thereby increasing the capacitive capability of the composites. One seemingly random result is the higher $C_{S,RuOx}$ value of 9.6 mass % Ru/RuO_x on Vulcan versus 13.4 mass % Ru/RuO_x on Black Pearls. The specific capacitance of 481 F g^{-1} for the Vulcan composite is notably higher than the 272 F g^{-1} of the Black Pearls composite. The lower capacitance is due to a large contribution of both C=O groups in the Black Pearls as well as possible impurities to the mass of the composite, which artificially lowers the specific capacitance. This would result in a corresponding decrease in the value of $C_{S,RuOx}$ according to Equation 4.2. While this explains the low $C_{S,RuOx}$

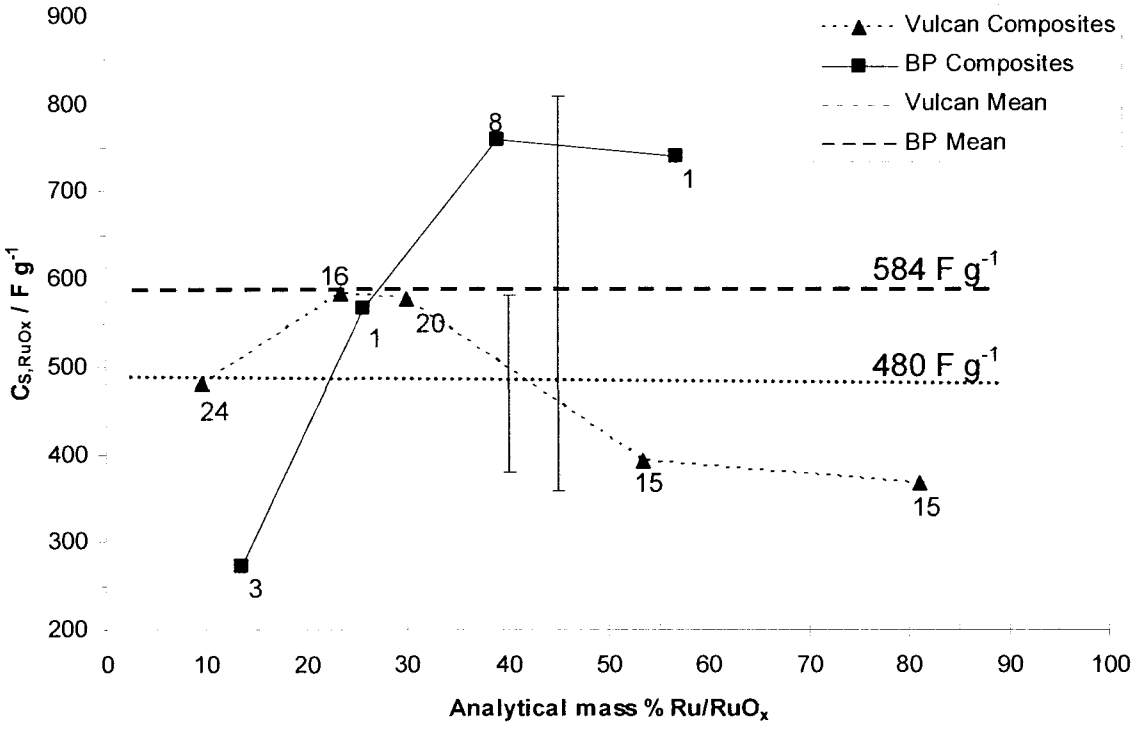

Figure 4.18. Comparison of $C_{S,RuOx}$ values for all composites based on analytical mass % Ru/RuO_x. The value next to each point indicates the composite aging time in weeks. Average $C_{S,RuOx}$ values with standard deviations are shown.

value for the BP composite, it does not explain the large $C_{S,RuOx}$ value for the Vulcan composite. As with the previous capacitance comparison between composites with different carbon supports, the most likely explanation is the increased aging of the Vulcan sample (24 weeks versus 3 weeks for the BP composite). Again, this may have resulted in more extensive and nearly complete conversion of Ru^0 to RuO_2, especially given the lower initial mass % Ru in the sample. The maximum values of $C_{S,RuOx}$ were found to be 583 F g^{-1} for the ca. 30 mass % Ru on Vulcan composite and 758 F g^{-1} for the 38.9 mass

% Ru/RuO_x on Black Pearls composite, which was close to that of similar composite materials in the literature.[26-29] All maximum capacitance values are highlighted in Table 4.5. Overall, the mean $C_{S,RuOx}$ values for Vulcan and Black Pearls composites only differed by ca. 100 F g^{-1}. In addition, the overlapping standard deviations of the means shown in Figure 4.8 indicate that the capacitances values obtained with composites of either carbon support were not significantly different. As discussed previously, it was hoped that six-fold increase in specific surface area of the Black Pearls over the Vulcan carbon would provide greater $C_{S,RuOx}$ values, but this was not always the case.

In summary, the specific capacitance of both types of composites increases linearly when increasing the mass % Ru and/or Ru/RuO_2. The Black Pearls composites generally yield higher $C_{S,Total}$ values than the Vulcan composites. Composites of Ru/RuO_x on Black Pearls supports yielded maximum attainable $C_{S,Total}$ and $C_{S,RuOx}$ values of 574 F g^{-1} and 758 F g^{-1}, respectively, which compare favourably to literature values. However, whether due to aging or surface area differences, neither Blacks Pearls nor Vulcan carbon produced composites with $C_{S,RuOx}$ values that clearly outperformed the other. Regardless, given the unknown degree of oxidation of Ru^0 to RuO_2, it was theorized that the effective loading of electroactive Ru in the composites was not being fully utilized.

4.4 Conclusions

The reductive deposition of ruthenium nanoparticles onto high surface area carbon supports yielded composites with high values of specific capacitance. Using both Vulcan Carbon XC72 and Black Pearls 2000 as the carbon supports produced composites

with capacitances that were substantially greater than that of the carbon alone. The specific capacitances of the composites increased linearly with increasing mass % of ruthenium. The maximum specific capacitances attained were 300 F g^{-1} and 574 F g^{-1} for the theoretical 79.5 mass % Ru on Vulcan and Black Pearls composites, respectively. Overall, the Black Pearls composites produced higher values of $C_{S,Total}$. The maximum $C_{S,RuOx}$ values were determined to be 583 F g^{-1} for the 23.5 mass % Ru/RuO_x on Vulcan composite and 758 F g^{-1} for the 38.9 mass % Ru/RuO_x on Black Pearls composite. Both of these values are on par with $C_{S,RuOx}$ values reported in the literature. However, the difference between the mean $C_{S,RuOx}$ values for both composites was only 100 F g^{-1}, indicating that both carbon supports promoted similar electroactive Ru/RuO_2 utilizations.

XPS analysis revealed that RuO_2 was the dominant form of the oxidized Ru^0 nanoparticles, as expected. XRD showed no diffraction pattern for RuO_2, indicating that the aging in air resulted in an amorphous oxide, as desired. However, the XPS results indicate that the Ru^0 was not completely converted to RuO_2 during aging, resulting in composites with less than a maximum effective loading of the oxide. XRD results confirmed the existence of crystalline Ru^0 nanoparticles in the aged composites that were ca. 3.1 nm in mean particle diameter. This led to the theory that as the Ru^0 nanoparticles were oxidized, they produced amorphous RuO_2 which slowly grew around the metal centre. Eventually, the partially depleted Ru^0 "core" was surrounded by a RuO_2 "shell", preventing further oxide formation. TEM analysis yielded nanoparticles in the composites which had a mean particle diameter of 8.9 nm; these particles were larger than the Ru^0 particles measured by XRD. However, the XRD results may have been

dominated by the greater number of smaller nanoparticles, overshadowing the contribution from the larger particles. In addition, it was uncertain whether the numerous smaller nanoparticles visible via TEM, which would have influenced the mean particle diameter, were those of Ru^0 or RuO_2. Thus, while existence of the "core-shell" structure of the Ru^0/RuO_2 in the composites is highly probable based on the materials characterization results, the proof is not definitive.

The strong evidence for the core-shell structure is significant. It indicates an incomplete usage of the available ruthenium in the composites, which translates to less than maximum specific capacitance values. Since the goal of these experiments was to maximize the capacitance while minimizing the total mass of the composite, the unused ruthenium is detrimental to the capacitance of the material. It essentially serves as deadweight, artificially decreasing the specific capacitance of the composites while making minor contributions to both the EDL and pseudocapacitance, if any. For these reasons, the confirmed core-shell structure is mildly disappointing. However, there is an upshot to the structures. The incomplete oxidation of Ru^0 to RuO_2 could simply be due to the aging method of oxide formation. The capacitance values reported still compared favourably to those found in literature.[4,26-29] If a more efficient oxide formation technique were used, the composites would have the potential for capacitance values beyond those reported. This encourages further experimentation to determine the best method of oxide formation to produce composites with fully realized capacitance capabilities.

4.5 References

1. Brodd, R. J.; Winter, M. *Chem. Rev.* **2004**, 104, 4245.

2. Chen, C.P.; Tilak, B.V.; Sarangapani, S. *J. Electrochem. Soc.* **1996**, 143, 3791.

3. Burke, A. *J. Power Sources.* **2000**, 91, 37.

4. Cygan, P.J.; Jow, T.R.; Zheng, J.P. *J. Electrochem. Soc.* **1995**, 142, 2699.

5. Belanger, D.; Hill, I. R.; Quinn, D.; Toupin, M. *J. Power Sources.* **2005**, 140, 203.

6. Hollenkamp, A.F.; Pandolfo, A.G. *J. Power Sources.* **2006**, 157, 11.

7. Chesneau, M.; Fauvarque, J. F.; Gamby, J.; Simon, P.; Taberna, P. L. *J. Power Sources* **2001**, 101, 109.

8. Lin, C.; Ploehn, H. J.; Popov, B. N. *J. Electrochem. Soc.* **2002**, 149, A167.

9. An, K. H.; Bae, S. C.; Choi, Y. C.; Chung, D. J.; Kim, W.S.; Lee, D. C.; Lim, S. C.; Park, Y. C. *Adv. Mater.* **2001**, 13, 497.

10. Beck, F.; Dolata, E.; Grivei, E.; Probst, N. *J. Appl. Electrochem.* **2001**, 31, 845.

11. Kim, K.-H.; Kim, S.-J.; Lee, K.-H.; Sung, J.-H. *J. Power Sources.* **2004**, 133, 312.

12. Belanger, D.; Davey, J.; Ren, X.; Uribe, F. *J. Electrochem. Soc.* **2000**, 147, 2923.

13. Goodenough, J. B.; Lee, H. Y. *J. Solid State Chem.* **1999**, 144, 220.

14. Anderson, M. A.; Chapman, T. W.; Pang, S.-C. *J. Electrochem. Soc.* **2000**, 147, 444.

15. Hu, C.-C.; Wang, C.-C. *J. Electrochem. Soc.* **2003**, 150, A1079.

16. Athouel, L.; Belanger, D.; Brousse, T.; Crosnier, O.; Dugas, R.; Toupin, M. *J. Electrochem. Soc.* **2006**, 153, A2171.

17. Anderson, M. A.; Liu, K. C.; *J. Electrochem. Soc.* **1996**, 143, 124.

18. Srinivasan, V.; Weidner, J. W. *J. Electrochem. Soc.* **1997**, 144, L210.

19. Srinivasan, V.; Weidner, J. W. *J. Electrochem. Soc.* **2000**, 147, 880.

20. Hu, C.-C.; Huang, Y.-H. *J. Electrochem. Soc.* **1999**, 147, 2465.

21. Carette, P. L.; Hagans, P. L.; McKeown, D. A.; Rolison, D. R.; Russell, A. E.; Swider, K. E. *J. Phys. Chem. B* **1999**, 103, 4825.

22. Haran, B. S.; Popov, B. N.; Ramani, M.; White, R. E. *J. Electrochem. Soc.* **2001**, 148, A374.

23. Kim, I.-H.; Kim, K.-B. *Electrochem. Solid-State Lett.*, **2001**, 4, A62.

24. I.D.Raistrick, in *The Electrochemistry of Semiconductors and Electronics-Process and Devices*, J. Mchardy and F. Luduig, Editors, p. 297, Noyes, Park Ridge, NJ (1992).

25. Chang, K.-H.; Chen, W.-C.; Hu, C.-C. *J. Electrochem. Soc.*, **2004**, 151, A281.

26. Kawai, M.; Kobayakawa, K.; Nanaumi, T.; Ohsawa, Y.; Sato, Y.; Yomogida, K. *Electrochem. Solid-State Lett.*, **2000**, 3, 113.

27. Kim, H.; Popov, B. N. *J. Power Sources*, **2002**, 104, 52.

28. Ko, J. M.; Park, J. H.; Park. O. O. *J. Electrochem. Soc.*, **2003**, 150, A864.

29. Jang, J. H.; Machida, K.; Min, M.; Naoi, K. *J. Electrochem. Soc.*, **2006**, 153, A334.

30. Lee, Y.-H.; Kim, I.-H.; Kim, J.-H.; Kim, K.-B. *J. Electrochem. Soc.*, **2005**, 152, A2170.

31. Fenton, J. M.; He, C.; Kunz, H. R. *J. Electrochem. Soc.*, **2003**, 150, A1017.

32. J. Wang, in *Analytical Electrochemistry*, p.31, Wiley-VCH, New York, NY (2000).

33. Zheng, J. P. *Electrochem. Solid-State Lett.* **1999**, *2*, 359.

34. Liu, P.; Verbrugge, M. W. *J. Electrochem. Soc.*, **2006**, 153, A1267.

35. Hsieh, C.-T.; Teng, H. *Carbon*, **2002**, 40, 667.

36. Ohta, K.; Okajima, K.; Sudoh, M. *Electrochim. Acta*, **2005**, 50, 2227-2231.

37. Andreas, H. A.; Conway, B. E. *Electrochim. Acta*, **2006**, 51, 6510.

38. Conway, B. E.; Hadzi-Jordanov, S.; Kozlowska, A. *J. Electroanal. Chem.* **1975**, *60*, 359.

39. Conway, B. E.; Hadzi-Jordanov, S.; Kozlowska, A.; Vukovic, M. *J. Electrochem. Soc.* **1978**, *125*, 1473.

40. Hubbard, A. T.; Soriaga, M. P. *J. Am. Chem. Soc.*, **1982**, 104, 2735.

Chapter 5

Summary and Future Work

In this thesis, two different types of materials containing ruthenium oxide were investigated for use in supercapacitors. RuO_2-TiO_2 hydrogels were shown to be moderately capacitive for electroactive sol-gels, albeit with stability issues requiring further study. Carbon-supported RuO_x composites were shown to be highly capacitive materials which have the potential to yield even greater capacitances due to incomplete conversion of Ru^0 to RuO_2.

Fabricating capacitive RuO_2-TiO_2 hydrogels was met with several difficulties. First, the use of CFP electrodes introduced corrosion background currents into numerous electrochemical measurements. This problem was resolved by wax impregnation of the CFP strips to stop capillary electrolyte flow. Next, the loss of RuO_2-TiO_2 CME stability due to rapid ruthenium dissolution during cycling diminished the capacitive capability of the electroactive gel. Modest heat treatment of the CMEs mostly resolved the Ru leaching issue in acid electrolyte, thereby increasing stability of the hydrogel.

Amongst all RuO_2-TiO_2 hydrogel CMEs, the maximum attainable specific capacitance was 10 F g^{-1}, a relatively high value compared to similar electroactive sol-gels. It was not reproducible, however, as both the lower stability of the hydrogels and the increased crystallinity of the annealed gels decrease the capacitive capability of the CMEs. Overall, the potential of RuO_2-TiO_2 hydrogel is encouraging, although variable capacitance and stability issues currently limit their appeal as supercapacitor materials.

Future work in the area of electroactive RuO_2-TiO_2 sol-gels should involve using different (Ru+Ti):H_2O:H^+:EtOH mole ratios to change the rate of gelation so as to strengthen the gel network during aging, thereby increasing the stability of the hydrogels

and preventing Ru dissolution during CME cycling. Also, hydrogels should be aged for fixed time intervals to determine the effect of aging on capacitance and stability. Finally, precise control of the temperature and time interval during the heat treatment process is necessary in order to optimize the stability and capacitance of the gels.

The reductive deposition of ruthenium nanoparticles onto high surface area carbon supports has been shown to produce highly capacitive composites that most likely containing Ru^0 cores surround by RuO_2 shells. XPS confirmed that RuO_2 was the dominant oxide species and that the composites contained Ru^0 which was not converted to oxide. The existence of crystalline Ru^0 nanoparticles in the composites, which have a mean particle diameter of ca. 3.1 nm, was confirmed by XRD. The XRD analysis did not yield a diffraction pattern for RuO_2, indicating that the aging in air resulted in an amorphous oxide. The RuO_2 mean particle diameter was 8.9 nm as shown by TEM. Combined, these results provide strong evidence for the existence of core-shell ruthenium structures in the composites, which consist of crystalline Ru^0 cores surrounded by amorphous RuO_2 shells.

The specific capacitance of the composites has been shown to increase linearly with increasing mass % of ruthenium. The maximum specific capacitances attained for the Vulcan and Black Pearls composites were 300 F g^{-1} and 574 F g^{-1}, respectively, with the Black Pearls composites producing higher $C_{S,Total}$ values overall. However, it has been shown that the difference between the mean $C_{S,RuOx}$ values for both composites is only 100 F g^{-1}, indicating similar redox-active utilization of Ru/RuO_x for both carbon supports.

The maximum $C_{S,RuOx}$ values among the various Vulcan and Black Pearls composites were 583 F g^{-1} and 758 F g^{-1}, respectively.

Future studies in this area should involved the use of different organic electrolytes such as acetonitrile to determine if the composites are operable and maintain their capacitance over greater potential ranges. In addition, the composites should be used in a two-electrode setup so as to measure their performance in an actual supercapacitor. While the specific capacitance values of the composites compare favourably with literature values, they do not represent the full capacitive potential of the composites. The incomplete oxidation of Ru^0 to RuO_2, which results in a less than maximum effective loading of electroactive ruthenium in the composites, is likely due to the relatively slow aging method employed. Thus, future research in this area should involve the use of a more efficient oxide formation technique to promote complete conversion of Ru^0 to RuO_2. This could involve the temperature controlled aging of freshly made composites and/or CMEs in a hydrous atmosphere to promote the formation of amorphous $RuO_2 \cdot xH_2O$. Finally, different deposition techniques such as colloidal methods and electrophoretic deposition could be used to deposit Ru^0 and/or RuO_2 on carbon.